UNIVERSITÀ DEGLI STUDI DI PAVIA
DOTTORATO DI RICERCA IN FISICA – XXXI CICLO

Upgrade of the Small Wheels and search for Dark Matter in association with top quarks at the ATLAS experiment

Edoardo Maria Farina

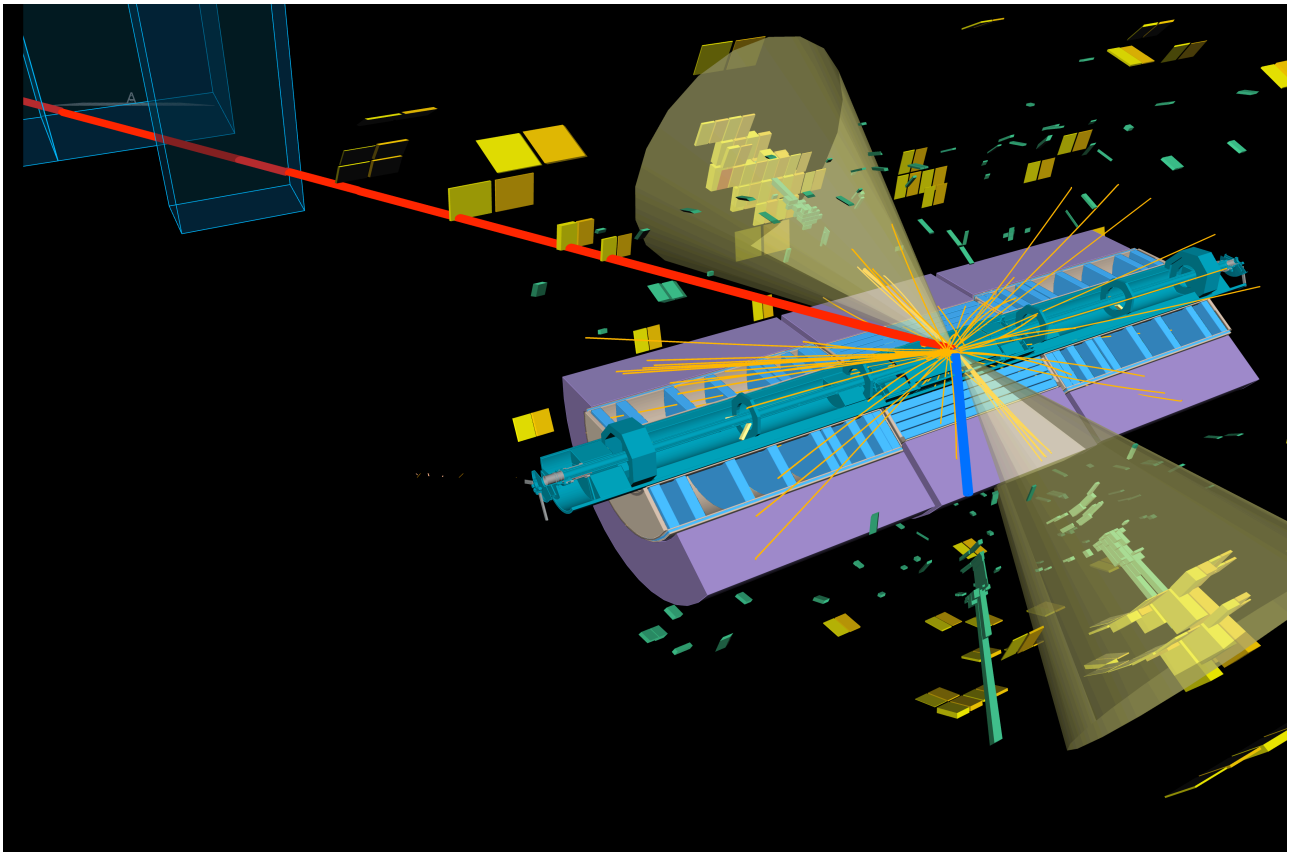

Tesi per il conseguimento del titolo

Università degli Studi di Pavia
Dipartimento di Fisica

DOTTORATO DI RICERCA IN FISICA – XXXI CICLO

Upgrade of the Small Wheels and search for Dark Matter in association with top quarks at the ATLAS experiment

Edoardo Maria Farina

Submitted to the Graduate School of Physics in partial fulfilment of the requirements for the degree of

DOTTORE DI RICERCA IN FISICA

DOCTOR OF PHILOSOPHY IN PHYSICS

at the

University of Pavia

Supervisor: Prof. Adele Rimoldi

Referees: Dr. Gabriella Pugliese
Prof. Alessia Tricomi

Cover: Display of a candidate top-antitop event from proton-proton collisions recorded by ATLAS with LHC stable beams at a collision energy of 13 TeV. The candidate event is reconstructed in the electron, muon and 2 b-tag jets final state.

Upgrade of the Small Wheels and
search for Dark Matter in association with top quarks
at the ATLAS experiment

Edoardo Maria Farina

PhD thesis - University of Pavia
Pavia, Italy, January 2019

Introduction

When I was about to start my PhD I made myself the promise to learn everyday something new. My goal was to get involved in as many aspects as possible of a modern High Energy Physics experiment, gaining experience in both the hardware and in the physics analysis worlds; not an easy task, as I experienced.

This thesis tries to follow this philosophy; after a short introduction to the Standard Model and to the ATLAS experiment, three distinct topics related to the ATLAS experiment will be described highlighting my personal contributions.

In chapter 4, a long term ageing study on small Micromegas detector prototypes carried out at the Gamma Irradiation facility at CERN is reported. The project has been of great importance in the context of the ATLAS New Small Wheel upgrade, since it showed how performance changes when Micromegas detectors are irradiated for a long time in high rate particle environments. In addition, high rate performance studies have been performed, supported by a dedicated Geant4 simulation.

Chapter 5 is dedicated to the quality control procedures that I contributed to set up and perform on more than 1500 readout boards for the mass production of the Micromegas detectors in view of their installation in the experiment from 2019. This task has been, and still is, a crucial aspect for the upgrade project: our responsibility is to certify the quality of the most complex part of the detector, investigate source of problems and figure out solutions to be quickly implemented on the production chain of our suppliers. In the chapter, I will emphasize the complexity and responsibility of this task and of its large impact on the Collaboration.

Chapter 6 is focused on a search for Dark Matter based on 36.1 fb^{-1} collected by the ATLAS experiment. Dark Matter is known to be a dominant component of the Universe. It might be directly produced at colliders, depending on the mass and interactions, and the search for WIMPs (Weakly Interacting Massive Particles) is one of the main field of search of new physics

at LHC. The analysis described is based on a Simplified Model, where the Standard Model (SM) is coupled to the Dark sector by means of spin 0 scalar or pseudoscalar mediators. In particular we are looking for Dark Matter production in association with two top quarks, leading to two leptons in the final state. I will discuss the model, how physics objects are reconstructed in ATLAS, then focusing on the analysis strategy, based on the comparison of the observed and estimated number of events passing a well-defined selection. Each SM process contributing to the background has been individually estimated via Monte Carlo or data driven techniques. Results are finally interpreted in terms of discovery limits, both model dependent and independent.

In conclusion, in the appendix, I present my contribution to a Detector R&D project, where a novel design of gaseous detector is proposed for even higher rate particle environments. In appendix D, I describe my contribution to the development of the Atlas New Small Wheels Databases, in particular concerning the Italian QAQC database and its own web interface. This activity aims to provide a reliable system to store the data concerning the detectors and the raw material, during the mass production.

Contents

Chapter 1

The Standard Model of elementary particles

In 2012 ATLAS and CMS, two of the main experiments at the Large Hadron Collider (LHC), jointly claimed the discovery of a particle compatible with the last missing piece of the Standard Model (SM) [1, 2], the Higgs boson. This represented an epochal milestone for mankind, eventually leading to the Nobel Prize award, and a turning point for particle physics. If, in the last years, we were guided in the discoveries by strongly supported theories, now we are facing a new era, where experiments need to provide some new evidences and break our current understanding of Nature. We can say that the discovery of the Higgs boson answered the only one big question we had concerning its existence, but at the same time left the floor to many others, deeper and more fascinating ones. In this first chapter a short description of the Standard Model is given, then later focusing on its limits and unexplained observations. One of these is the existence of *Dark Matter*, whose search is part of this thesis.

1.1 The Standard Model

The Standard model mathematically describes three of the four forces observed in Nature, gravity is not included, all the elementary particles involved and their interactions. Technically it is a renormalizable quantum field theory, where particles are represented by local quantum fields, while interactions are generated by imposing local gauge symmetry invariances. The SM gauge group is $SU(3)_c \times SU(2)_I \times U(1)_Y$, where $SU(3)_c$ describes the QCD interactions, and $SU(2)_I \times U(1)_Y$ describes the unified electroweak interactions.

A summary of the elementary particles is reported in Fig. 1.1 together with some of the most relevant properties. Particles having spin equal to 1/2 are called fermions and are, at their turn, divided into two categories based on their interactions, quarks and leptons. Both quarks and leptons are subdivided into three generations. Leptons have electric charge equal to -1 and +1 (electrons,

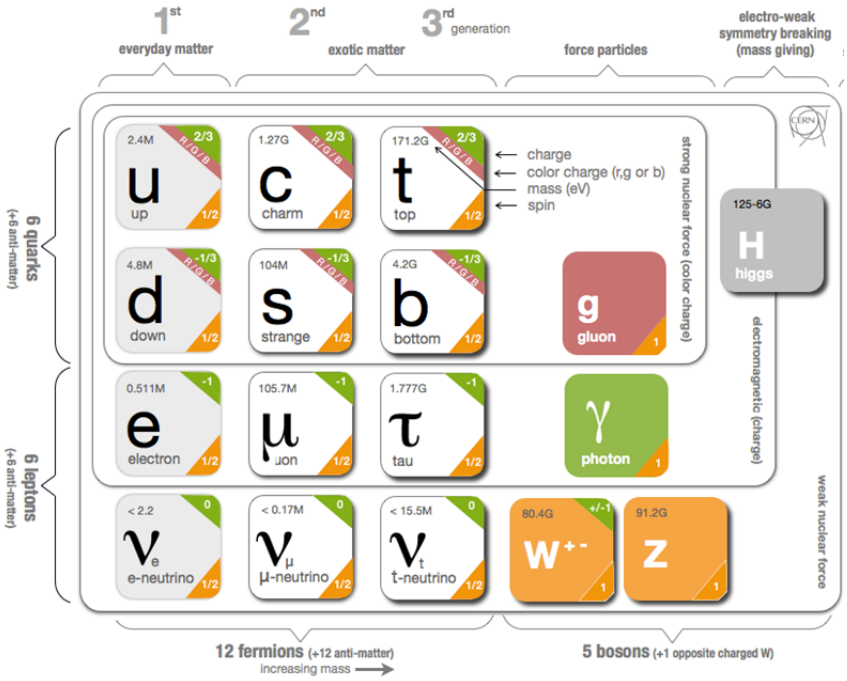

Figure 1.1: SM elementary particles

muons, taus and their antiparticles respectively) and 0 (neutrinos and their antiparticles), and they are only involved in electroweak interactions. Quarks, on the other hand, have electric charge equal to 2/3 and -1/3 respectively and they are coloured (the colour being the quantum number of the strong interaction).
Bosons, excluded the Higgs boson, have spin equal to 1 and are the force mediators: an interaction between two particles occurs when a vector boson is exchanged. The $W^{\pm}$ and Z^0 bosons are the mediators of the weak interaction, the photon (γ) of the electromagnetic and the gluon (g) of the strong one. The Higgs boson is an exception in this picture, since it has spin equal to 0. Its existence is of crucial importance to explain the massive nature of the electroweak bosons, and to give a mass to all the other massive particles as well.

1.2 Electroweak theory

Weak and electromagnetic interactions have been unified under a common electroweak theory. The physicists behind this extraordinary milestone, Sheldon Glashow, Abdus Salam, and Steven Weinberg, have been awarded the Nobel prize in 1979 [3]. As already mentioned the electroweak theory is based on $\mathrm{SU}(2)_I \times \mathrm{U}(1)_Y$, defining the gauge group, where I is the weak isospin and Y

the ipercharge. Isospin and ipercharge satisfy the Gell-Mann-Nishima relation

$$Q = I_3 + \frac{1}{2}Y$$

where Q is the particle charge and I_3 is the third component of the isospin. Imposing the local symmetry leads to the introduction of three massless, spin 1 gauge bosons W_i and an additional spin 1 gauge boson B. To provide mass terms to the gauge bosons, the electroweak symmetry is broken by the Higgs mechanism [4], leading the to mass eigenstates:

$$W^{\pm} = \frac{1}{\sqrt{2}}(W^1 \mp W^2)$$

and

$$\begin{pmatrix} A_\mu \\ Z_\mu \end{pmatrix} = \begin{pmatrix} \cos\theta_W & \sin\theta_W \\ -\sin\theta_W & \cos\theta_W \end{pmatrix} \begin{pmatrix} B_\mu \\ W^3_\mu \end{pmatrix}$$

where θ_W is the weak mixing angle. The masses of the two bosons can be thus derived:

$$m_W = \frac{1}{2}vg \quad \text{and} \quad m_Z = \frac{v}{2}\sqrt{g'^2 + g^2}, \tag{1.1}$$

where g and $g\prime$ are the SU(2) and U(1) gauge coupling respectively and v is the vacuum expectation value of the Higgs field. The relation between boson masses and mixing angle can be also obtained:

$$\frac{m_W}{m_Z} = \cos\theta_W \tag{1.2}$$

1.3 Strong theory (QCD)

Interactions among quarks are based on the invariance of the Lagrangian under a SU(3) rotation in the colour space. Imposing the invariance leads to 8 gauge fields, corresponding to 8 gluon types. Also in this case a broken symmetry is introduced in order to explain the different quark masses. Two very important differences arise with respect to the electroweak case. The first one is the behaviour of the coupling constant α_S as a function of the transferred momentum. At high energy it goes to zero asymptotically and it can, therefore, be treated with perturbative mathematical approaches. On the other hand, at large distances and small momentum transferred the coupling increases requiring different and more complex techniques as the lattice QCD [5]. The first difference, consequence of the way the constant evolves, is the colour confinement, according to which quarks and gluons cannot be isolated and observed singularly. This property comes from the nature of the strong force and of its massless mediator.

1.4 Limits of the SM

Despite having been tested to an extremely high precision, the SM is far from being a complete theory. To reassure new generations of physicists, Nature has jealously kept still an enormous amount of secrets. In the following, the most relevant ones are described, focusing in particular on the Dark Matter open problem.

- **SM is a model with many free parameters**. The SM does not descend from first principles. It has been built on the basis of experimental observations. It contains 19 free parameters, which need to be fixed by experimental measurements. Neutrinos are moreover massless in the model, while the experimental observation of neutrino oscillation tell us that neutrinos do have mass.

- **Gravity**. Gravity is still excluded from the model. A GUT (Great Unification Theory) including all the forces would definitely revolutionize our present understanding. At the moment the huge distance in order of magnitude between the gravitational and the other forces is still an open problem.

- **Three generations of particles**. We observe three generations of leptons and quarks with increasing masses. Why are those only three? Does this number come from something deeper?

- **Dark Matter/Energy**. The questions when our eyes are turned to the sky increase. The SM does not include any candidate for Dark Matter and no explanations for the Dark Energy.

- **Naturalness**. This is one of the main reasons motivating new particle physics search. A detailed dissertation can be found in Ref. [6]. The problem comes from the nature of the Higgs boson to couple to all fermions f giving them mass terms. Higgs mass at its turn receives quantum corrections as following:

$$m_h^2 \approx m_{h0}^2 + \frac{\lambda_f^2}{8\pi^2} N_c^f \Lambda^2, \tag{1.3}$$

  where $m_h \approx 125$ GeV, m_{h0} is the Higgs bare mass, while the remaining terms contribute to the $m_{h1-loop}$ correction to the Higgs mass. λ_f and N_c^f are the Yukawa coupling and the number of colours of the fermion f respectively. Λ is the cut-off limit of the theory, in other words, the largest energy at which the standard model is considered as valid. If the naturalness is naively defined as the ratio between $m_{h1-loop}$ and m_h it turns out that, for large value of Λ a fine tuning of many orders of magnitude is required of the bare mass and 1-loop correction to yield the observed Higgs mass. We are talking about 1 part over 10^{30}. This

problem exists only if the SM is considered valid up to a cut off scale which is well above the TeV scale. Proposed solutions to this problem are outside the scope of the thesis, but Supersymmetry (SUSY) deserves to be mentioned. Weak-scale supersymmetry introduces a new gauge symmetry which has been investigated in great details both theoretically and experimentally [7, 8, 9]. To every fermion a boson partner (or *s-partner*) is introduced and viceversa, every boson has fermionic partners. Under some assumptions, the $m_{h1-loop}$ contributions would completely vanish or, as in the case of broken supersymmetry, reduce to a logarithmic dependence to the cut-off scale, without any need for a fine tuning of the theory.

1.5 Dark Matter

One of the most astonishing aspects of our current understanding, or, better to say, not understanding, of Nature is that we are just looking at about 4% of the mass of the Universe. All the rest, 73% and 23%, are thought to be due to Dark Energy and Dark Matter respectively. The Dark adjective attests our ignorance concerning the real nature of this mass and energy. Dark Energy is the most accredited explanation for the increasing speed expansion of the Universe and it fits perfectly in the ΛCMD cosmological model, describing the evolution of the Universe, since the very beginning to our age. Detailed reviews on the topic can be find at Ref. [10, 11].
In the following some experimental and cosmological evidences in favour of the existence of the Dark Matter are reported, together with the most supported candidates and searches performed both at colliders and in dedicated experiments. For a detailed review refer to Ref. [12].

1.5.1 Experimental evidences

The first and oldest evidence, dated back in the early 1930, concerns the observation of the rotational velocity of galaxies, which could not be explained by only the barionic visible mass. Observations performed by J. H. Oort and F. Zwicky [13] agreed that the observed mass could not be more than a few percent the overall amount present in the Universe. 40 years later, Vera Rubin and collaborators extensively studied more than 60 galaxies, measuring the rotational velocity from the analysis of the spectral lines (Doppler effect). In absence of invisible mass, the velocity of stars in the galaxy should be described as the velocity of our planet around the Sun, thus:

$$v(r) = \sqrt{\frac{Gm(r)}{r}} \tag{1.4}$$

where $v(r)$ is the velocity, G is the gravitational constant and m is the mass within a radius r. The dependence from the radius goes as $1/\sqrt{r}$, decreasing as

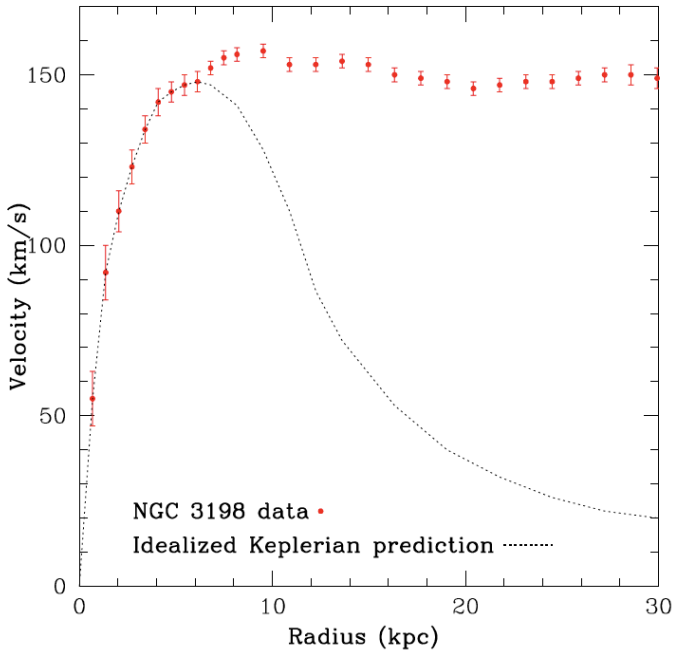

Figure 1.2: Expected rotational velocity in case of classical gravitational behaviour and measured one (red dot)

the distance from the center increases. Surprisingly the data observed showed a flat behaviour, meaning that the velocity does not decrease with increasing distances. The expected and observed behaviour are shown in Fig. 1.2. The agreement is restored if an invisible massive halo fills all the space and it is not concentrated, as the ordinary mass, close to the central bulge of the galaxy [14]. The second evidence derives from the observation of the gravitational lensing effect. This effect is due to the deformation of the spacetime in presence of a mass affecting the motion of bodies and light. Gravitational lensing effect allows, due to the bending of the light, to spot objects placed directly behind a closer one (in this case an "Einstein ring"is formed). Without entering into details from the reconstructed image of the hidden object it is possible to determine the amount of mass generating the gravitational effect. As an example, observation performed on Abell 370 cluster by Bergmann, Petrosian and Lynds led to an estimation of the total mass of the cluster to be about $10^2 - 10^3$ the observed one [15].

More recently, another important contribution is provided by cosmological observations. Among them the CMB anisotropy measurements performed by COBE, WMAP and by Planck [16, 17], seems to point to a large abundance of dark matter in the Universe. The extremely small anisotropies (30 ± 5 µK) found cannot be the only responsible for the seeds of the early Universe structure; given these fluctuations, due to the initial density perturbations of

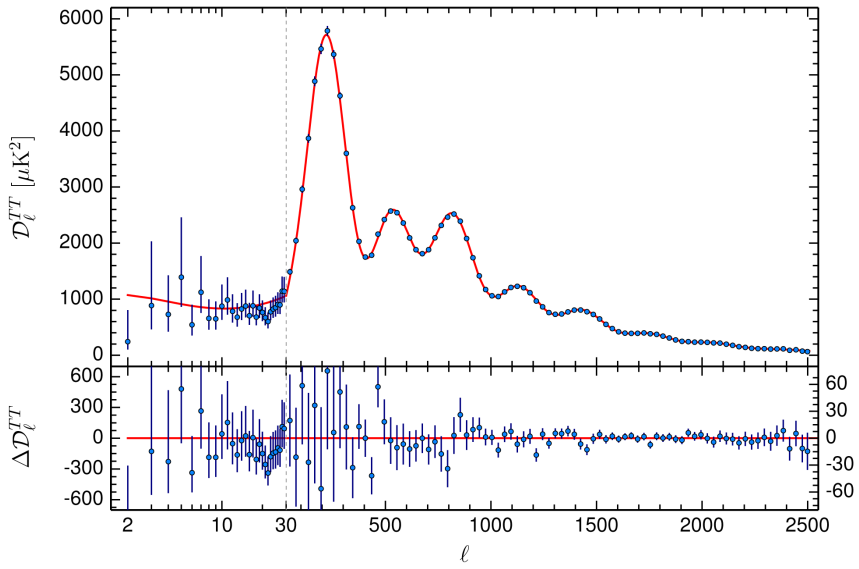

Figure 1.3: Planck 2015 power spectra. Comparison between data and expectations obtained from the total and baryonic densities is shown

the photon-barionic fluid, Universe would not have time to form. This implies the need for an electrically neutral form of matter that could start the structure formation process well before the recombination. Planck also provides the best estimation of the total and baryonic densities entering in the fit of the ΛCDM model [18]:

$$\Omega_m h^2 = 0.14170 \pm 0.00097 \quad \text{and} \quad \Omega_b h^2 = 0.02230 \pm 0.00014. \tag{1.5}$$

This very precise parameter estimation is dominated by the fit of the model to the CMB power spectrum shown in Fig. 1.3. Small variations in the baryonic and total densities would induce relevant changes in the anisotropy power spectrum, which are wholly inconsistent with the experimental data collected by Planck.

The last, in order of time, evidence, comes from the collision of a subcluster, called bullet, with a bigger galaxy cluster. During the collision hot gases compressed and heated up, leading to a strong X-ray emission, observed clearly by Chandra X-Ray Observatory [19]. Gases account for the vast majority of the baryonic mass. The strange thing is that the location of this emission and the position of the centre of mass obtained by means of the gravitational lensing effect show a relevant discrepancy. The region of X-Ray emission is not the same where the majority of the mass is concentrated [20, 21].

1.5.2 Dark Matter Candidates

Several Dark Matter candidates have been so far hypothesized and investigated within and outside the domain of the SM. The main properties of a perfect

candidate are the stability, or at least a long lifetime of the same order of magnitude of the cosmological time scale, it should gravitationally interact with ordinary matter and it should satisfy the measured relic density.
Still inside the SM, neutrinos could match the previous requirements. There are, however, at least two main reasons discouraging this choice: the first one is that neutrinos are relativistic particles, and a neutrinos-dominated universe would have prevented structure formation as we see today, favouring, on the other hand, larger structures formation first. The second aspect is that their measured abundance is not enough to account for the missing mass. WMAP constrained the neutrinos mass to be smaller than 0.23 eV, leading to a density of $\Omega_\nu h^2 < 0.0072$ [22]. Another widely supported possibility is represented by axions. These hypothetical particles have been postulated in 1977 to resolve the problem of CP violation in QCD (which is theoretically allowed, but never observed) and match all the dark matter candidate properties.
The search for sterile neutrinos are another very active field in physics. Those particles interact only gravitationally and bring right handed chirality. The introduction of right handed neutrinos is rather natural, as all known particles, except SM left-handed neutrinos, have been observed with both chiralities. Sterile neutrinos would also explain the SM neutrino masses in a natural way.
Finally, Dark Matter could also be made of WIMPs (Weakly Interacting Massive Particles). In the case of SUSY inspired models, the most popular WIMP candidate is the lightest supersimmetric sparticle which, if R-parity is conserved, cannot decay into ordinary matter. In this case the dark matter candidate is expected to interact weakly with ordinary matter and this is the property exploited in the WIMP hunting.

1.5.3 Search for WIMP Dark Matter

Many experiments have been designed, and will be in the future, as well, to detect WIMP Dark Matter using different and complementary methods. The most relevant are the direct and indirect searches, described in the following sections. A pictorial representation of the different approaches is reported in Fig. 1.4.

Direct detection

Direct detection experiments rely on the detection of the nuclei recoil due to the interaction of dark matter particles with detector material. Naively one would expect an upper limit on the energy deposed by a WIMP in about few keV, several order of magnitude below the contribution arising from the natural radioactivity. This makes the detection complex and requires a clean (and cold) environment. To be more precise the energy recoil is a function of the reduced mass $\mu = mM/(m + M)$ and the velocity v as following:

$$E = \frac{\mu^2 v^2}{M}(1 - \cos\theta),$$

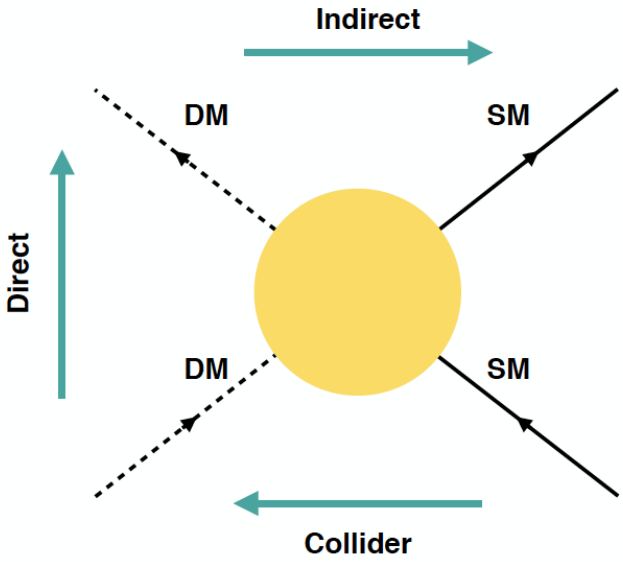

Figure 1.4: Schema of the different Dark Matter search approaches. Direct searches focus on detecting nuclei recoil of DM scattering against SM particles, indirect searches aim to find evidence of DM annihilation, while colliders investigate DM production from SM particles collisions

where θ is the scattering angle. Despite of the intrinsic experimental difficulties, WIMP events are expected to show some peculiarities making them recognizable over the background. In particular WIMP interactions are single-site events, while background events, such cosmic rays, can lead to multiple interactions. The second relevant aspect is that, if the dark matter halo is at rest with respect to the galaxy, the WIMP detection rate should vary at different time of the year due to the Earth movement in the direction of, or against, the dark matter halo. This modulation of the detection rate has been estimated to be of the order of 7%. Scattering processes are classified depending on the spin dependency, whether spin dependent (SD) or independent (SI). In the first case interactions result from the coupling with the WIMP spin and they are proportional to $J(J+1)$ rather than the number of nucleons (pseudo-scalar or axial-vector). In the second case there isn't such dependence and the cross section increases for larger nuclei. In Fig 1.5 limits on the WIMP cross section as a function of the mass in the spin-independent case are reported comparing the results provided by many different experiments. The most stringent limits are set by CDMS [23] and EDELWEISS [24] Collaborations both using silicon detectors, and LUX [25], a 370 kg double phase Xenon detector located in the US. DAMA Collaboration has claimed an annual modulation of the detected rate at 9.3 σ [26]. This positive observation has been interpreted in terms of dark matter model under two different solutions, a WIMP having mass $m_\chi \approx 50$ GeV and $\sigma_{\chi p} \approx 7 \cdot 10^{-6}$ pb or lower mass (range between 6 and 10 GeV) and $\sigma_{\chi p} \approx 10^{-3}$. The positive result from DAMA is indeed very controversial.

Indirect detection

Indirect detection experiments rely on the WIMP-WIMP annihilation. It is called indirect, since Dark Matter is not detected itself, while looking for annihilation products such as neutrinos, gamma rays and antimatter or muons. WIMP particles can be trapped by the Sun or the Earth, leading to an increase of their local densities and thus enhancing the probability of annihilation. Indirect search observations, in particular in the case of spin-dependent couplings, are competitive with direct search limits. Combined limits for the $\chi\chi \to b\bar{b}$ process are reported in Fig. 1.6. The regions above the curves are excluded. A more detailed review can be found in Ref. [27].

1.5.4 Search for Dark Matter at colliders

Up to now the discussion has been mostly focused on cosmology and large scale processes both to prove and try to detect Dark Matter. But can LHC and in general colliders provide useful information in this search? The real answer is that no one knows [28]. The possible role of colliders depends on the mass and the interactions of the DM. If a WIMP is considered, where DM is weakly coupled to the SM, it is not straightforward that the energy in the centre of mass

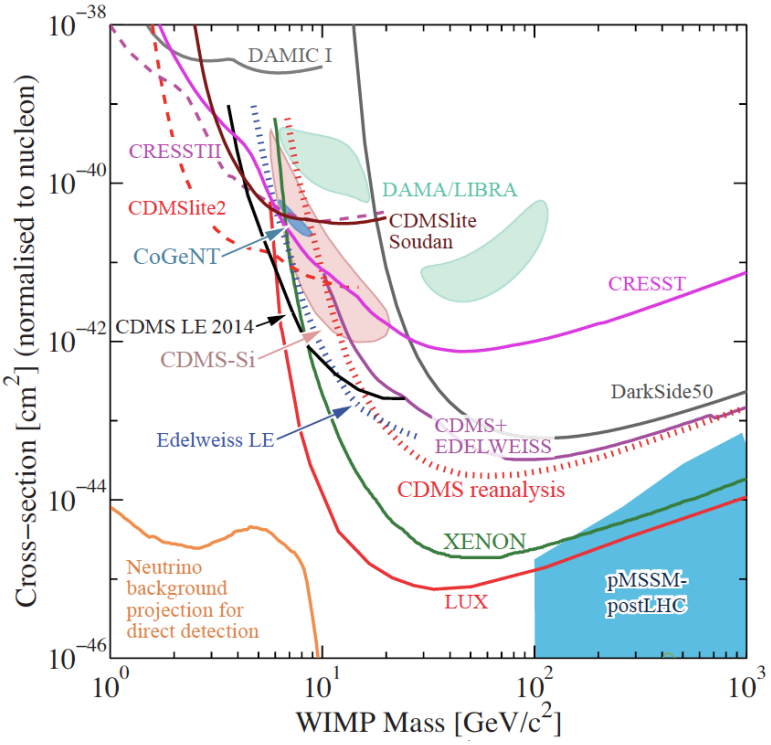

Figure 1.5: Exclusion cross-section limits as a function of the Dark Matter mass in the spin-indipendent case, for various experiments

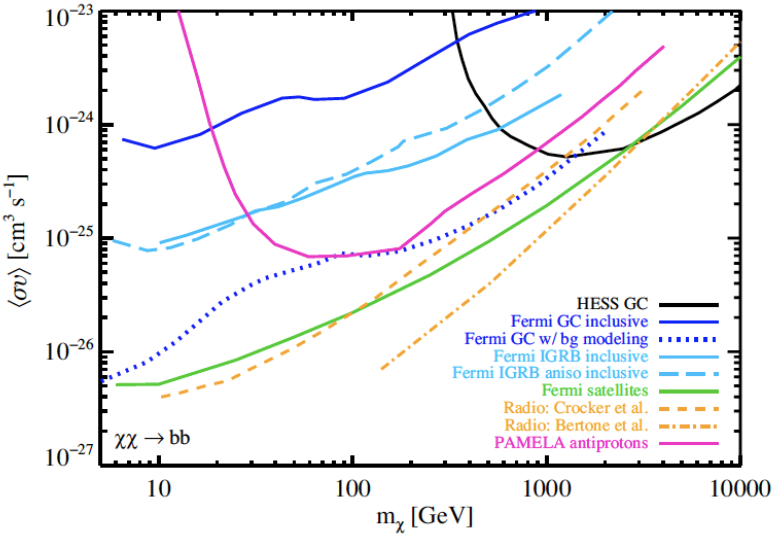

Figure 1.6: Exclusion limits for indirect search experiments as a function of the Dark Matter mass

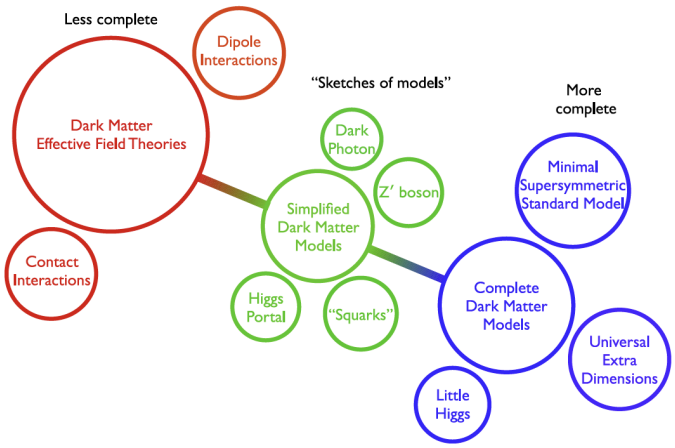

Figure 1.7: Schema of the different possible approaches to the Dark Matter search and their complexities

in the collision is enough to make them kinetically allowed. On the other hand, however, it turns out that the most accredited model describing the observed relic density in the context of an early Universe, and called *thermal freeze out*, points to a dark matter particle with mass and interaction strength within the LHC limits. Another key element to be recalled is that many extensions of the SM, motivated by other reasons, do foresee stable neutral massive particles which could easily assume the properties of Dark Matter. In these models, such as SUSY, however, many other particles and states are accessible together with the Dark Matter candidate, thus making more complex to extract limits directly comparable with direct and indirect searches.
The choice of the modelling approach is mostly driven by the need of minimality, reducing as much as possible the requirements on the new particles, and the plausibility, where, on the other hand, priority is given to models not clearly violating well established principles of particle physics. The two main approaches are grouped under the names of *Effective theories* and *Simplified Models*. In fact, as shown in Fig. 1.7, many different DM models can be built, all having a suitable candidate to solve the Dark Matter puzzle.

Effective theories The earliest and easiest approach is to assume that the only state, beyond the SM, accessible at LHC is the DM particle. In this case the interaction is translated into an effective field theory, a contact interaction, described by only two parameters, the suppression scale Λ and the Dark Matter mass. The advantage of this approach is that the kinematic distributions do not depend on the suppression scale, making very easy to present the results as lower bounds. Moreover, EFT approach is model independent, since there is no need to unveil the whole underlying model.

A typical interaction is described by operators, as an example, of this form:

$$O = \frac{1}{\Lambda^2}(\bar{q}\lambda^\mu\lambda^5 q)(\bar{\chi}\lambda_\mu\lambda^5\chi), \tag{1.6}$$

where χ is a spin 1/2 DM particle. On the other hand, EFT approach has strong limitations. In particular EFT validity is strongly constrained by the momentum transferred: for large values, which is the case at LHC, in particular in future runs, EFT makes unphysical predictions. This can be easily observed by obtaining the previous operator as limit case of a more general theory including a heavy spin-1 particle V^μ coupling to quarks and DM. It can be shown that if the mediator is exchanged in a *s-channel* of a 2-2 process, the matrix element will contain a propagator of the form

$$M \propto \frac{g_q g_{DM}}{m_V^2 - s},$$

which leads to the initial operator only in the case $m_V \gg s$. In this case the suppression scale assumes the form

$$1/\Lambda^2 = \frac{g_q g_{DM}}{m_V^2}$$

If mediator mass is comparable or smaller than momentum transferred, contact interaction does not provide a good description of the kinematics. Another relevant requirement to guarantee the validity of EFT is to remain in the perturbative regime leading to the following relation:

$$m_{DM} \leq \sqrt{\frac{\pi}{2}}\frac{m_{med}}{g_{DM}} \tag{1.7}$$

Simplified models Simplified models extend the range of validity of the EFT approach by introducing a second particle, a mediator, coupling both to the SM and DM sectors. Obviously this means to see the number of free parameters increase. In favour of this approach there is the possibility of describing both hard and soft spectra, overtaking the limitations of EFT approach, by considering both light and heavy mediators. Too heavy mediators make very difficult to obtained the relic density, which was the very first constraint for a Dark Matter search at LHC. Beside of this, Simplified Models should contain a stable, or with a lifetime long enough, particle and a mediator coupling to the two sectors. All the other particles belonging to the dark sector should be energetically inaccessible. The DM simplified models should in general only contain renormalizable terms, consistent with Lorentz invariance and gauge symmetries and they should not violate the global and accidental symmetries in the SM, such as the baryonic and leptonic numbers. In particular Minimal Flavour Violation (MFV) [29] is imposed to curb CP-violating effects. MFV simplified models describing spin-0 exchange, implies couplings to the SM fermions of Yukawa type. A more detailed discussion on the theoretical aspects of Simplified models can be found in [30] or in the LHC Dark Matter Forum recommendations [31].

Chapter 2

The Large Hadron Collider and the ATLAS experiment

In this chapter an introduction to the Large Hadron Collider (LHC) and to the ATLAS experiment is given, in particular providing an overview of the sub-detectors, with particularly emphasis on the muon spectrometer. In addition the ATLAS trigger and data acquisition logic is described, including a summary of the data collected by ATLAS so far. In conclusion the plan for future upgrades is presented.

2.1 The Large Hadron Collider

The LHC is the largest collider in the world [32], located at the *Conseil Europeen pour la Recherche Nucleaire* (CERN). It is housed in the same 26.7 km long tunnel already used by the LEP machine since 1989 [33]. It is designed to collide protons and ions, representing a unique facility for the study of the physics phenomena at high energy scale. The design collisional energy in the center of mass is $\sqrt{s} = 14$ TeV, to be compared with the previous record set by the Tevatron collider (FERMILAB, USA) of 2 TeV [34]. Delivering protons to the required energies (corresponding to 99.9999991% the speed of light) it is not an easy task; a complex system of accelerators is used to increase the protons energy at different stages (Fig. 2.1). The protons are obtained from stripping electrons to hydrogen gas with an appropriate electric field. Protons are then transferred to the Linac2[1], a linear accelerator designed to bring protons to 50 MeV. The second stage of acceleration, where protons get to the energy of 1.4 GeV, is the Proton Synchrotron Booster (PSB), followed by the Proton Synchrotron (PS), were the beam is accelerated up to 25 GeV. The PS also receives ions from the Low Energy Ion Ring (LEIR) to be accelerated. Particles are then sent to the Super Proton Synchrotron (SPS) where they

[1]Linac2 will be replaced with a new Linac4 in 2020. Linac3 is devoted, instead, to the ions acceleration

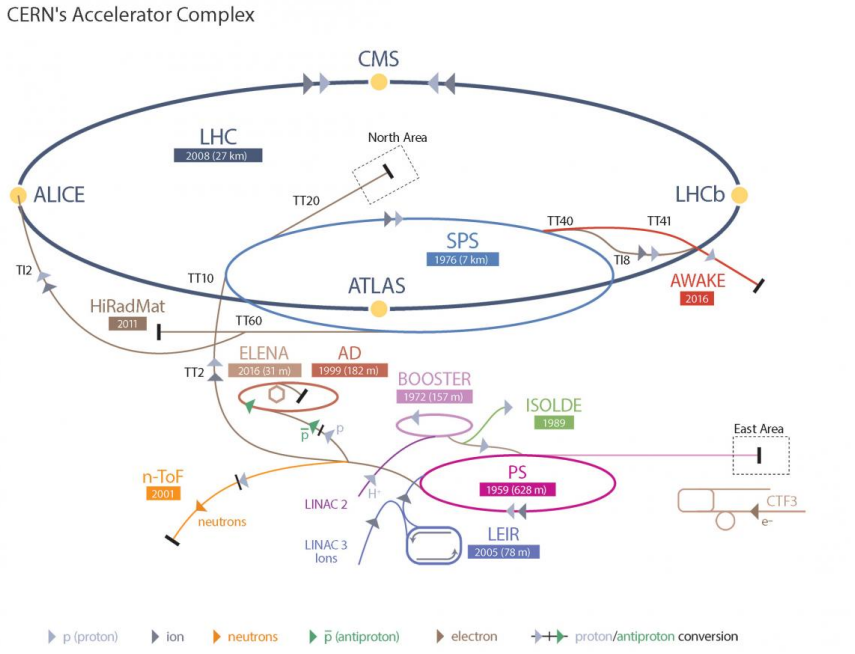

Figure 2.1: The CERN accelerator complex.

finally become suitable for the injection in LHC, at the energy of 450 GeV. Along the ring there are four places where the two proton beams, travelling in separate vacuum pipes, are made collide. At these interaction points detectors have been built: Alice [35], CMS [36], LHCb [37] and ATLAS [38].

2.1.1 LHC performance

The main LHC goal is to study the fundamental laws of Nature by colliding protons. The number of those collisions per second is determined by the luminosity of the beam L and the cross section of the event process under study according to:

$$N_{event} = L\sigma_{event}. \tag{2.1}$$

The luminosity, at its turn, is a function of the beam parameters, and, for a Gaussian beam is given by

$$L = \frac{N_b^2 n_b f_{rev} \gamma_r}{4\pi\epsilon_n \beta*} F \tag{2.2}$$

where n_b is the number of bunches in which the protons are grouped per beam, N_b is the number of protons per bunch, f_{rev} is the revolution frequency and γ_r is the relativistic factor. ϵ_n, the normalized emittance, is defined as $\epsilon_n = \beta_r\gamma_r\epsilon$, where ϵ is called beam emittance and gives a measure of the average spread of the beam in the position-momentum space. $\beta*$ is the value of the beta function at the interaction point. The beta function is related to

the transverse dimension of the particle beam, along the beam trajectory. If a Gaussian beam is assumed, the beta function is related to the width of the beam ($\sigma(s)$) by $\sigma(s) = \sqrt{\epsilon \cdot \beta(s)}$. F is the geometrical luminosity reduction factor, due to the angle of the crossing beams. It can be expressed in terms of the angle and the size of the beams. An indicator of the amount of data, or collisions, having taken place is the so-called integrated luminosity (L_{int}) defined as $L_{int} = \int Ldt$. In Tab. 2.1 the most relevant LHC design parameters are reported. At time of writing the energy in the centre of mass is 13 TeV. On the other hand LHC already reached and improved its design peak luminosity, having reached $2 \cdot 10^{34}$ cm^{-2}s^{-1} already in 2017.

Table 2.1: LHC nominal parameters

Dipole operating temperature	1.9 K
Number of dipoles	1232
Number of quadrupoles	858
Nominal energy, protons	7 TeV
Momentum at injection	450 GeV/c
Peak magnetic dipole field	8.33 T
Current in main dipole	11800 A
Bunch spacing	25 ns
Design Luminosity	$1 \cdot 10^{34}$ cm^{-2}s^{-1}
No. of bunches per proton beam	2808
No. of protons per bunch (at start)	$1.15 \cdot 10^{11}$
Circulating current / beam	0.54 A
Number of turns per second	11245
Stored beam energy	360 MJ
Beam lifetime	10 h
Average crossing rate	31.6 MHz
Number of collisions per second	600 millions
Radiated Power per beam (syncrotron radiation)	6 KW
Total crossing angle (collision point)	300 μrad
Emittance ϵ_n	3.75 mm μrad
Beta function $\beta*$	0.55 m

2.2 The ATLAS experiment

The ATLAS experiment is among the biggest scientific international collaborations ever made. It counts over than 170 institutes involved, spread all over the world. It is a general purpose experiment, designed to cover the widest spectrum of physics searches possible. The dimensions are impressive: its shape is nearly cylindrical, 44 meters long with a radius of about 12 meters. It is located 80 meters underground in an experimental hall located in one of the

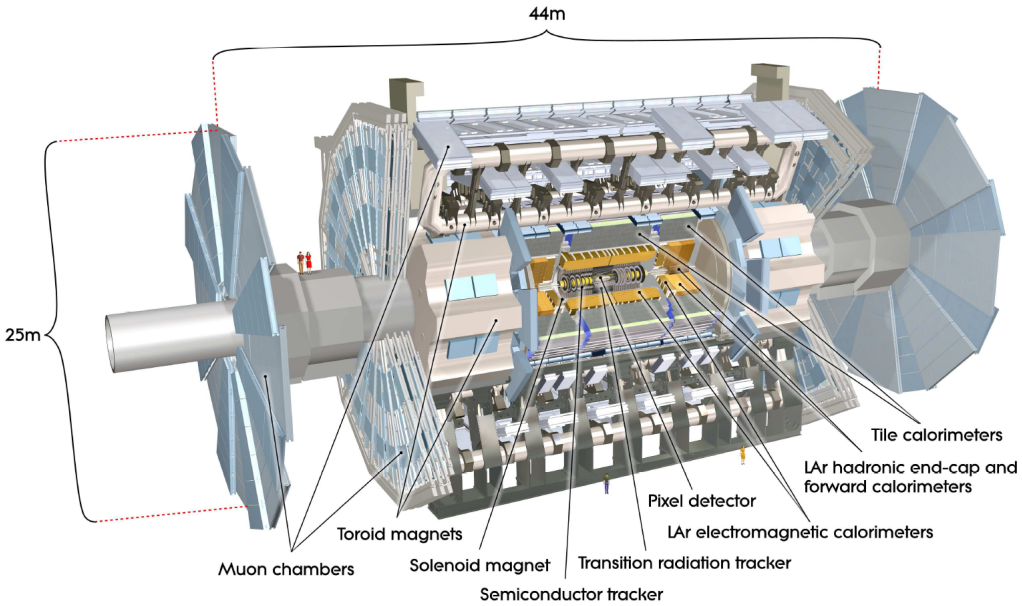

Figure 2.2: The ATLAS experiment.

LHC intersection points near the Swiss-French border. Its weight is of about 7000 tons. Figure 2.2 shows a cut-away of the detector, unveiling it internal onion-like structure; three are the main sub-detectors, the inner detector, the calorimeters, and the muon spectrometer. Each sub-detector is designed to measure different properties of the particles: to measure with high precision the trajectory of charged particles in the inner detector, the energy of electrons and hadrons in the calorimeters and the trajectory of muons in the outermost spectrometer. The detectors are symmetrically mounted with respect to the interaction point (IP) and in such a way to cover the highest solid angle as possible[2]. In addition the inner detector and the muon spectrometer are immersed in magnetic fields, to allow the measurement of the particles momentum given their deflections in two different fields. In the next sections few details concerning each sub-detector is given.

2.2.1 The Magnets

The ATLAS system of magnets [39] is composed of two types of magnets, the solenoid, surrounding the inner detector, and the toroids, located all around the barrel and at the end-caps, outside the calorimeters. The solenoid magnet is 5 meters long with a bore of 2.4 meters and it is build up of a single layer coil. It provides a magnetic field of 2 T. In order to generate such field the coil is cooled down to 4.5 K, by using liquid helium. The three toroids consist

[2]ATLAS uses a dedicated right handed coordinate system centred at the IP. the z axis is the along the beam pipe, the x axis points to the center of the ring, while the y axis looks upwards. In the transverse plane cylindrical coordinate are used (r, ϕ), while the pseudorapidity is defined as $\eta = -ln(tan(\theta/2))$

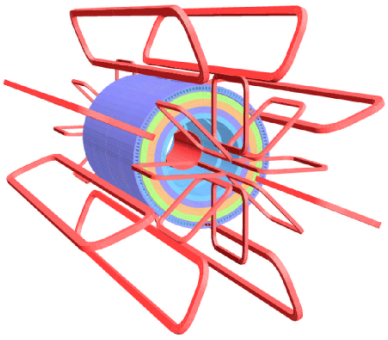

(a)

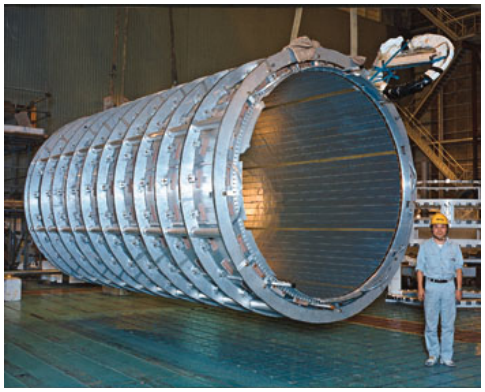

(b)

Figure 2.3: Schema of the magnetic field geometry (a) and picture of the innermost barrel solenoid (b)

of 8 coils each radially assembled with respect to the beam. The coils of the end-cap toroids are rotated by an angle of 22.5 degrees with respect to the barrel ones to provide radial overlap and optimize the bending power. The two end-cap toroids are inserted in the barrel toroid at the end. They are 5 meters long, with an outer diameter of 10.7 m and an inner bone of 1.65 meters. The magnetic field has a peak value of 3.9 T close to the coils and 0.5 at the center for what concerns the barrel toroid, while it reaches up to 4.1 T in the coils for what concerns the end-cap toroids. In both the cases the coils are cooled down by means of liquid helium. A precise knowledge of the field is of extreme importance for the correct evaluation of the particle momentum. More insight can be found in Ref [40].

2.2.2 The inner detector

The layout of the inner detector is shown in Fig. 2.4 [41]. The inner detector is contained in a cylinder 6 meters long with a radius of about 1 meter. As already mentioned in the previous section, a magnetic field of about 2 T is supplied to enhance the bending of charged particles. It covers the region in the pseudorapidity range $\mid \eta \mid < 2.5$. The required tracking resolution is $\sigma_{p_T}/p_T = 0.05\% p_T \bigoplus 1\%$. It is composed of three independent, but complementary detector systems. The closest to the beam, and also where the highest granularity is reached, is the Pixel Detector. It consists of 4 barrel layers (they were originally three before the insertion of the IBL pixel detector in 2014 [42]) and three end-cap disk layers. The intrinsic resolutions in the barrel are 10 µm (R-ϕ) and 115 µm (z), In the end-caps detectors are mounted to provide a resolution of 10 µm (z) and 115 µm (R-ϕ).
Pixels are surrounded by the Semiconductor Tracker (SCT). It consists of silicon strips arranged in four layers in the barrel and nine wheels in the end-caps. In order to reconstruct both coordinates, a 40 mrad angle rotation is adopted

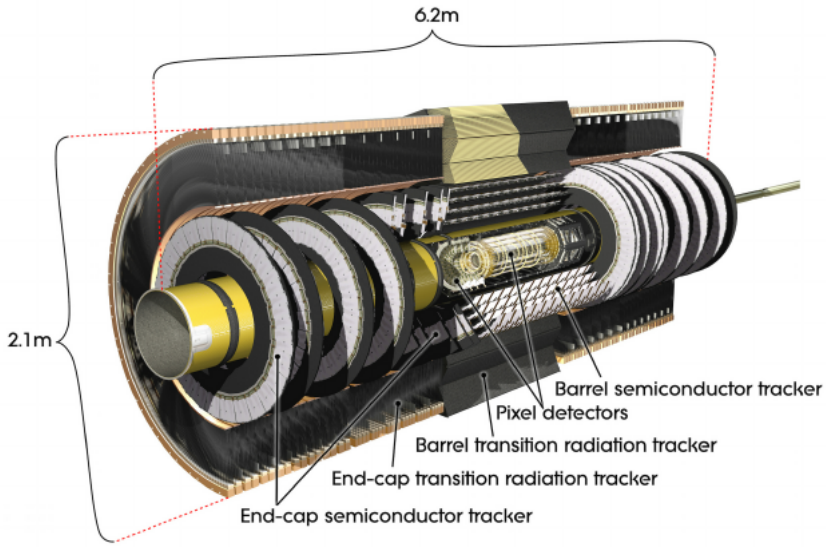

Figure 2.4: The ATLAS inner detector layout.

between different layers of strips. The overall performance of the central station is of 17 µm (R-ϕ) and 580 µm (z) in the barrel. The outermost station is the Transition Radiation Tracker (TRT). It consists of three cylindrical layers in the barrel and 8 wheels in the end-caps of drift tubes. Each straw is 4 mm in diameter with a central gold plated tungsten wire of about 30 µm. This subdetector allows to discriminate between the energy lost by particle ionization and transition radiation losses, contributing to particle identification.

2.2.3 Calorimeters

The inner detector is surrounded by calorimeters. A cut-away of the ATLAS calorimeter system is shown in Fig. 2.5. The innermost is the electromagnetic calorimeter [43], designed to reach an energy resolution of $10\%/\sqrt{E(GeV)} \bigoplus 1\%$. It consists of a sampling structure of lead as absorber and LAr as active material, with the absorber showing an accordion shape. The barrel electromagnetic (EM) calorimeter extends up to $\eta = 1.474$, for a total thickness of 22 X_0. Higher η are covered by the EM end-cap calorimeter, up to $\eta = 3.2$. Also in this case an accordion shape absorber and active material is used, assembled in two wheels in each end-cap cryostat. The hadronic Tile calorimeter [44] sorrounds the EM calorimeters in the barrel region, up to $\eta = 1.7$. It is designed to provide precise measurement of jets, taus, hadrons with a resolution of $50\%/\sqrt{E(GeV)} \bigoplus 3\%$. It consists of a sampling structure, where iron is used as the absorber and scintillating fibres as the active medium. In the forward region, due to the higher particle flux expected, tiles are replaced by LAr and copper is used as absorber. The hadronic end-cap calorimeter matches the pseudorapidity coverage of the electromagnetic ones, sharing the same cryostat. Finally, in the very forward region, covering up to $\eta = 4.9$

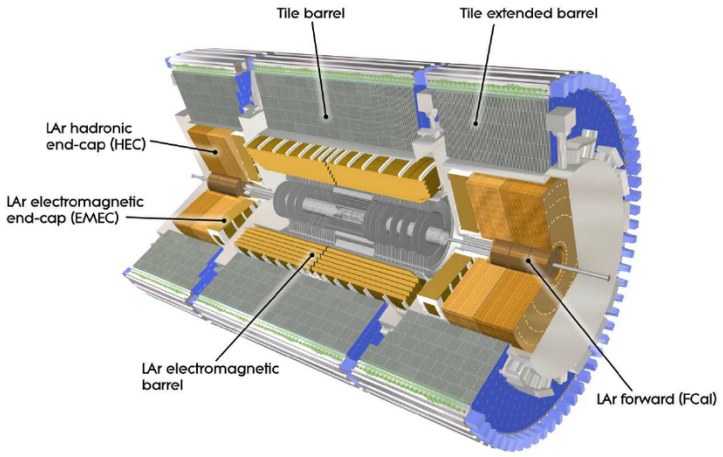

Figure 2.5: The ATLAS calorimeters layout.

the LAr forward calorimeter (FCal) is located. It is designed to provide both electromagnetic and hadronic energy measurements and it uses copper and tungsten absorbers and LAr as active material.

2.2.4 The Muon spectrometer

The muon spectrometer [45] constitutes the outer part of the ATLAS detector and is designed to detect charged particles exiting the barrel and the end cap calorimeters in the pseudorapidity range $\mid \eta \mid < 2.7$. It is designed to measure the muon transverse momentum with a resolution of $\sigma p_T/p_T = 10\%$ at $p_T = 1$ TeV. In these regions, as already described in the previous section, a toroidal magnetic field is provided, both in the barrel and end-caps. The momentum of a particle can be obtained by measuring the curvature of the particle bending in the magnetic field. High momentum implies low curvature. To measure the transverse momentum the method of the sagitta, which is defined as the maximum deviation of a circle from a straight line, is used. For a 1 TeV muon, given the configuration of the magnetic field, the expected sagitta is around 0.5 mm. This leads to an overall uncertainty on the measurement of the sagitta of 50 µm. The design of the muon spectrometer is shown in figure 2.6. The muon detectors in the barrel are organized in three concentric stations equipped with Monitor Drift Tube chambers (MDT) at a radius of about 5, 8, 10 meters from the beamline. MDT chambers consist of six (middle and outer stations) to eight (inner station) layers of drift tubes. An average resolution of 80 µm per tube and 35 µm per chamber is achieved. The middle and the outer stations are equipped also with Resistive Plate Chamber (RPC) detectors to provide the trigger signal. RPCs are located on both sides of the middle MDT station, and directly inside the outer MDT station. A schematic view of the cross section of the barrel muon system is shown in figure 2.7.

In the forward direction three independent wheels are mounted perpen-

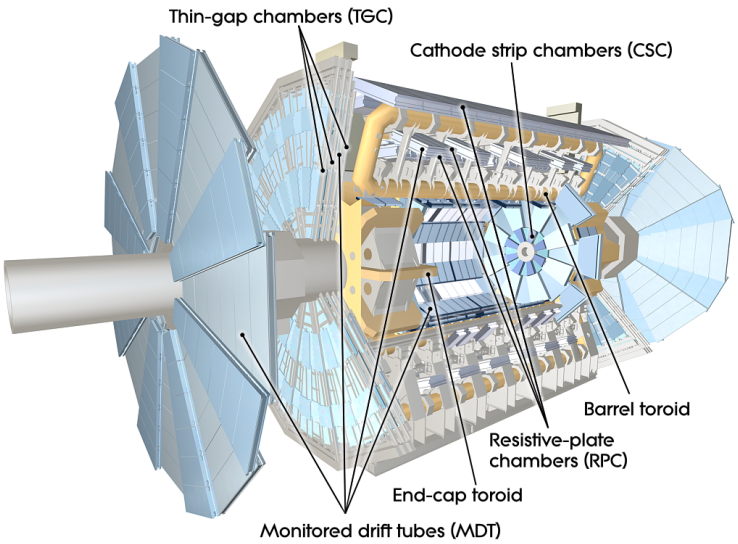

Figure 2.6: The ATLAS muon spectrometer layout.

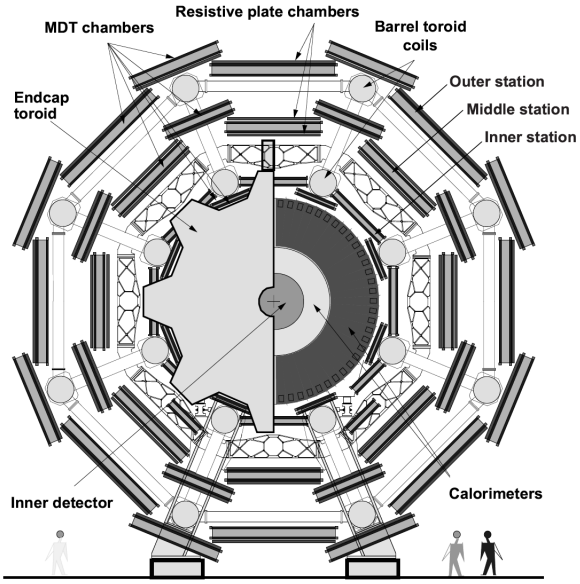

Figure 2.7: Schematic view of a cross section of the barrel region.

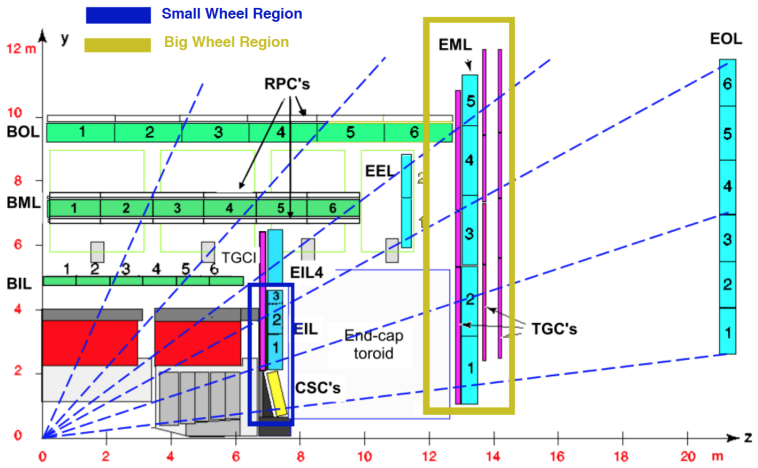

Figure 2.8: Longitudinal view of the muon spectrometer showing the three concentric stations at different distance (5, 8, 10 meters) from the interaction point. The innermost wheel, the so called Small Wheel, is outlined

dicular to the beam axis at a distance of 7.5, 14 and 22.5 meters. The two outermost wheels are equipped with MDTs for the reconstruction. The central wheel, called Big Wheel, is also equipped with two Thin Gap Chambers (TGCs) doublets and one triplet to provide the trigger signal. A schematic view of a cross section of the muon spectrometer in a plane along the beam axis is shown in figure 2.8. The innermost wheel, the so called Small Wheel, is equipped with Cathode Strip Chambers (CSCs) in the part closest to the beam, and MDTs in all the rest for the measurement of the most accurate coordinate (η coordinate) and TGCs for the second one. In table 2.2 the main characteristics of the four subsystems forming the muon spectrometer are reported. Each subsystem is described in more details in the following section.

Table 2.2: Table reporting the characteristics of the four different technologies used in the ATLAS muon spectrometer. Due to space constraints acronyms have been used. The technologies are: Monitored Drift Tube (MDT), Cathode Strip Chamber (CSC), Resistive Plate Chamber (RPC), Thin Gap Chamber (TGC).

Type	Function	Coverage	Res (z)	time Res
MDT	tracking	$\mid \eta \mid < 2.7$	35 μm (R/z)	
CSC	tracking	$2.0 < \mid \eta \mid < 2.7$	40 μm (R), 5 mm ϕ	7 ns
RPC	trigger	$\mid \eta \mid < 1.05$	10 mm (R/ϕ)	1.5 ns
TGC	trigger	$1.05 < \mid \eta \mid < 2.7$	2-6 mm (R) 3-7 mm ϕ	4 ns

Monitored Drift Tubes

Precision tracking in the muon spectrometer is mainly performed by Monitored Drift Tubes (MDTs). They consist of 3 mm cylindrical drift aluminium tubes, with a 30 µm tungsten-rhenium wire placed in the center with a precision better than 10 µm. Tubes are filled by Ar/CO_2(93:7) gas mixture and are operated at 3 bar overpressure. Electrons resulting from gas ionizations drift towards the wire where they also amplify. The voltage applied is about 3.1 kV, resulting in an amplification of $2 \cdot 10^4$. A single chamber is composed of six to eight layers of tubes, each with a spatial resolution of 80 µm. The length of the tubes goes from 0.9 m to 6.2 m. MDTs are used both in the barrel and end-caps muon stations, except for the closest one to the IP, the Small Wheel, for $2.2 <| \eta |< 2.7$ where they are replaced by Cathode Strip Chambers due to the very high rate. More then 70000 tubes have been produced to equip the detector.

Cathode Strip Chambers

Cathode Strip Chambers (CSCs) are the tracking detector in the innermost part of the end-cap muon station (Small Wheel) closest to the interaction point. They are adopted where the particle rate exceeds the MDTs limit (150 Hz/cm^2). They consist of multi-wire proportional chambers, with both cathodes segmented, one with strips parallel to the wire, and the other perpendicular. The gas gap is of 5.08 mm, as the cathode readout-out pitch, while the anode wire pitch is of 2.54 mm. The overall CSC resolution per layer is of about 50 µm on the precise coordinate and few millimetres on the second one. The gas mixture used is $Ar/CO_2/CF_4$ (30:50:20). The maximum drift time is of 30 ns.

Resistive Plate Chambers

The Resistive Plate Chambers (RPCs) are the detectors designed to provide the trigger signal in the barrel region. Each of the three concentric muon stations in the barrel are equipped with two independent planes of RPCs, measuring η and ϕ of the tracks. Redundancy is obtained to reject fake hits and improve the trigger efficiency. RPCs are parallel planes detectors: the gas gap is of 2 mm, defined by cylindrical spacers placed every 10 cm and the electrodes are made of a mixture of phenolic resins (bakelite) which has a resistivity of $2 \cdot 10^{10}$ Ωcm. A graphite coating is applied with a surface resistivity of ≈ 100 kΩ, allowing uniform distribution of the high voltage. Between plates an high electric field is applied (4.9 kV/mm) allowing avalanches formation towards the anode. Bakelite surfaces are, moreover, covered by linseed oil, to guarantee the required smoothness. Signal is induced on copper strips mounted on the outer faces of the resistive plate and read-out via capacitive coupling. Typical width of the readout strips is of about 30 mm. The gas mixture used

is $C_2H_2F_4/C_4H_10/SF_6$ (94.7:5:0.3). Spatial resolution is limited by the strip width.

Thin Gap Chambers

The trigger in the forward region is provided by the Thin Gap Chambers (TGCs). They are mounted on the middle wheels (big wheels) in seven different layers to provide redundancy and in the inner wheels. The TGC detector technology is based on multi-wire proportional chambers characterized by an anode wire to cathode plane gap distance of 1.4 mm and 1.8 mm wire-to-wire spacing. Detectors are operated in quasi-saturated mode, leading to a typical signal rising time of 5 ns. The gas used is a mixture of 45% n-Pentane and 55% $C0_2$. The detector is operated at 3.0 kV for a gas gain of about 10^6. Between 4 and 20 wires are grouped together to fed a common readout channel. Behind the cathode planes, on one side precision copper strips run perpendicularly to the wires, with a pitch ranging from 15 to 49 mm.

2.2.5 The ATLAS Trigger and data acquisition system

The ATLAS Trigger system [46] is a crucial part of the ATLAS experiment, being responsible for the selection of interesting events reducing the recording rate from the LHC bunch crossing rate of about 40 MHz to 1 kHz. A schema of the current ATLAS trigger system is provided in Fig. 2.9. Major changes have been introduced between the first data taking period (Run 1, 2010-2012) and the second one (Run 2) started in 2015. A detailed description of the old trigger structure can be found in [47] for reference. It currently consists of an hardware level first trigger (called Level 1, or L1) and a software one, called HLT. The L1 trigger reduces the event rate to about 100 kHz, providing a decision in less than 2.5 µs. It uses information from the muon system (L1 Muon), partial data from calorimeters (L1 Calo) and from the topological trigger module (L1Topo) which calculates basic physics quantities given the information provided by the detectors. The decision is taken at the Central Trigger Processor (CTP); if accepted, event data are transferred from the Read-out Driver (ROD) to the Read-Out System (ROS) for the HLT selection. The HLT selection is driven by the analysis of the Region-of Interest (RoI) identified by the L1 trigger logic. At this stage all the detector information within the RoI first, and then from the whole detector is used. This second step reduce the rate up to 1 kHz. Events accepted for local saving are then transferred to the event-building system, and finally to be written to a permanent storage.

2.2.6 The road to now

Despite of long future we have in front of us, LHC and ATLAS already have quiet a long history behind. The first part of Run 1 data taking period, in 2009 and 2010, has been mainly devoted to the commissioning of the machine and

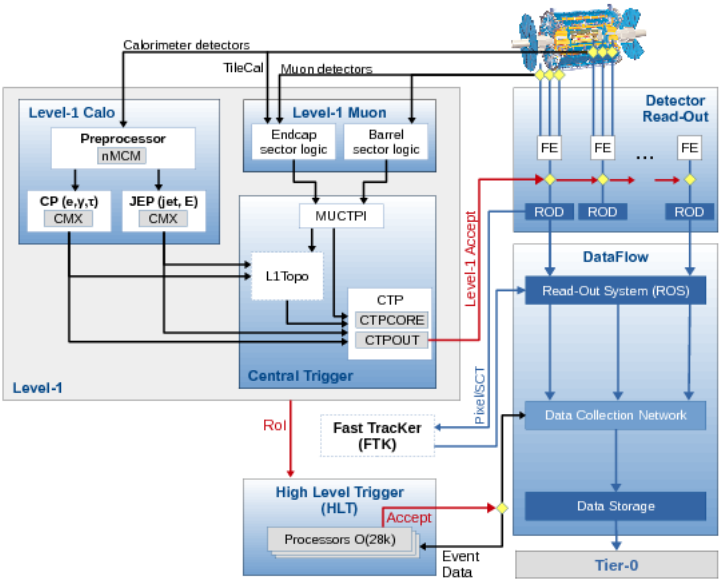

Figure 2.9: The ATLAS Trigger system.

the exploiting of its potential. The first collision took place on March, 30th 2010 at 7 TeV in the centre of mass. Several months of commissioning and test followed to allow increasing the beam intensity. At the end of the year 368 bunches with 10^{11} protons each were circulating in LHC for a peak luminosity of $2.1 \cdot 10^{32}$ cm^{-2}s^{-1}. In 2011 the number of bunches was increased to 1380, reaching a bunch spacing of 50 ns, further increasing the beam intensity and improving the machine parameters. By the end of the year a peak luminosity of $3.7 \cdot 10^{33}$ was reached, allowing ATLAS to accumulate 5 fb^{-1}. The 2012 saw the increase of the centre of mass energy to 8 TeV. Integrated luminosity was about 1 fb^{-1} per week. By the end of 2012 ATLAS accumulated about 20 fb^{-1} 2.10. More than two years passed without beams circulating, completely dedicated to the upgrade of the machines for pushing the limits reached in Run 1 and improve the performance. In 2015 the beam energy has been increased up the current value of 6.5 TeV (centre of mass energy of 13 TeV) and, by the end of the year, 2240 proton bunches per beam were circulating in the accelerator for an integrated luminosity of 4 fb^{-1}. In 2016, the energy did not change, but the outstanding LHC performance allowed to set new limits and integrate almost two times the expected luminosity. In October, when beams stopped circulating, 40 fb^{-1} were recorded by ATLAS (Fig. 2.11a). The reason is mainly the very high availability of the accelerator and injectors: the accelerator was colliding protons almost 50% of the time. 2017 has been a great year for LHC as well. The integrated luminosity exceeded the initial previsions, despite of many serious problems to the machines. ATLAS recorded about 50 fb^{-1}, given that 40 were expected at the beginning. What is more remarkable is the record on the peak luminosity reached: $2.06 \cdot 10^{34}$ cm^{-2}s^{-1}. This value is more than twice the design value of the LHC machine. At time

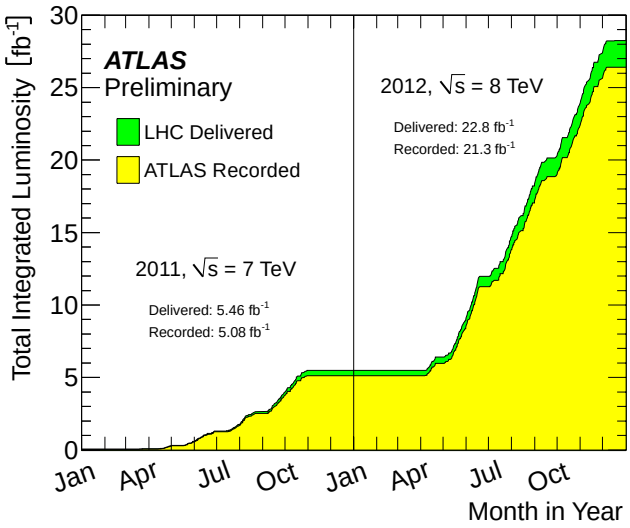

Figure 2.10: LHC delivered and ATLAS recorded integrated luminosity in Run 1 [48].

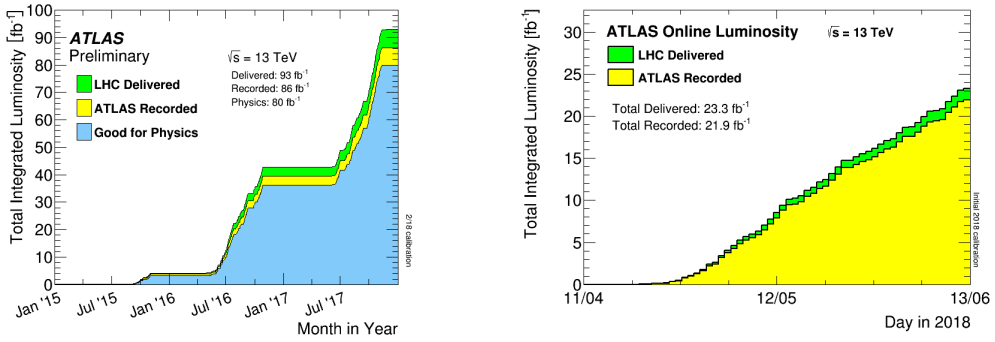

(a) (b)

Figure 2.11: Integrated luminosity years 2015-2017 (a). Integrated luminosity in 2018 at time of writing (June 2018) (b).

of writing, June 2018, we are in the middle of 2018 data taking. The aim is to collect even more data than in 2017, expecting about 60 fb^{-1} collected by the experiment. A peak luminosity of $2.14{\cdot}10^{34}$ cm^{-2}s^{-1} has been already reached for an integrated luminosity of about 20 fb^{-1} (Fig. 2.11b).

2.2.7 Plans for upgrade

The successful LHC operations up to now should not distract from what is still in front of us. An extremely ambitious upgrade programme of the machines is planned in 2022-2023, with some aspects anticipated in the long shutdown 2, in 2019 [49]. The aim is to reach peak luminosity of 5 times the initial design values, and an integrated luminosity of about 3000 fb^{-1} in a dozen years after the upgrade. In other words, data taken up to now will be completely negli-

gible. Upgrades will involve triplet magnets, possibly suffering from radiation damage, cryogenics, collimators, and the replacement of two dipoles with new ones shorter, but producing a stronger magnet field; this will allow to save space for supplementary collimators. This ambitious upgrade programme does affect also the detectors. Increasing the luminosity will imply an higher number of interactions per beam crossing (*pileup*). The expected value at High Luminosity LHC (HL LHC) is of about 140 interactions per beam crossing, to be compared to the 30/40 we have today [50]. This will imply that the particle rate in the detector will increase and it will not be sustainable for many of them. During the two long shutdown periods (LS2 and LS3) ATLAS will undergo major upgrades, called Phase I [51] and Phase II respectively [52]. The most important upgrade project during Phase I is the New Small Wheels project, consisting of the replacement of the innermost muon station in the end-caps, the Small Wheels, with a completely new detector technology (Micromegas) and an improvement of the TGCs detectors, called Small TGCs (sTGCs). More details about this project will be given in the next chapter. Another important project is the Fast TracKer (FTK), based on associative memories designed to improve the particle identification, to maintain low trigger rates and high efficiency for electrons and muons and provide more flexibility for identifying new physics signatures. During the Phase II the biggest upgrade consists in the replacement of all the Inner Detector with a silicon brand new one, called Inner Tracker (ITk). ITk will have a large impact on physics performance, extending the coverage of the inner detector, reducing the forward jets pileup and improving the vertexing capabilities. In the meantime the trigger logic will be revised and improved and the electronics of many subdetectors will be replaced.

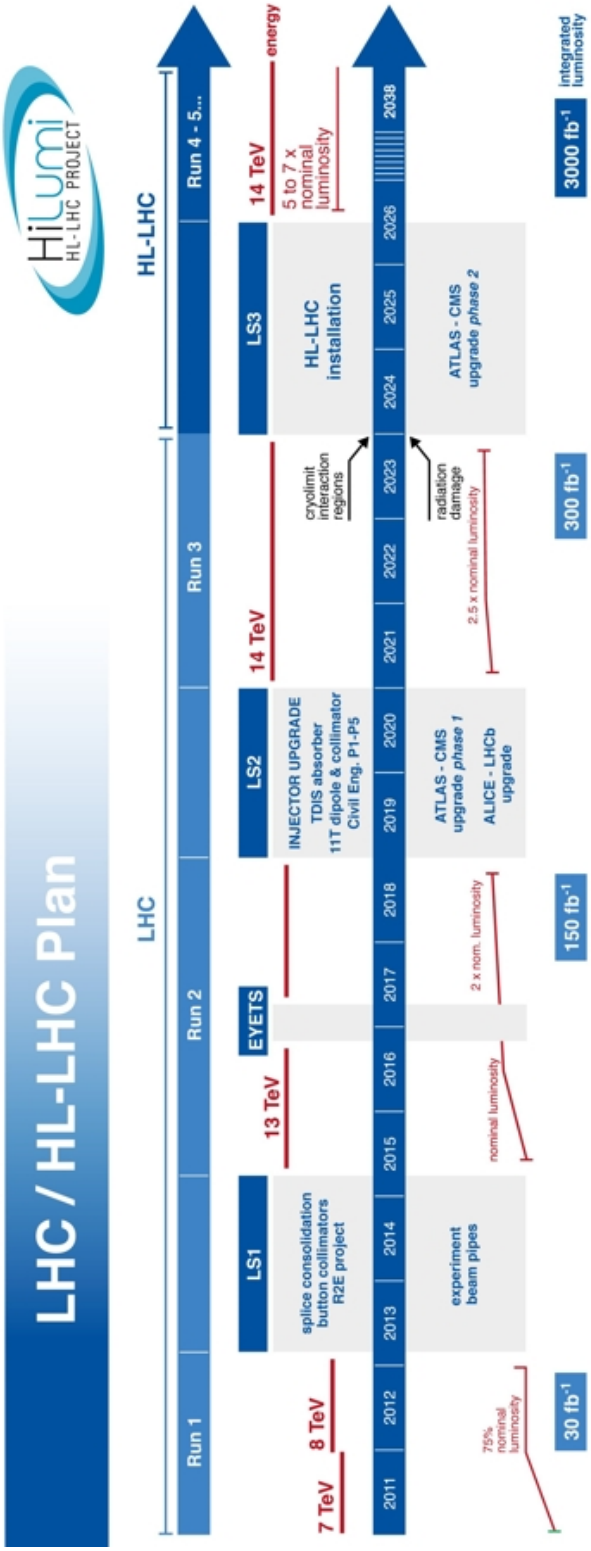

Figure 2.12: LHC: plans for a (brilliant) future

Chapter 3

The New Small Wheels Project (NSW)

In this chapter the main aspects of the New Small Wheels upgrade project will be reported in particular focusing on the physics requirements of the new detector technologies and benefits, followed by a brief description of the Micromegas technology. The main reference for the first part of the chapter is the NSW Muon TDR [53].

3.1 Introduction

As already introduced in the previous chapter, where the ATLAS general upgrade plan has been presented, one of the most relevant Phase I upgrade of the experiment consists in the replacements of all the detectors currently installed in the innermost muon station in the forward regions, the so-called *Small Wheels*. Fig. 3.1 shows a picture of a Small Wheel currently installed in ATLAS where are clearly visible the two detector technologies employed: CSC and MDT.

The upgrade is motivated by at least two main reasons. The first reason concerns the need of improving the Level-1 muon trigger logic in order to discard the fake muon triggers produced by particles not coming from the Interaction Point (IP), without reducing the acceptance and trigger efficiency. Such upgrade requires to include the information from the Small Wheels in the trigger logic, thus requiring an improvement of the detector performance. The second one is related to the expected degradation of the performance of the detectors currently installed due to the higher particle rate foreseen in the next years of LHC operations. The consequences of this effect have been studied in particular concerning the MDT tracking chambers and will be discussed in the next section. CSCs are, at their turn, affected by the increased particle rate and an improvement of the performance is required to fulfil the high accuracy ATLAS requirements for the coming years.

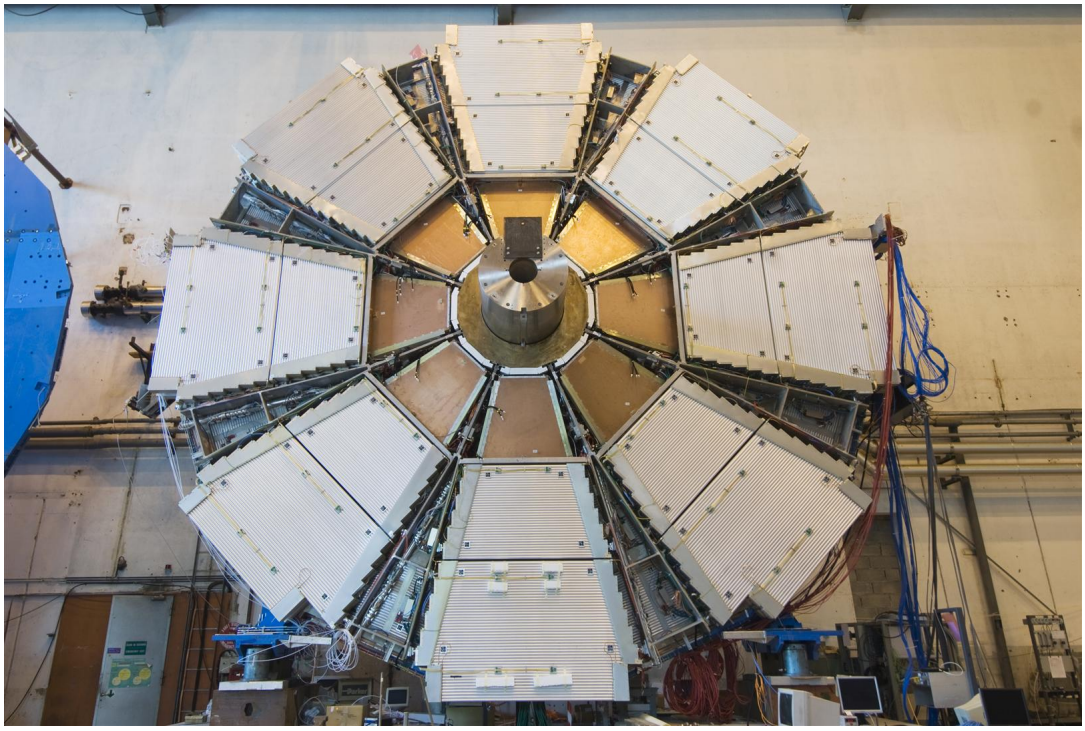

Figure 3.1: Picture of a Small Wheel currently installed in ATLAS. MDT and CSC detectors are installed at different η ranges

3.2 Trigger performance and requirements

During Run 1, the end-cap muon trigger was provided by the TGC chambers installed in the second forward muon station (middle wheel), resulting in a large contribution of tracks not coming from the interaction point. Figure 3.2 shows the η distribution of the Level 1 muon trigger signals having transverse momentum of at least 10 GeV. The subset of those actually reconstructed as real muons in the offline analysis is also reported. More than 80% of the triggered events are not associated with a reconstructed muon.

At higher luminosity, as expected in LHC in the next years, the fake trigger signals will increase and eventually saturate the full bandwidth (100 kHz) available for the Level 1 trigger. During Run 2 a first improvement of the trigger logic has been performed, resulting in a reduction of 60% of the trigger rate with only a 2% reduction of the efficiency to real muons [54]. This result has been achieved adding an additional TGC coincidence in the region $1.3 <| \eta |< 1.9$ in the Small Wheels, or a TGC/Tile Calo coincidence to cover the pseudorapidity region $1.0 <| \eta |< 1.2$. Figure 3.3 shows a schematic view of the new trigger logic, with an indication of the various pseudorapidity regions. The curved arrow represents a slow particle generated in the beam pipe, hitting the TGC in the middle station, but not the ones in the innermost: events of these types are thus rejected.

Despite of the big improvement on the fake trigger rejection, a further effort

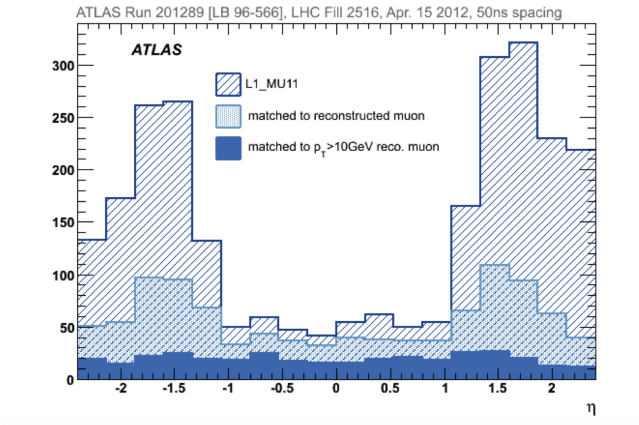

Figure 3.2: Distribution as a function of η of the level 1 trigger signal for muons having p_T if at least 10 GeV. In the plot the muon candidates reconstructed in the offline analysis are also reported

is needed to satisfy the requirements of the future runs with higher luminosity. The upcoming New Small Wheels are expected to maintain a Level 1 trigger rate below 20 kHz, without any off-line cut or acceptance reduction which would affect the physics analyses.

3.3 Precision tracking performance

The second, important, reason for the upgrade is that a sizeable reduction of the performance of the detector, such as the MDTs, is expected at a luminosity higher than $3{\cdot}10^{34}$ cm^{-2}s^{-1}. This is due to the fact that local charges in the gas reduce the effective field in the tubes, inducing a lower amplification and a loss of efficiency. At moderate rate this effect is negligible, since the local charges due to an ionizing particle are absorbed before the next particle arrives. In particular the entity of the reduction has been studied at test-beam and it is shown in Fig. 3.4(a). A single tube starts to lose efficiency even at low rate, reaching an inefficiency of about 35% at 300 kHz. Since a MDT chamber is actually composed of many tubes, the efficiency reduction is less pronounced, leading anyway to an unacceptable reduction of the performance above 300 kHz. Figure 3.4(b) shows the rate expected as a function of the distance for a luminosity of $3 \cdot 10^{34}$ cm^{-2}s^{-1}, as seen in the MDT and CSC chambers, with an indication of the 300 kHz threshold per tube previously mentioned. A large fraction of the MDTs would need to operate at rate higher than 300 kHz.

3.4 NSW requirements

In order to fulfil the ATLAS requirements, maintaining at high rate during High Luminosity LHC (HL-LHC) the same performance as now, the new de-

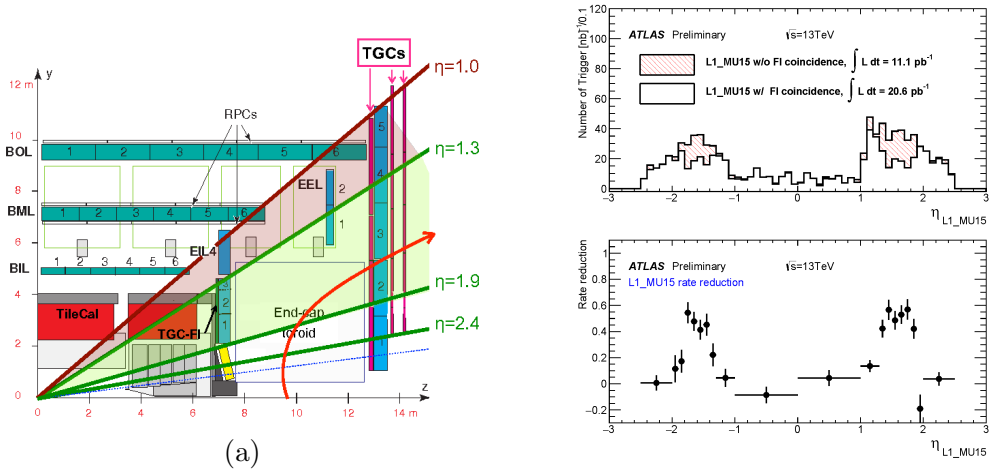

(a) (b)

Figure 3.3: End-cap muon trigger logic schema in Run II: a coincidence with TGCs in the Small Wheels is required to discard fake triggers (a). Number of triggers as a function of η with and without the requirement of the additional coincidence (Top) and fractional event rate reduction (bottom)

tector technologies for precision tracking should provide:

- Reconstruction of muons tracks with a spatial resolution better than 50 µm. This will assure an overall momentum resolution of 10% for 1 TeV muons
- Efficiency in finding muons better than 97% for muons with p_T greater than 10 GeV
- Efficiency not degrading at very high momenta
- Measurement of the second coordinate with a resolution of at least 2 mm

The requirements in order to keep the L1 trigger rate below the 20 kHz available rate are summarized as following:

- The information should arrive to the Sector Logic (the muon trigger electronics) not later than 1.088 microseconds after a collision which is the latency of the current TGC signals from the Big Wheels.
- Track segment reconstruction should have an angular resolution of 1 mrad or better.
- Track segments should have a granularity better than 0.04x0.04 in the η-ϕ plane to match the current muon trigger system
- The overall reconstruction efficiency should be at least 95%
- Track should be reconstructed in the full coverage of the detector

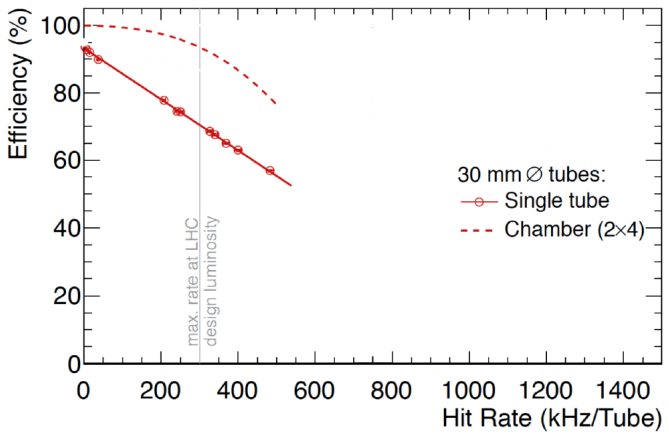

(a)

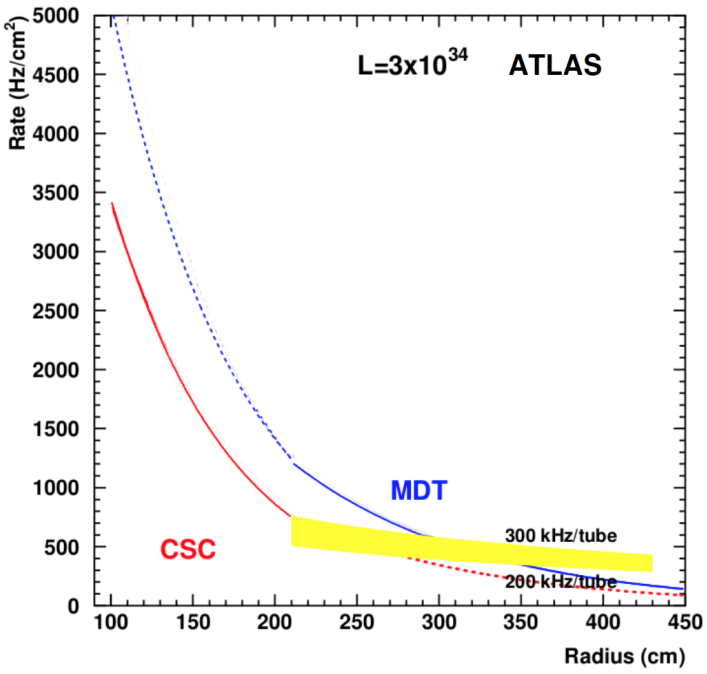

(b)

Figure 3.4: (a) Efficiency of MDTs at testbeam as a function of the particle rate (tubes and chambers). (b) Rate expected as a function of the distance at a luminosity of $3{\cdot}10^{34}$ cm^{-2}s^{-1}. Indication of the equivalent rate expected in the MDTs is also reported.

3.4.1 NSW ageing requirement and expected background

Another important requirement of the new detector technologies, involved in any planned future upgrade, is the capability to run in very harsh and radioactive environments without a considerable reduction of the performance for all the detector lifetime. In the case of the NSW, this lifetime is about 10 years at the maximum HL-LHC luminosity. In this condition the maximum particle rate of minimum ionizing particle (MIP) is expected to be of about 15 kHz/cm^2. If the energy deposed by a MIP in a standard Micromegas structure (see next section) is considered, recalling some concepts described in App. A, the charge accumulated due to a MIP can be calculated as follows:

$$Q_{MIP} = \frac{E_{MIP}}{W_i} q_e G \tag{3.1}$$

where $E_{MIP} \sim 1.25$ keV, W_i is the ionization energy which, for an Argon-CO_2 mixture, has a value of about 26 eV, q_e is the charge of the electron, and G is the detector gain, around 5000. If these values are used, a charge produced by a MIP is about 40 fC. Considering the particle rate expected in HL-LHC this brings to a total accumulated charge of about 50 mC/cm^2 for 10 years of operations. Other smaller contributions to the background are also expected from alpha particles, neutrons, and highly energetic photons [55].

3.5 NSW Design

Two detector technologies have been chosen to fulfil the resolution, efficiency and latency requirements: the Micro Mesh Gaseous Structure (Micromegas) and the Small Thin Gap Chambers (sTGCs). The project foresees a robust, redundant tracking system, where the two technologies complement each other. The Micromegas detectors are mostly devoted to high precision muons tracking, while sTGCs are mainly contributing to provide the trigger signal. Each wheel will be composed of sixteen sectors, eight large (LM) and eight small (SM), slightly overlapping to maximize the acceptance. Each sector consists of two Micromegas and two sTGCs wedges separated by a central spacer frame. The wedges are arranged to maximize the distance between the sTGC detectors (sTGC-MM-MM-sTGC). A layout of the NSW structure, both seen from the IP and from the HO side is show in Fig. 3.5. Each Micromegas wedge, at its turn, is segmented into two modules, called SM1 and SM2 (if belonging to the small sectors) or LM1 and LM2 if belonging to the large ones. Concerning the sTGCs, each wedge is segmented into 3 modules. The structure of a sector is schematically shown in Fig. 3.6 A single module is not a single detecting plane, but a quadruplet, providing four independent layers of measurement. In average a particle will, given the structure just described, cross at least 8 layers of Micromegas and 8 layers of sTGCs. The design also satisfies the requirement of being compatible with the current tracking detectors and with

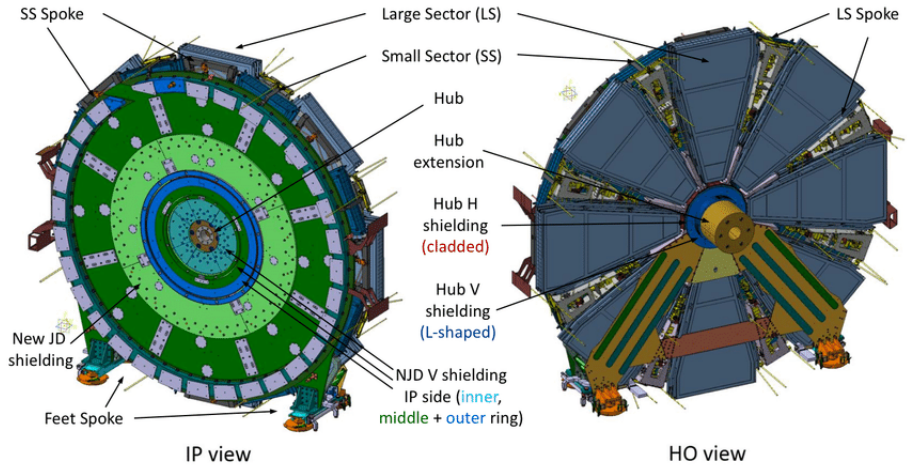

Figure 3.5: Layout of the NSW seen from the IP and the HO side

the end-cap alignment system. The entire wheels are expected to be assembled on the surface, and then installed in the cavern.

3.6 Micromegas technology

Micromegas [56] is a relatively new detector technology belonging to the category of Micro Gaseous Pattern Detectors (MPGDs). Those detectors have been designed to overcome limitations of the wire-based gaseous detectors, mainly concerning the high rate capability, the ageing and the resolution limited by the wire spacing. The common element among all the MPGDs is being based on Printed Circuit Boards (PCB) combined with photolitographic techniques, allowing to manipulate very thin layer of materials. This technology profits of the large experience accumulated in other fields and it is changing the paradigm of gaseous particle detectors, improving their limits. Many large experiments are now upgrading or foreseeing to upgrade their detectors with MPGDs.

The original Micromegas consists of a drift electrode, a gas gap where the particles convert of about 5 mm, called *drift region*, a metallic mesh and a cathode layer where the signal is readout. The metallic mesh is kept at a well defined distance from the readout by insulating pillars (typical length $\sim$ 0.1mm). An electric field is applied both between the drift electrode and the mesh, and between the mesh and the readout. Typical values of the fields are 100 V/cm and 50 kV/cm respectively. In the drift region ions and electrons move towards the electrodes, while the amplification takes place only between the mesh and the readout. The role played by the pillars is thus critical. Recalling the theory of the Towsend coefficient (App. A), the amplification of the detector depends exponentially on the distance. A small variation of the distance between readout and mesh determines large variations of the electric

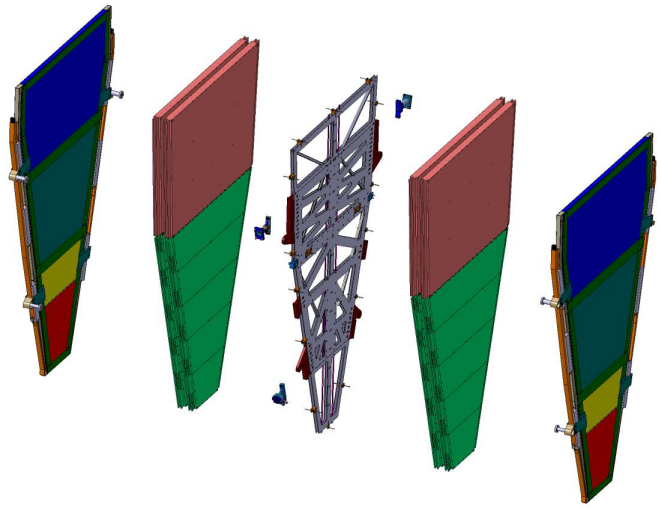

Figure 3.6: Layout of a sector. Two Micromegas and two STGC wedges are separated by a central spacer frame. Each wedge is composed of 2 or 3 modules, depending if Micromegas or sTGC respectively

field, resulting in detector instabilities. A weak aspect of this structure is to be extremely sensible to sparks. Sparks occur when the multiplication reaches values close to the Raether-limit, where the gas becomes conductive having exceeded its breakdown limit. In this situation sparks can damage the electrode and lead to long deadtime due to the time needed to collect all the charges. ATLAS developed a protection schema, to decrease the impact of sparks in the detectors, consisting of a thin layer of insulating material on top of the readout copper strips, covered, at its turn, by a layer of carbon resistive strips, retracing the path on the underlying copper strips. In this configuration the voltage is applied between the mesh and the resistive strips. The signal is readout via capacitive coupling from the underlying copper strips. A schematic description of the working principle and some of the main aspects of a resistive Micromegas are reported in Fig. 3.7.

3.7 Micromegas for the NSW upgrade

As already described in 3.5, the NSW project foresees 16 sectors, 8 of them called small and 8 large, each one composed of two wedges for each detector technology (2 Micromegas and 2 sTGS), separated by 40 mm thick spacer frame. Each wedge, at its turn, contains a sTGC and a Micromegas quadruplet. A quadruplet provides 4 independent detection layers, arranged in a single structure. Depending of their dimensions, 4 types of quadruplets have been designed: LM1 and LM2 (Large sectors) and SM1 and SM2 (Small sectors). The construction of the quadruplets is responsibility of four consortia, INFN

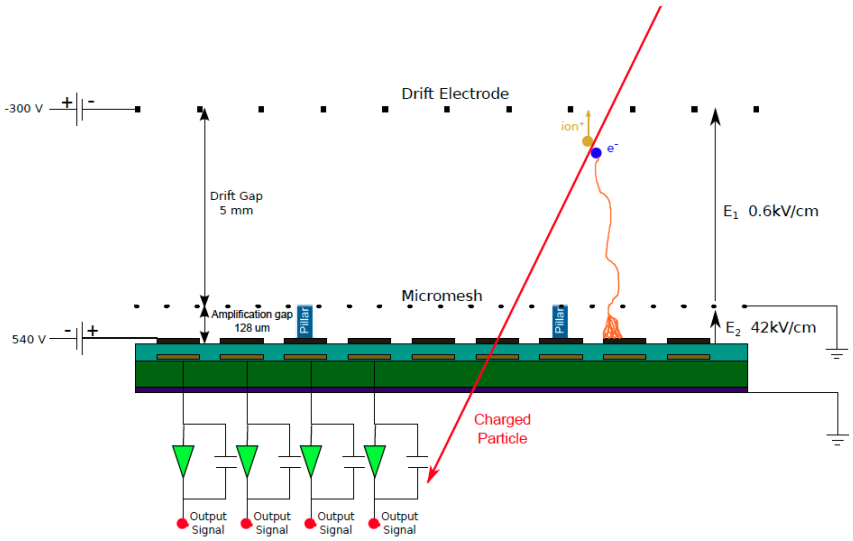

Figure 3.7: Resistive Micromegas schema and principle of working. With respect to a standard Micromegas an insulating layer is adopted between resistive and readout strip to prevent damages due to sparks

(Italy) for SM1, BMBF (Germany) for SM2, IRFU/CEA (Saclay) for LM1 and Dubna/Thessaloniki for LM2. The size of each quadruplet, depending on the type, ranges from 2 to 3 m^2. Each quadruplet is composed of 4 independent gas gaps and readout layers arranged in such a way to maximize the compactness and reduce the materials budget. The design foresees the construction of drift and readout panels separately: readout panels include resistive and copper strips, pillars are created on the resistive strips. Drift panels consist of the external frame, the drift gap and the mesh, which is then coupled to the pillars at the assembly phase. Figure 3.8 shows the quadruplet structure: readout panels have the same readout structure (resistive and readout strips and pillars) on both sides, separated by an honeycomb aluminium structure; drift panels are single side, if closing the quadruplet externally, or double sided, if used internally, between two readout panels.

In order to provide a measurement of both coordinates, a readout panel has strips inclined of ± 1.5 degrees with respect to the base of the trapezoid on both sides, and it is called stereo layer, while the eta layer has strips parallel to the base.

3.7.1 Readout panels

The external skins of the readout panels, including the readout structure, are the most critical element of the detector and condense most of the technological challenges of the entire project. The panel construction consists, at first, in the realization of the readout structure (PCB boards), described in great detail in Chapter 5, then glued on the two sides of honeycomb spacer at a later stage,

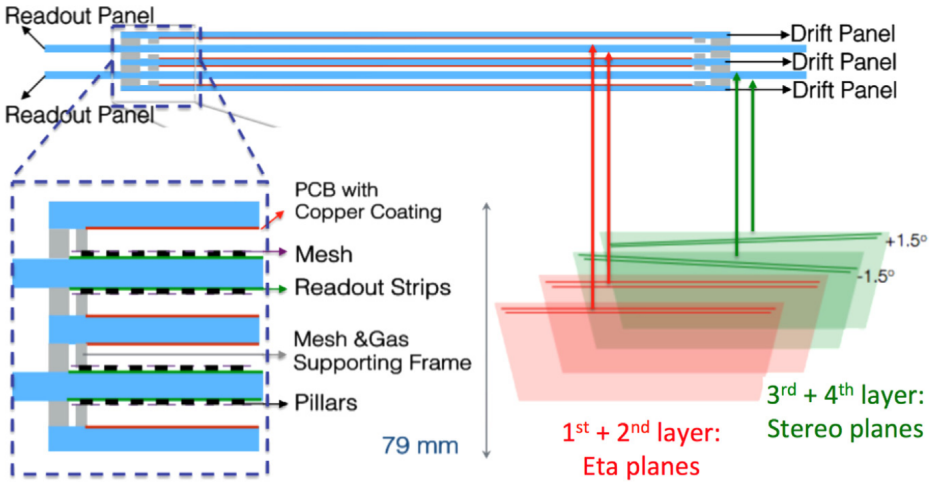

Figure 3.8: Structure of a NSW quadruplet. 2 double sided readout panels and 3 drift panels, one of those double sided are assembled, providing 4 independent detection layers . Different inclinations of the readout strips allow to reconstruct both coordinates.

providing stiffness, but containing the weight of the panel. Readout PCB boards are based on a glass-reinforced epoxy laminate material (FR4) PCB with copper strips chemically etched. An insulating layer of Kapton® is glued on top, covered, at its turn, by resistive strips. Rectangular pillars (1000x200 μm^2) are created via photolitographic technique on top of the resistive strips. Readout PCBs are produced in industries, ELTOS in Italy and ELVIA in France. Commercial standard PCB size are limited in size up to 60 cm in the short direction, obliging to segment a readout panel into 3 or 5 parts depending on the type. Figure 3.9 shows the segmentation of each of the four readout panel types (SM1, SM2, LM1, LM2) with indication of the dimensions. Each PCB has 1022 readout strips, 511 routed to the bottom left and 511 to the top right of the board as shown in Fig. 3.10. Here the electronic boards will be plugged. Resistive strips are interrupted in the middle of each board, defining two independent sectors where a different HV could be applied. Copper strips, on the other hand, are routed all along the board. The alignment between the readout PCBs on the two sides of the honeycomb is one of the most critical aspect of the readout panel construction. More details concerning the PCB boards will be given in a dedicated chapter of this thesis.

3.7.2 Drift panels

The drift board structure is simpler. Readout PCBs are replaced by FR4 skins (0.5 mm thick) covered by a Cu layer, serving as drift electrode. Gas gap frames and mesh frames are mounted on top, the first one defining the height of the drift gap. The mesh frame is 120 µm thinner, hosting the mesh, previously

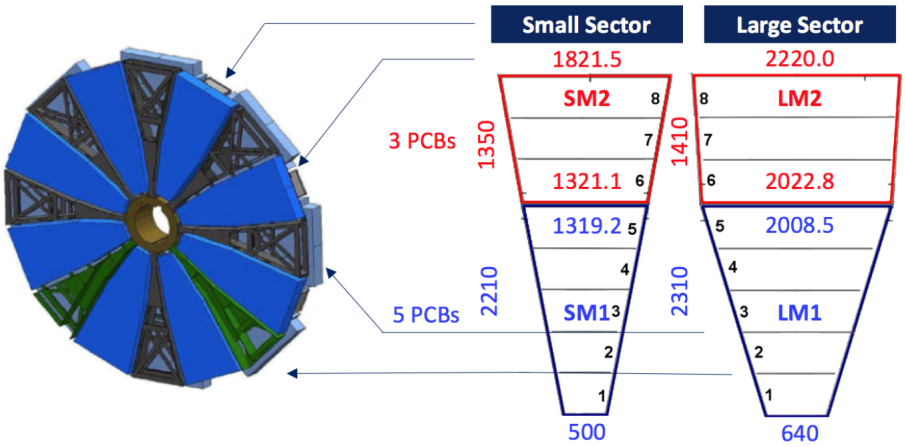

Figure 3.9: Segmentation of readout PCBs for small and large sectors into 3 or 5 RO PCBs has been required by the limited size of commercial PCBs available on the market. Indication of the dimensions are also given

Figure 3.10: Layout of a readout PCB, with indication of the location of the contacts for the front-end electronic boards

pre-stretched using pneumatic clamps at around 10 N/cm. Gas distribution pipes and inlets are also foreseen in the drift panel structure. Interconnection holes, connecting the two external drift panels, have been designed to limit the deformation of the quadruplet when gas overpressure is maintained in the quadruplet.

3.7.3 Module requirements

In order to fulfil the ATLAS requirements, extremely challenging mechanical constraints should be taken into account in the construction of the panels, in particular, considering the η direction:

- Position of strips on planes: 40 µm
- Relative alignment of the two sides of the readout panel: 60 µm
- Relative alignment of the two readout panels: 60 µm

Considering the z direction, performance requirements are translated into the following mechanical constraints:

- 37 µm in RMS, equivalent to $\pm$ 110µm mechanical tolerance, for both read-out and drift panels
- 50 µm for the aluminium bars and honeycomb structure

Chapter 4

Ageing of Micromegas detectors at GIF++ and rate studies

In this chapter a long term ageing study carried out on two Micromegas detectors at the CERN Gamma Irradiation Facility (GIF++) is reported. The aim is to prove that this detector design can stand the accumulated charge expected in 10 years of HL-LHC operations without any degradation of the performance, which has been estimated in 0.2 C/cm^2 including a safety factor. Complementary to this main study, the detectors performance has been studied in high particle rate environment, combining muon beam and high rate photon background. This project took almost three years to be accomplished, throughout which I have been always actively contributing and in some cases leading the activity, from the installation of the setup, to the analysis of the data. Relevant aspects of the physics of gaseous particle detectors can be found in the appendix, together with a brief description of the GIF++ facility.

4.1 The problem of ageing

An important effect which can affect the detector performance or the working point is the ageing, which may change due to the exposure to particle irradiation for long term periods. This has been found to be particularly relevant for wire-based detectors implying a progressive degradation of the performance [57]. Usually this degradation consists of an increasing dark current (background counting rate) after exposure to radiation or a decrease of the detector gain (leading to a drop in the efficiency) due to a partial shielding of the amplification field. The ageing is in general due to deposition of material on either the anode or the cathode surfaces. Deposits, especially on the anode, can take the form of whiskers, droplets or a uniform coating as shown in Fig. 4.1. Certain types of gas mixtures are more prone to produce deposits due to polymerization processes, for example those containing hydrocarbons. This leads to the formation of radicals, which are not volatile and tend to deposit on

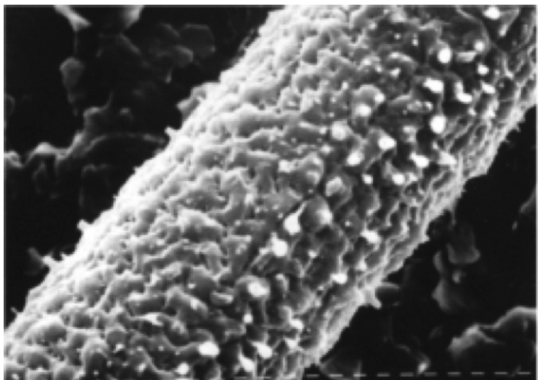

Figure 4.1: Example of wire analysed at the microscope revealing a coating surrounding the entire wire. Several types of coating can be seen on the wires depending on the composition of the gas mixture

the electrodes. In addition a relevant contribution is given by contaminants, such as non-polymerized monomers left from the production of plastic materials, traces of oils, lubricants and cooling fluids not properly removed after the detector construction. In general every detector technology has its own weakness, and the ageing manifests itself in a different way. Another crucial aspect of the ageing is that the effects depend on the rate of charge accumulation. Some problems may occur if the ageing is very slow, not appearing at all if the same charge is accumulated in a small amount of time. The best ageing test is thus to replicate the exact conditions the detectors will be exposed to in the experiment. Accelerating the ageing, for example exposing to an intense X-rays gun, or operating the detector in a completely different regime, may provide a partial and not reliable answer to the ageing issue. In the context of the NSW update project, Micromegas detectors will be installed in the ATLAS experiment during Phase-I upgrade, in 2019, and they are expected to run until the end of the operations, currently foreseen in 2035.

4.2 Description of the setup

The ageing study has been carried on two *bulk* resistive Micromegas detectors, with an active area of about 10×10 cm^2. The adjective *bulk* refers to the specific construction technique of this detector, where the mesh is embedded on the pillar structure. The rest of the detector design is very similar to the one adopted for the NSW project: 5 mm *drift* gap, ≈100 µm amplification gap, resistive structure based on 50 µm thick Kapton layer, and similar materials. The resistive strips are screen-printed and the paste used is exactly the same used for the NSW detectors. Each of the two detectors, called *T5* and *T8* in the following, has a single gas gap and mono-dimensional readout pattern, providing a single measurement of the tracks. The readout plane is composed of copper strips, 300 µm wide and with strip pitch of 400 µm. The resistivity of

the carbon strips above the insulating layer is of the order of few $M\Omega/cm^2$. The mesh has 18 µm thick wires, with an opening of 45 µm. As already explained, the best ageing test is the one lasting as long as the detector permanence in the experiment. For the NSW this means about 10 years. The position of the detectors in the GIF++ facility has been chosen to accumulate the already mentioned 0.2 C/cm^2 in about 2 years, based on a rough estimation of the particle rate, accelerating the ageing of a factor five, considered as a good compromise between duration of the test and its reliability. The position chosen in the facility is indicated in Fig. 4.2 (red dot), at about 90 centimetres of distance from the source. The distance of the aluminium stand from the source has been mechanically fixed and it did not change throughout the time. The two detectors were anchored to the aluminium stand rail; in this way the height from the floor was also fixed and optimized to face directly the source. On the other axis, however, detectors could slide on the rail with respect to the source position up to about 40 cm. This movement could affect the rate of photons illuminating the detectors, leading, ultimately, to a different ageing rate between the two chambers. A picture of the two chambers under test and of the aluminium stand is shown in Fig. 4.3. The extent of this effect has been studied by means of a dedicated Geant4 simulation, described in the following section. The HV (both for the amplification and drift fields) was completely controllable from remote: the HV cables, 20 meters long, have been routed under the false floor to the main rack area, where a CAEN mainframe was installed. Copper strips have been readout by means of the SRS system and APV 25 hybrids [58] [59]. A typical event as acquired by the APV is shown in Fig. 4.4. The acquisition window is usually set to 675 ns, divided into time bins of 25 ns each. At each time bin the integrated charge collected is readout. The electronics, FEC and ADC cards have been installed in the bunker, shielded from the radiation. Ethernet cables run from the bunker to the control room situated 50 meters apart. Ar/CO_2 (93:7) is the standard gas mixture used: the gas bottle is placed outside the facility, copper and stainless steel pipes have been routed to the detectors.

4.3 Characterization of the source

A preliminary characterization of the detector has been carried out by evaluating the number of single clusters of charge recorded by the electronics and belonging to the same photon converting in the gas. This study is required to estimate the particle background rate at which the detectors have been exposed to, as a function of the different source filters available. Figure 4.5 shows a typical event as seen from the Online DAQ software used. In the left panel the strip charge is reported as a function of the strip number. On the right the time of the signal arrival, corresponding to the time at which the maximum charge for each strip is measured, is reported as a function of the strip number. In this case three independent photons interacted in the gas in

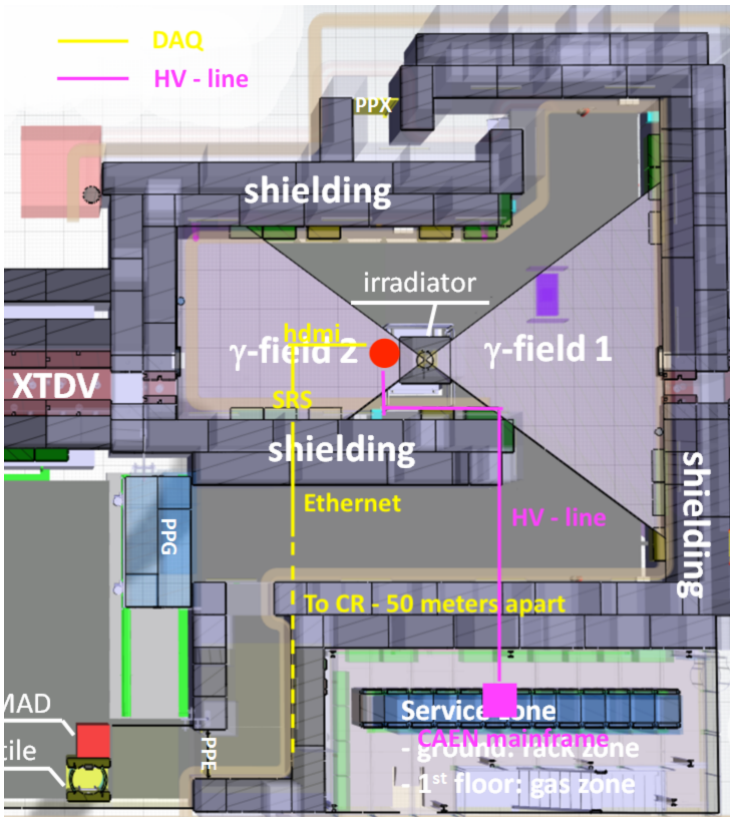

Figure 4.2: Layout of the facility. The position where the Micromegas setup was installed is also shown

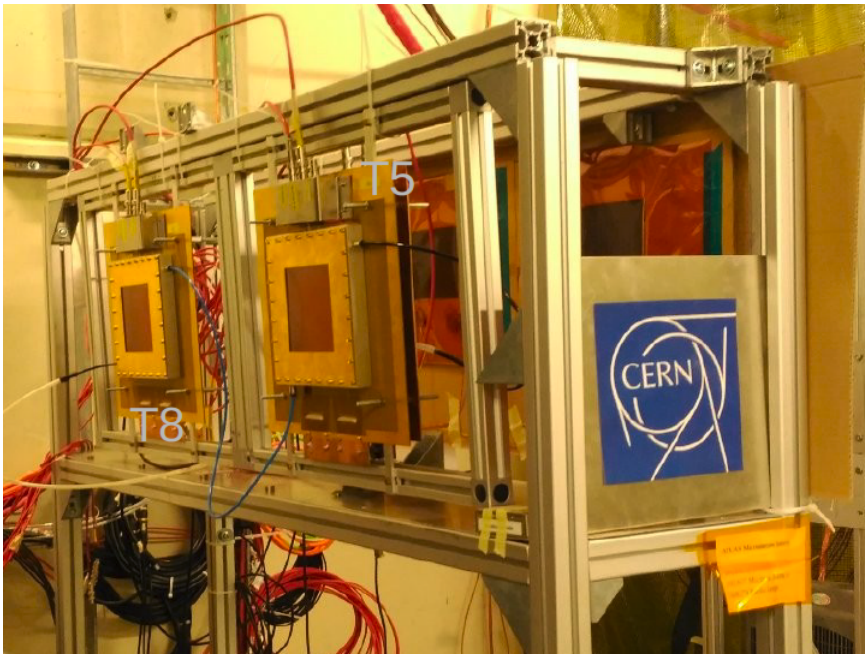

Figure 4.3: Aluminium stand supporting the two Micromegas detectors

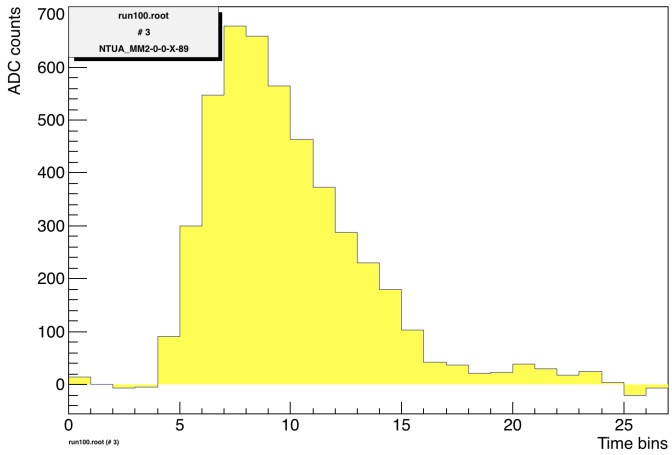

Figure 4.4: Event as acquired by the APV 25 electronics

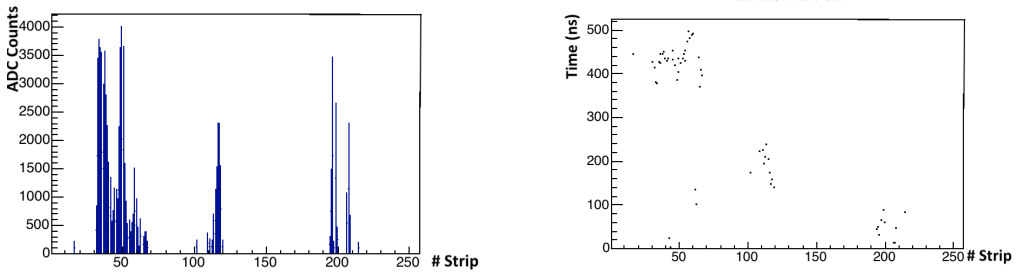

(a) (b)

Figure 4.5: Typical example of an event in a Micromegas detector as seen by the DAQ online system. Figure (a) shows the charge readout as a function of the strip number, figure (b) shows the time of arrival of the signal as a function of the strip number

the acquisition time window of $\approx$ 500 ns. The trigger was provided randomly. To evaluate automatically the number of interactions in a recorded event a topological reconstruction of the clusters is performed: neighbouring strips are grouped together, if temporally compatible, being most probably due to the same photon conversion. If one strip without a readable signal is surrounded by two fired strips, the central one is considered as dead and incorporated in the cluster. This reconstruction technique has been widely used in the Micromegas community, providing validated results in muons or pions testbeams or at the cosmic stand. At GIF++ an additional difficulty is represented by the electronic noise induced by the high level of radiation and from the fact that photons interacting in the gas can produce delta rays travelling long distances in the gas and producing, in turn, secondary ionisations. Concerning the first point, dedicated cleaning algorithms have been developed, more details can be found in [60].

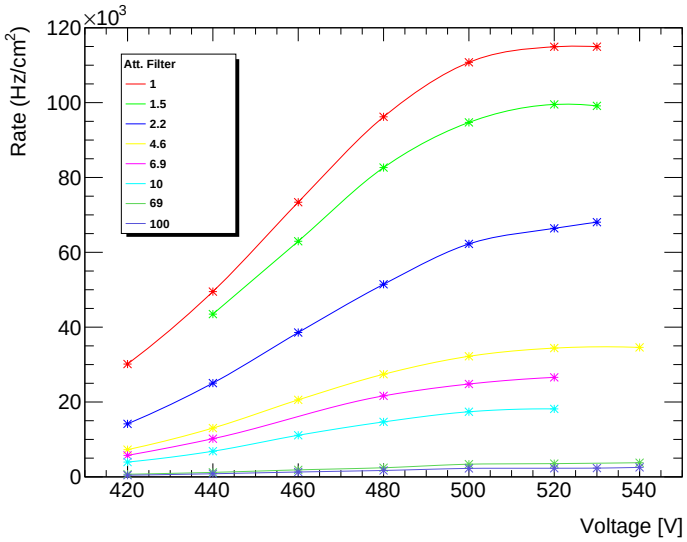

Figure 4.6: Photon interaction rate as a function of the amplification voltage for different values of the attenuation of the source

The particle rate has been estimated for different values of the source attenuation as a function of the amplification voltage normalizing the number of events recorded to the acquisition time window used. Results are shown in Fig. 4.6. Where not explicitly differently reported, the drift voltage has been kept always at 300 V, usual value for this type of detectors to guarantee a good transparency of the mesh to the electrons. With attenuation filter equals to 1, which means no attenuation of the source, a rate of about 120 kHz/cm^2 has been measured at 530 V. At lower amplification voltages, the amplification is lower, thus the efficiency may be also affected if the amplified charge is still below the threshold of the electronics. If this is the case, the particle rate measured decreases. With every combination of filters used a plateau in the number of counted clusters is reached starting from 500 V, defined as the voltage at which the full efficiency is reached.

The detector current as a function of the amplification voltage has been also evaluated for different values of the attenuation filters, and it is reported in Fig. 4.7. As standard working point for the ageing study an amplification voltage of 500 V has been chosen, corresponding to about 1.8 µA in the full source scenario. The corresponding efficiency is close to 1, as also previously observed.

4.4 Geant4 simulation of the detector at GIF

In order to achieve a comprehensive understanding of the detector performance, a dedicated Geant4 simulation has been carried out. Geant4 is a well known and widely used simulation tool-kit in High Energy Physics, allowing a detailed

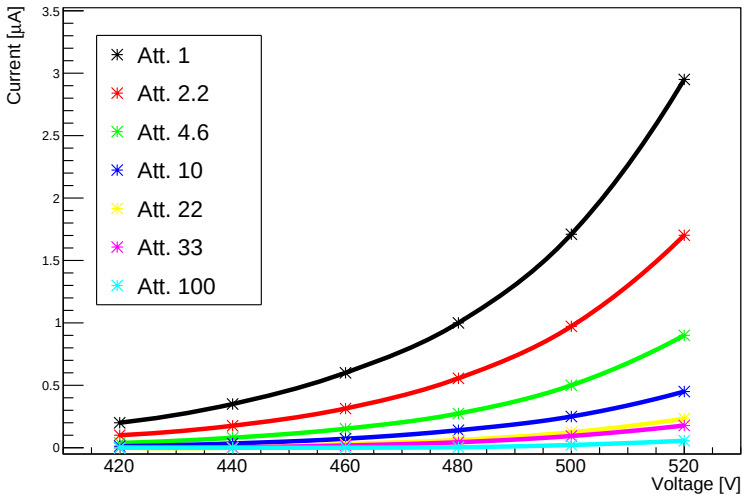

Figure 4.7: Detector current as a function of amplification voltage for various attenuation filters

and realistic description of the geometry, choice of the physics processes to activate, and freedom in the choice of the physics quantities to be scored [61]. In this case the realistic description of the facility has been imported directly as XML file, as described and validated in [62]. The source code of the facility geometry has been provided directly by the paper authors, to whom we are deeply grateful. The detector has been implemented as described in 4.2, defining a list of materials which are summarized in Fig. 4.8. The detector structure implementation is based on an already validated simulation work described in [63][1]. Concerning the physics processes activated, Geant4 provides predefined physics kits containing most of the relevant processes and covering most of the different applications. In this case the standard *FTP_BERT* physics list is used, containing all the electromagnetic processes, as described in [64]. The gas gaps, both drift and amplification are sensitive detectors: a particle interacting, or even only passing in a sensitive region is scored and the most relevant information (energy, energy deposited per step, momentum, direction) is saved for later analysis.

The first goal of the simulation was to evaluate the effect, in terms of observed particle rate, due to the sliding of the detectors in the aluminium stand from a position facing directly the source to a position misaligned of about 40 cm. This effect, if large, could lead to a difference between the two detectors in terms of ageing rate. The source, indeed, has been realized with a set of filters and lenses, designed to provide a flat irradiation front, in order to irradiate as uniformly as possible the detectors placed at the same distance from the source, as in our case. Several simulations have been carried

[1]Thanks to Nikolaos Karastathis for his courtesy.

Part	Material	Composition
PCB	G10	8.16%Na, 35.53%O, 2.29%Ca, 0.37%Al, 22.16%Si, 1.57%Mg, 13.66%C, 1.91%H, 13.45%Cl
Readout Strips	Cu	100%Cu
Insulators	Kapton	69.11%C, 2.64%H, 7.33%N, 20.92%O
Resistive Strips	C in Epoxy	52.02%C, 4.28%H, 13.59%O, 30.11%Cl
Glue	Epoxy	38.92%C, 5.45%H, 17.30%O, 38.33%Cl
Mesh, Drift	Stainless Steel	74.62%Fe, 16.90%Cr, 8.48%Ni
Frame	Aluminium	100%Al
Window	Mylar	62.50%C, 4.20%H, 33.30%O
Brass Cover	Brass	70%Cu, 30%Zn
Ar : CO_2 Gas	Ar : CO_2	93%Ar, 7%CO_2(~ 1, 91%C, 5.09%O)
Air	Air	0.01%C, 75.53%N, 23.18%O, 1.28%Ar

Figure 4.8: List of material defined for the geometry construction

out with a fixed number of particles isotropically emitted from the source recording only the ones passing trough the detector gas gaps. The position of the detector has been progressively moved with respect to the position facing directly the source, where maximum rate is expected, of 15, 30 and 45 cm on both sides. The relative number of particles scored, as a function of the position, normalized to the maximum is shown in Fig. 4.9 compared to the relative rate expected in absence of focusing lenses. Position at 0 cm is facing directly the source. A relative variation of $\pm 5\%$ is found by shifting the detector from the center to 40 cm on both sides and it represents the uncertainty to be taken into account in the particle rate estimation. The focusing effect of the lenses is of the order of few percent. The Geant4 simulation has been also used to evaluate the detector sensitivity, as described in the next section.

4.5 Estimation of the sensitivity

In order to provide an estimation of the sensitivity, which is the probability of a photon to interact and to be seen by the detector, in addition to the rate recorded, the total photon rate illuminating the detector needs to be estimated. The Geant4 simulation has been therefore run several times, once for each setting of the attenuation filters used, with the detector placed as in the real facility, counting the particles passing through the gas gaps, without requirements on the interaction in the detector. The number of events seen and counted experimentally at the efficiency plateau (amplification voltage set to 500 V) by the detector has been then compared with the flux simulated, as reported in Tab. 4.1. The last column reports the value of the sensitivity, calculated as the ratio between the two values. The sensitivity shows a value of

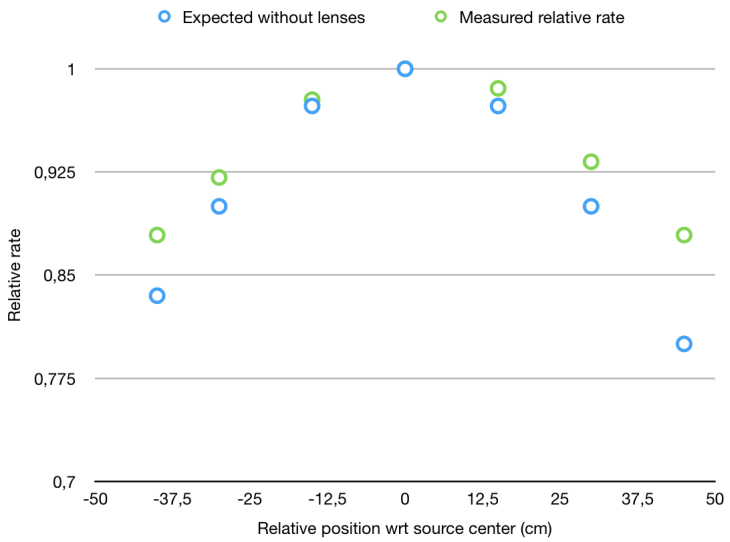

Figure 4.9: Detectors could be displaced with respect to the center of the source up to 30-40 cm. A simulation has been carried out to evaluate the maximum difference in photon flux due to a misalignment of the detectors with respect to the source. A min-max difference of about 10% is found

about $1.7 \cdot 10^{-3}$ compatible among the different attenuation filters considered except for the case where the source is not shielded (attenuation 1). In this case a lower value is found. A explanation could, however, justify this behaviour: at very high rate the current flowing in the detector is very high (order of µA) inducing a voltage drop on the same resistive strips (whose resistivity is of the order of few $M\Omega/cm^2$) resulting in a reduction of the effective field in the detector, i.e. a lower amplification. A lower number of clusters seen would lead to a lower value of the sensitivity.

Table 4.1: Rate measured by the detector, simulated and their ratio as a function of different attenuation filters

Att. factor	Rate from detector (kHz/cm^2)	Total photon rate	**Sensitivity**
1	115	7.70E+07	0.0015
1.5	100	5.21E+07	0.0019
2.2	68	3.73E+07	0.0018
4.6	35	1.88E+07	0.0018
10	18	1.06E+07	0.0017
100	2.5	1.49E+06	0.0017

To verify these explanations a ratio plots have been computed considering the measured particle rate as a function of the amplification voltage for various attenuation filters, divided by the rate observed at the respective HVs, but always taken at a reference attenuation filter. The reference filter has to have

a high value (low particle rate from the source), where effects arising from high occupancy are not present. A second ratio plot, made as the previous one, but considering the detector current instead of the particle rate has been also considered. Both ratio plots should show a flat behaviour as a function of the amplification if no supplementary effects arise, meaning that the relative ratio between the rate (or the current in the second case) measured with different filters depends only on the value of the filters themselves and not on the voltage. If voltage drop is taking place, meaning a reduction of the amplification at high rate, both the ratios should decrease while increasing the amplification voltage. Fig. 4.10 shows the two ratio plots when the attenuation 100 (the peak source intensity is reduced by a factor 100) is used as a reference. The top one (a) is done by considering the measured rate, the bottom one the current recorded (b). Both plots show a reduction of $10\% - 20\%$ at high rate with the increasing of the amplification voltage, confirming that the amplification is indeed affected by the high particle rate environment. A contribution arising from the failure of the clusterisation algorithm in correctly recognizing the cluster is also visible at the highest rate, even at low amplification voltage.

4.6 Experimental evaluation of detector performance at high rate

The possibility of combining a muon beam with the photon source irradiation, gave the chance to assess the detector performance, spatial resolution and amplification, as a function of the source intensity. The resolution of a Micromegas detector is related to the precision on the cluster position definition, which is in general higher if the cluster charge of the event if bigger. The reason is the fact that sharing the charge among many strips, allows a better definition of the centre of charge cluster position, in the case of muons impacting perpendicularly the detector. Amplification reduction, due to voltage drop or any other effects, would produce a decrease of the average size of the clusters, reducing, ultimately, the detector performance. The two detectors, aligned to the beam, have been installed in a telescope as shown in Fig. 4.11. Two Micromegas 10x10 cm detectors, called *Tmm* have been used as tracking reference chambers. The trigger signal, fired by the passage of muons, has been provided by the coincidence of scintillators placed both outside and inside the facility to reduce the fake triggers coming from the photon interactions.

Recorded data contains both muon tracks and randomly distributed photon interactions. After the topological cluster reconstruction already described in Sec.4.3, a dedicated algorithm, based on Hough transform [65], has been developed to discriminate between the two. First a calibration file is provided, containing data taken without photon irradiation (source off). This calibration is required to perform the alignment of the detectors and the correction for inclination. Then data with both muons and photons is analysed. Each cluster,

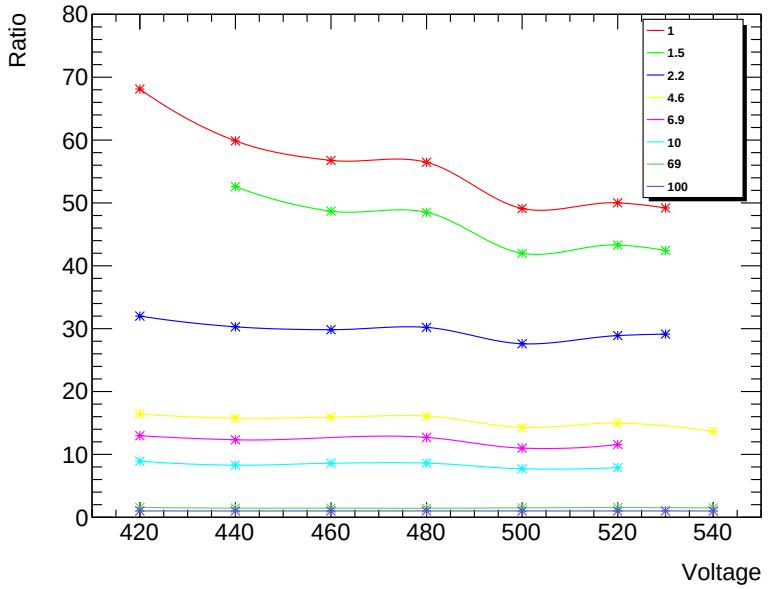

(a)

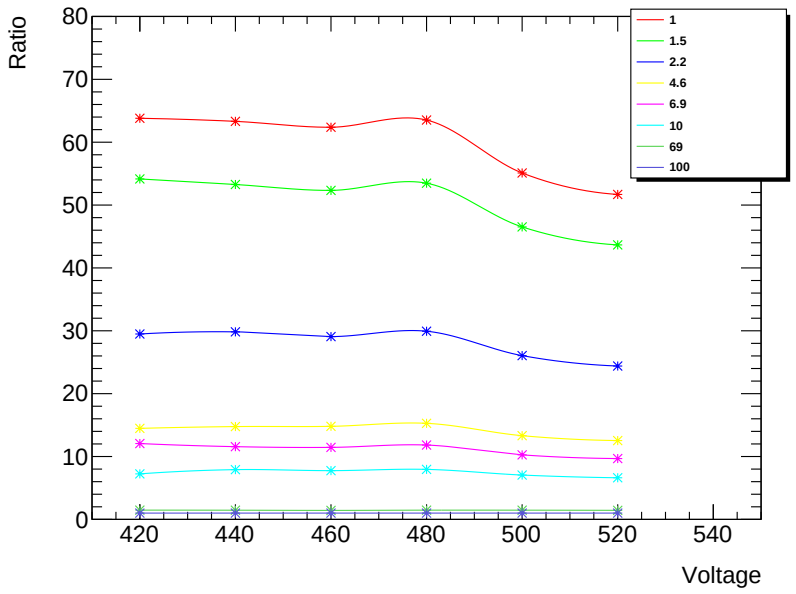

(b)

Figure 4.10: Figure (a): particle rate as a function of the amplification voltage for different attenuation factors divided by the rate measured at the same value of voltage but at attenuation 100. Figure (b) shows the same ratio plot but considering the detector current in place of the particle rate

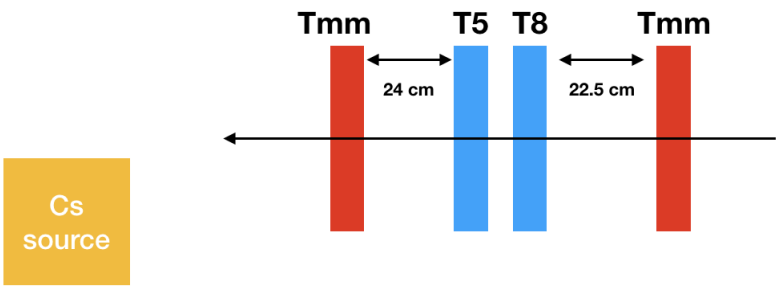

Figure 4.11: Setup for the high rate detector performance study. Two bulk Micromegas are used as tracking chambers

given its position, is transformed into a line (or, more in general, a curve) in the Hough space. In this case a simple linear transformation is used. Clusters compatible with a muon track all intersect in the Hough space in one point as shown in the last section of the figure. The coordinate of the intersection point, when anti-transformed, provides the parameters of the track. This technique has been found extremely efficient in muon track selection.

The distribution of the residuals, obtained computing the difference between the measured cluster position and the best-fit track interpolated on the detectors under test is then fitted with a gaussian distribution, whose sigma parameter provides the resolution. In order to estimate the amplification factor, the cluster charge distribution of muon candidates as recognized by the Hough transform algorithm is fitted with a Landau function and the most-probable-value is then considered as shown in Fig 4.12. This parameter quantifies the mean value of the charge collected for muon signals; if the value decreases, clusters have in average less charge, meaning a reduction of the amplification. For all these runs, amplification voltage has been set to 500 V, while the drift voltage, as usually, to 300 V.

The particle rate has been modified changing the filters. The rate equivalent to a specific attenuation has been estimated through the measurements already described in a previous section. Detector performance has been assessed up to a particle rate of about 70 kHz/cm^2. It is important to remind that this type of detector has been designed to work in particle rate environment up to 15 kHz/cm^2 as expected in the ATLAS New Small Wheels. Figure 4.13 shows the results for the resolution (a), and the amplification (b) as a function of the particle rate. A resolution of about 70 µm is found constant even at the highest rate. This value is slightly worse than the intrinsic resolution of the detectors found in previous studies, due to a not fully optimized analysis. However the purpose of this study is only to evaluate the degradation of the performance, if any, as a function of the rate. For what concerns the amplification, a most-probable-value of about 1300 ADC counts ($\approx 10^4$ electrons) have been found, constant up to 35 kHz/cm^2, with a small degradation only at the highest rate.

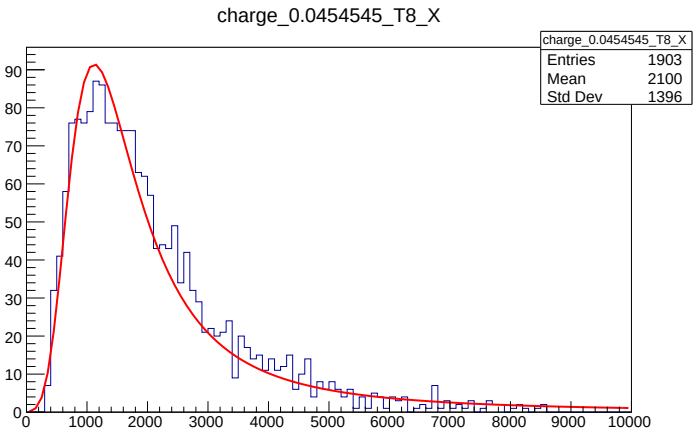

Figure 4.12: Typical distribution of muon cluster charge. The fit is performed with a Landau function. The most-probable-value is an indication of the amplification in the detector

The errors bars reported are obtained by the error on the parameter estimation. This study successfully confirms that no performance degradation will arise if detectors are operated at the maximum rate of 15 kHz/cm^2, and even at higher rate.

4.7 Long term ageing study

In addition to the rate capability, the assessment of the ageing effect on these detectors is a crucial aspect in view of their installation in complex and long term experiment as ATLAS or CMS. In our cases T5 and T8 have been installed in GIF++ to perform an accelerated ageing in May 2015. Since then the detectors currents, HVs, environmental conditions have been kept constantly monitored. Figure 4.14 shows for both the detectors the integrated charge as a function of time until the end of the measurement, in December 2017. More than 0.3 C/cm^2 have been collected by both the two detectors, which is about 0.1 C/cm^2 more than the initial goal. It is evident that the charge accumulation rate, or slope of the curves, is not constant. This is due to the frequent changes in the position of the detectors, leading to a change in the current as evaluated by means of the Geant4 simulation and described in a previous section, or changes in the source attenuation, or testbeam carried out in the facility as in May 2017. The effect of the irradiation has been assessed by measuring the efficiency to muons and the gas gain as a function of the amplification voltage three times, once before the beginning of the irradiation, one in the middle after accumulation 0.2 C/cm^2 and one at the very end of the irradiation period. Figure 4.15 shows the efficiency curves for the three data measurement campaigns for the two chambers, T5 and T8 respectively. The efficiency measurement has been carried out installing the two detectors in the

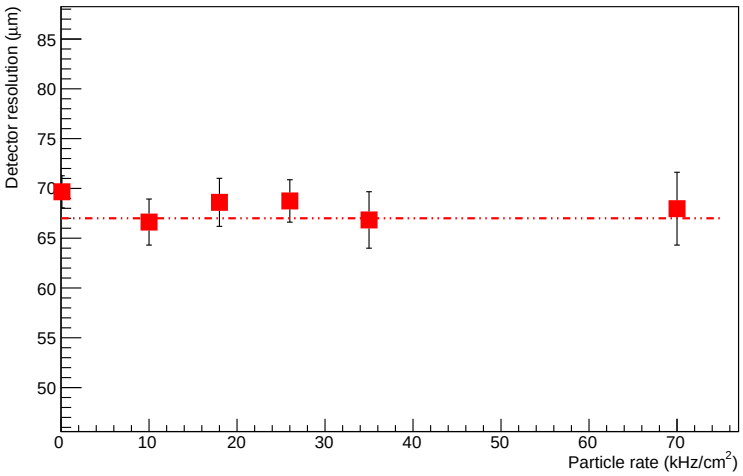

(a)

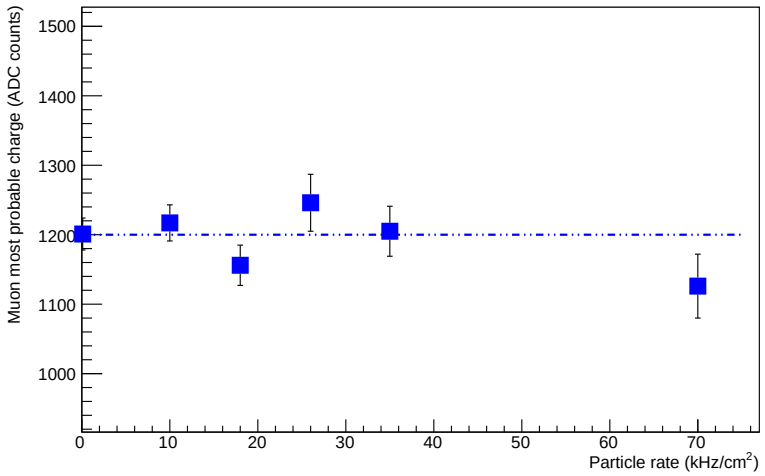

(b)

Figure 4.13: Resolution (a) and most-probable-value (b) of muon charge as a function of the particle rate

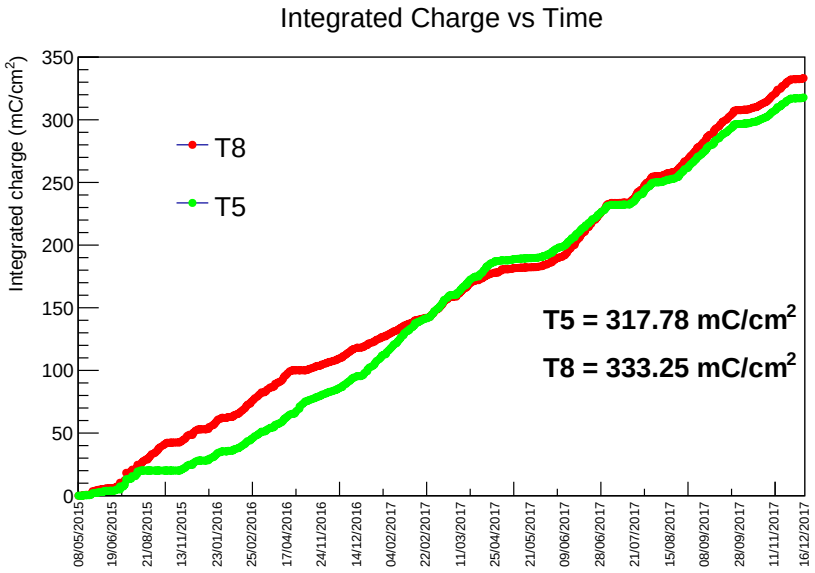

Figure 4.14: Integrated charge as a function of time

same telescope already described for the high rate studies and exposing them to the muon beam. Data have been taken with source off as described above. Scintillators were employed to provide the trigger signal. An event has been considered if one and only one cluster is found on each tracking detector and considered efficient if, within a window of 500 µm from the expected position, a cluster is found also on the detector under test. Viceversa if no clusters are found the event is labelled as lost, and contributes to the inefficiency evaluation. Two main aspects are relevant and should be considered in the evaluation of the ageing in this measurement. The first is the value of the efficiency at the plateau, initially very close to one, that could degrade reducing the maximum achievable tracking efficiency. The second one is a shift of the working point, defined as the voltage which needs to be applied in order to be fully efficient. An increase of the working point would require an increase of the voltage at which the detectors should be operated, potentially leading to instabilities and discharges. As clearly shown in the plot, none of these two issues took place in the detectors. The environmental conditions are not taken into account in this analysis, explaining the small differences at lower voltage. This kind of analysis is also sensitive to the electronics noise and pedestal fluctuations: different setups, especially at very low amplification, where the charge of muons cluster is low, could show small differences. In any cases an efficiency of almost one is reached, at a working point of about 500 V.

To confirm this result the gas gain has been measured in the laboratory with an ^{55}Fe source. Figure 4.16(a) shows the setup that has been used for the measurement: HV has been applied to resistive strips and drift electrode, as in normal detector operation. The mesh has been connected to a discriminator and then to a scaler to provide the rate of photon interactions once the source

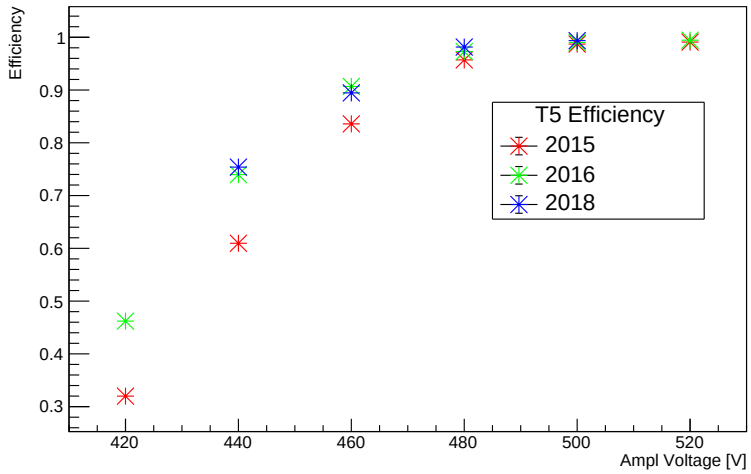

(a)

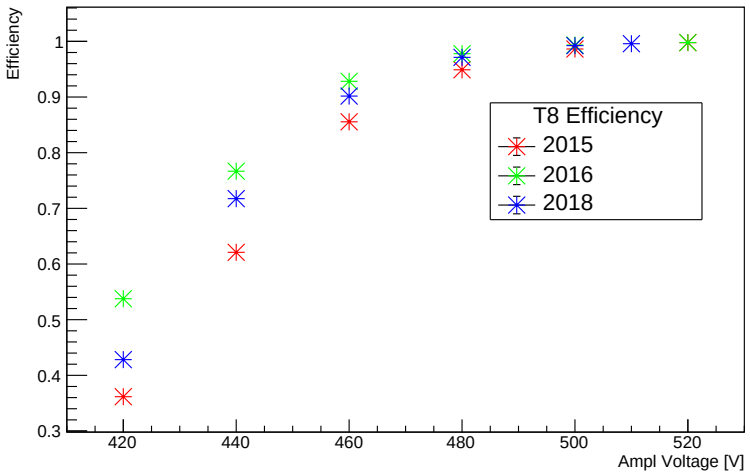

(b)

Figure 4.15: Efficiency curve as a function of the amplification voltage for T5 (a) and T8 (b) for the three data taking campaigns

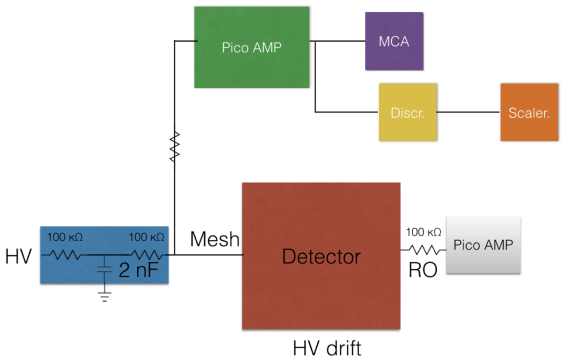

Figure 4.16: Schematic of the setup used for the gas gain measurement

is placed on the detector. The gas gain has then been calculated observing the current on the resistive strips as follows:

$$G = \frac{I}{Rep} \tag{4.1}$$

where R is the particle rate observed at full efficiency on the mesh, e is the electron charge and p is the number of primaries expected for each photon interaction. A reference value, usually adopted in literature is 220.

Fig. 4.17 shows the gas gain in logarithmic scale for T5 (a) and T8 (b) as a function of the amplification voltage for the three measurement campaigns. Also in this case no corrections for environmental conditions have been applied, but no significant reduction of the gain has been observed.

The last approach to assess whether performance has changed throughout the time is to look at the current flowing in the detector as a function of time during the source-on periods. This approach has a critical aspect: due to the several changes in the attenuation filters in the 2 years and a half of irradiation, and especially to the movement of the detectors in the structure (see previous sections) which were not registered, the rate of photons reaching the detector hasn't been always constant. To account for this issue time intervals where source conditions and detectors parameters are fixed have been considered; if the source attenuation, at a certain instant, is changed, the time interval is closed and a new one is started with the new source parameter. This technique allows to identify single time units where nothing was changed in the facility. Then periods are joint together with a method that could be called *tail tip*: the current is rescaled in such a way that the very first part of a period takes the same value of the last part of the previous one. In this way the absolute value of the current is lost, but trend in the current behaviour can still be appreciated, if any. No ageing is expected between adjacent periods. Another important aspect has to be taken into account, which is the charge-up and polarization effects taking place as soon as the source is switched on at very high rate. In this condition for few minutes the dielectric polarization induces an increase

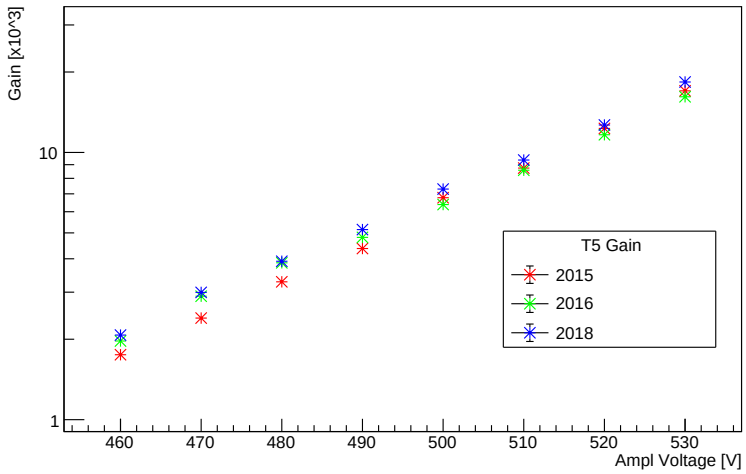

(a)

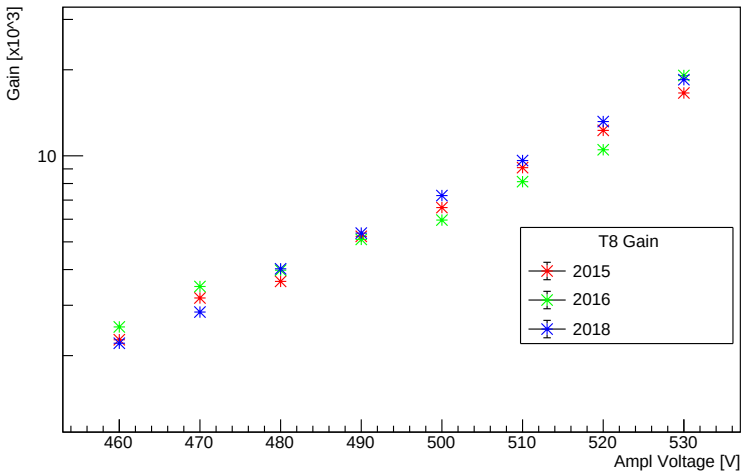

(b)

Figure 4.17: Gas gain for T5 (a) and T8 (b) as a function of the amplification voltage for the three measurements compared

of the current which is not due to any ageing effect. In the analysis, therefore, about an hour of the first part of each time interval is cut away in order to consider current values only in stable conditions. In Figure 4.18 the detector current is reported as a function of time when the source is switched off and then immediately switched on again to full rate (a) and when it is switched on after some time being fully shielded (b). As soon as the source goes to off, the current drops to zero, showing a negligible dark current. When the source is switched on, a peak is observed in both the situations, then exponentially decreasing in the order of few seconds. In the second case, however, a very small, but still perceptible increase of the current is observed, which saturates after some tens of minutes. Both the effects are very small (order of few %), but should be taken into account to provide a reliable description of the current behaviour as a function of time. Figure 4.19 shows the current behaviour for the two chambers, T5 snd T8. On the X-axis the interval number is reported. The average length of a period is about 3 days. The integrated charge considered in the analysis, reported in the plot as well, is smaller than the total integrated charge due to analysis requirements, most of them already described above. In any case, both detector current trends are clearly demonstrating that no appreciable changes have taken place, confirming the results already suggested by the gas gain and the efficiency measurement.

4.8 Conclusions

The presented studies carried out on Micromegas prototypes at the GIF++ facility were aiming to assess the performance of the detectors in high particle rate environment and the ageing effects due to long term irradiation. Resolution and amplification are not affected up to 70 KHz/cm^2, and no sign of ageing has been observed after integrating 0.3 C/cm^2, much higher than what this type of detectors will see in 10 years of High Luminosity LHC operations. A similar ageing study has been also carried out at Saclay laboratories in the past years with an X-ray generator, reporting no significant sign of performance degradation [55]. In this case, however, the ageing rate was accelerated of several orders of magnitude, performing all the test in about one week. As observed in a previous section, this approach may provide not fully reliable results.

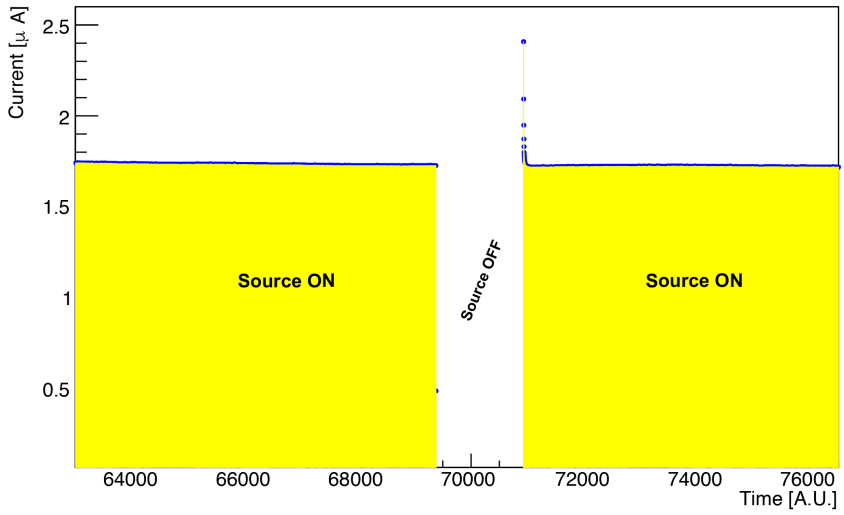

(a)

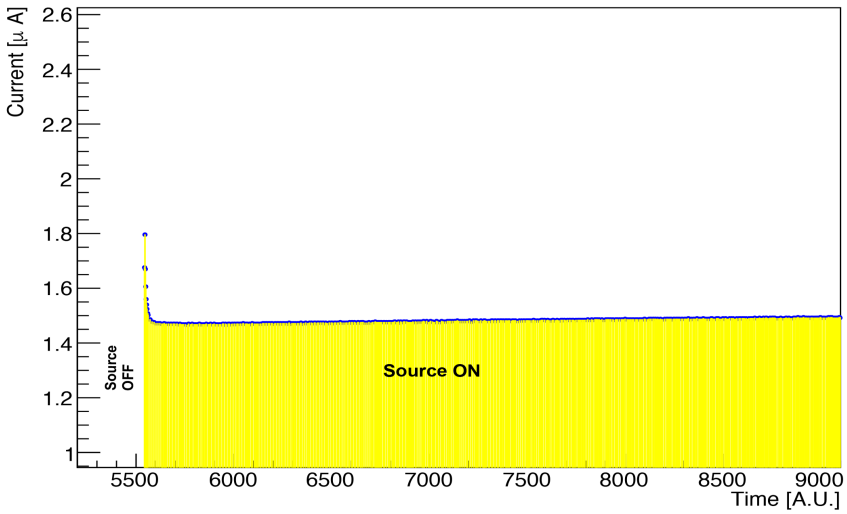

(b)

Figure 4.18: Detector current as a function of time when a transition from source on to source off and immediately back to source on is performed (a) and when source is turned on after some time (b)

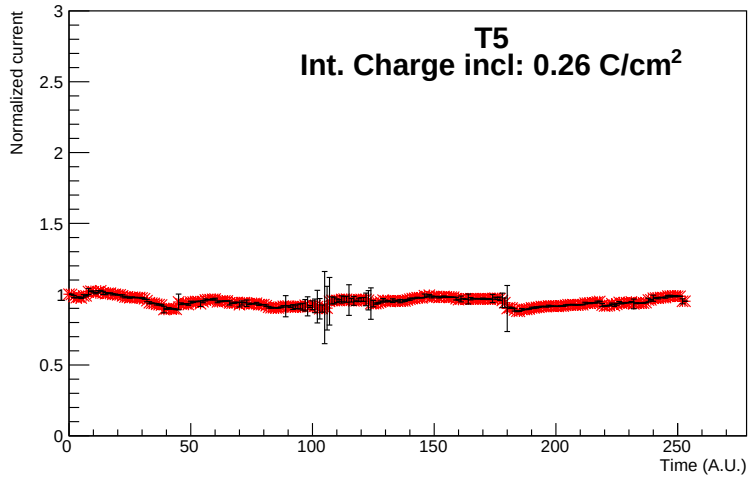

(a)

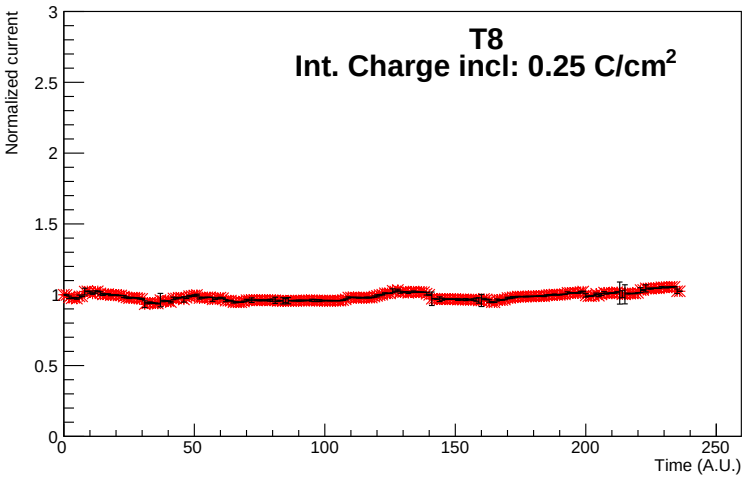

(b)

Figure 4.19: Current trend for T5 (a) and T8 (b) as a function of time

Chapter 5

Quality Assurance of RO Printed Circuit Boards (PCBs) for the NSW detectors

In this chapter a detailed description of the readout Printed Circuit Boards (PCBs) for the NSW detectors is given, in particular focusing on some aspects of the quality assurance and control performed at CERN. In this project I have been contributing in several ways: I have been the responsible for the development and maintenance of the databases and software infrastructure, collaborating in the definition of tests, in the daily shifts as expert and in the supervision and training of shifters for more than one year and a half. The material here presented is the result of many years of work, headaches and sleepless nights of several friends and colleagues of the CERN EP-ADE-MU group. I am deeply grateful to all of them.

5.1 Readout PCB design and construction

As seen in chapter 3, each readout panel is composed of two readout skins, one for side. Each skin is, at its turn, composed of 3 or 5 independent readout PCBs, depending on the quadruplet type. In total about 2200 readout PCBs will need to be delivered to the construction sites in order to build all the detectors. The structure of a readout PCB and the construction sequence are shown in Fig. 5.1. A 500 µm a glass fiber epoxy layer (called FR4) is used as substrate for the copper readout strips, obtained by etching, having a pitch ranging from 425 µm to 450 µm and a thickness of 50 µm. A 50 µm Kapton® foil, carrying the resistive strips, is then glued at high temperature and pressure in a very clean environment on the FR4 layer. The resistive strips have the same pitch of the readout strip, and a thickness of about 20 µm. HV input lines are connected to the resistive strips, screen-printed with silver conductive paste. Finally the pillars are created via a photolitographic process after lam-

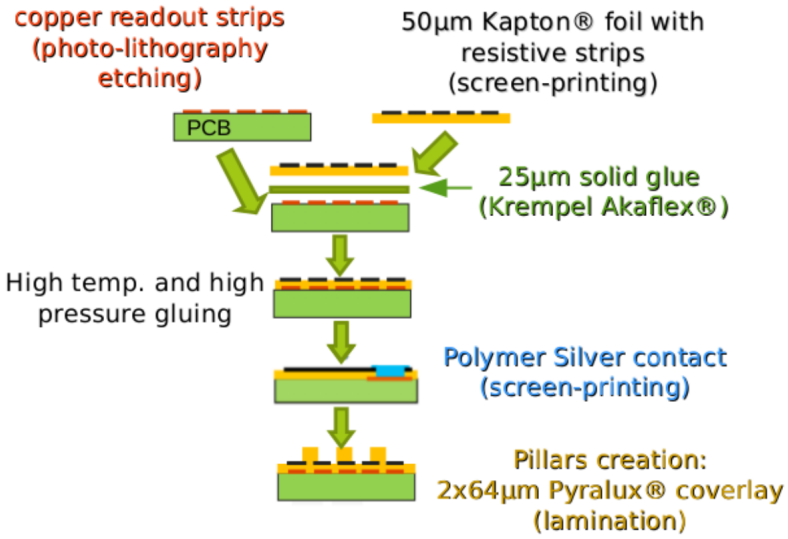

Figure 5.1: Step of PCB production

inating the PCB with a double layer of coverlay material (Piralux PC1025). Finally edge milling and precision holes drilling is performed. During the copper etching, several alignment masks are also created to verify a posteriori the precision of the construction.

5.2 Quality control (QAQC) organization at ATLAS PCB lab

The readout PCBs are the most challenging and complex part of the entire NSW detectors. They are produced by ELTOS (Italy) and ELVIA (France) companies, involving non standard processes and extremely high precision, requiring dedicated machines, training and specific follow-up. The quality control and assurance operated at CERN is a crucial element of the entire project: an out-of-specification or malfunctioning board sent to the construction sites would result in a not perfectly working detector. The schema of the readout PCBs logistic and production is show in 5.2. Base materials (top left of the image) are sent to CERN from external suppliers and then sent to the companies for the PCBs production. Resistive foils (bottom left of the image) are produced in Japan (Kobe), then shipped to CERN and finally to the companies. After construction, PCBs are sent to CERN for quality assessment: if minor or no defects are found PCBs are shipped to the four construction sites (Pavia, Munich, Saclay and Dubna). In case of major defects boards are repaired at CERN, if possible, or sent back to companies for replacement or reparation as shown in Fig. 5.3. The tests performed at CERN aim to complement the quality protocol established with the companies, monitoring all the production steps.

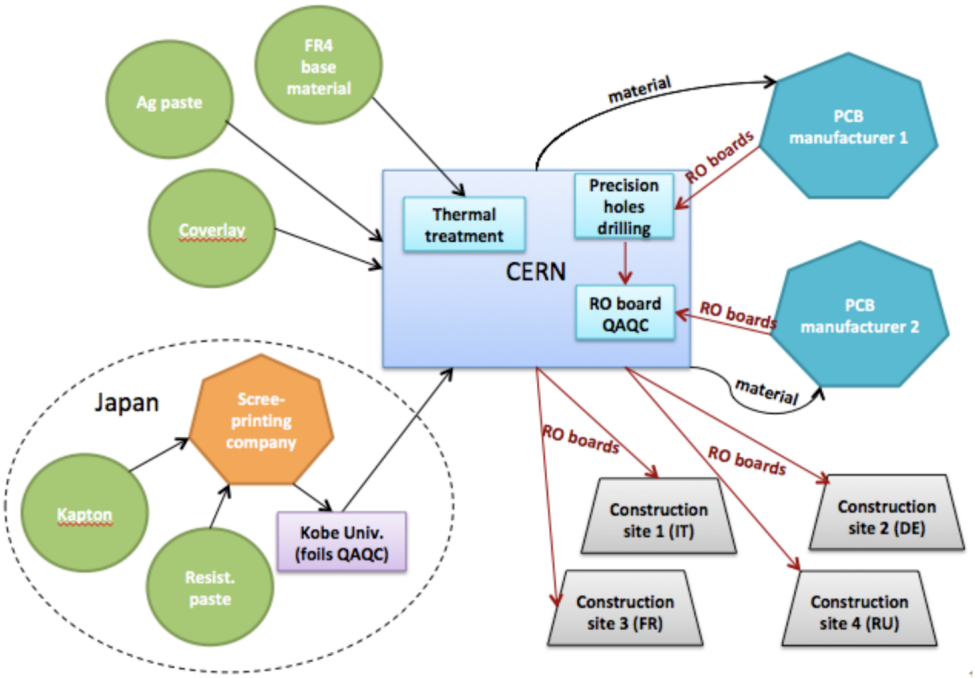

Figure 5.2: Schema of PCB and base material logistic

Figure 5.3: Schema of QAQC tests and organization

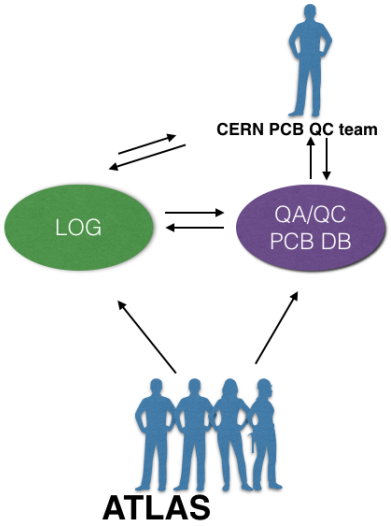

Figure 5.4: Dedicated databases have been set to record logistic and QAQC information, the LOG and PCB QAQC databases respectively. Both are hosted at CERN and based on Oracle

Given the large number of boards and the complexity of the logistic, each PCB and resistive foil is associated with specific and unique IDs. This ID allows the registration of all the information related to the single item and to keep track of the shipments. Moreover, a dedicated database has been developed to host the QAQC measurements and tests results, in order to be accessed and retrieved them when needed. Figure 5.4 shows part of the databases interplay: the QAQC PCB database is accessed in reading and writing mode by the ATLAS CERN Muon group, responsible for the quality assessment of the boards. Each board is also registered in the *LOG* database, where shipment, parenting and logistic is recorded. The external community, indicated in the picture as *ATLAS*, can at any time retrieve the information from both the databases, through dedicated web interfaces described later in the text.

The control process of each single board arriving to CERN is organized in multiple stations, or desks, designed and equipped with proper tools and instruments for each specific test as shown in Fig. 5.3. Before starting the real tests, each board passes through a quick, but detailed visual inspection by an expert, in order to spot macroscopic problems that could affect the whole batch: manufacturing of PCB boards is a complex procedure, involving several chemical baths and steps. It turned out that changes in the industrial processes, could dramatically affect the whole production. A immediate feedback to the companies after the arrival of a new delivery is therefore of extreme importance. After this, the QC starts and PCB are registered in the *LOG* database. Each desk is also equipped with a computer, to access the web form developed to fill all the information and save permanently in the database. The online form, developed in Javascript and AngularJs, hosted at

CERN and based on Nodejs, is organized in indipendent sections, mimicking the organization of the QC lab. Each section allows the user to provide the relevant information, insert measurements, answer specific questions. Thresholds and possible source of issues are automatically advertised on the form. When check of the board is completed, i.e. all the sections have been filled, a final grade to the board is suggested depending on the results of the intermediate sections: an expert user, when performing the final inspection and reviewing the whole board, can confirm or modify the automatic grade, accepting the board, or rejecting it. A view of the form is provided in Fig. 5.5.

5.3 QAQC tests

In the following sections few details of the most relevant tests performed will be given, focusing in particular on the critical defects found throughout the project.

5.3.1 Toplight inspection

The toplight inspection consists in the visual inspection of the board surface. The desk is equipped with a stereo Leica microscope and a light to investigate all the possible defects that could cause HV instabilities. It should be reminded that on top of the pillars, during the quadruplet assembly, the metallic mesh will be coupled defining the amplification region. Distance from the mesh and resistive strip is of about 120 µm, being the height of the pillars themselves. The presence of a defect, contamination, dust trapped below the Kapton® could sensibly reduce this gap, leading to a local higher gain region, and introducing a weakness in the whole detector as shown in Fig. 5.6. The internal tolerance for bumps has been set to 10 µm. Larger bump needs polishing with sandpaper, if possible, or passivation with a coverlay disk. Other issue that should be found at toplight inspection are shown in Fig. 5.7. Edge damages, or any damage of the resistive foil affecting the Kapton® will break the insulation between resistive and readout strips, leading to discharges and making the detector completely unusable. If the isolation is broken, no reparation can be performed and the PCB is rejected. The insulation between resistive and readout strip is also tested with a dedicated template and a Megger insulation tester, by applying 1 kV: if more than 3 GΩ are obtained, test is passed. Another HV critical insulation test is performed between the resistive strips, and the part of the PCB in contact with the external frame. This part is covered by 128 µm of coverlay material and also in this case a failure of the insulation could cause the immediate rejection of the board. Resistance value of the coverlay insulation higher than 30 GΩ is expected.

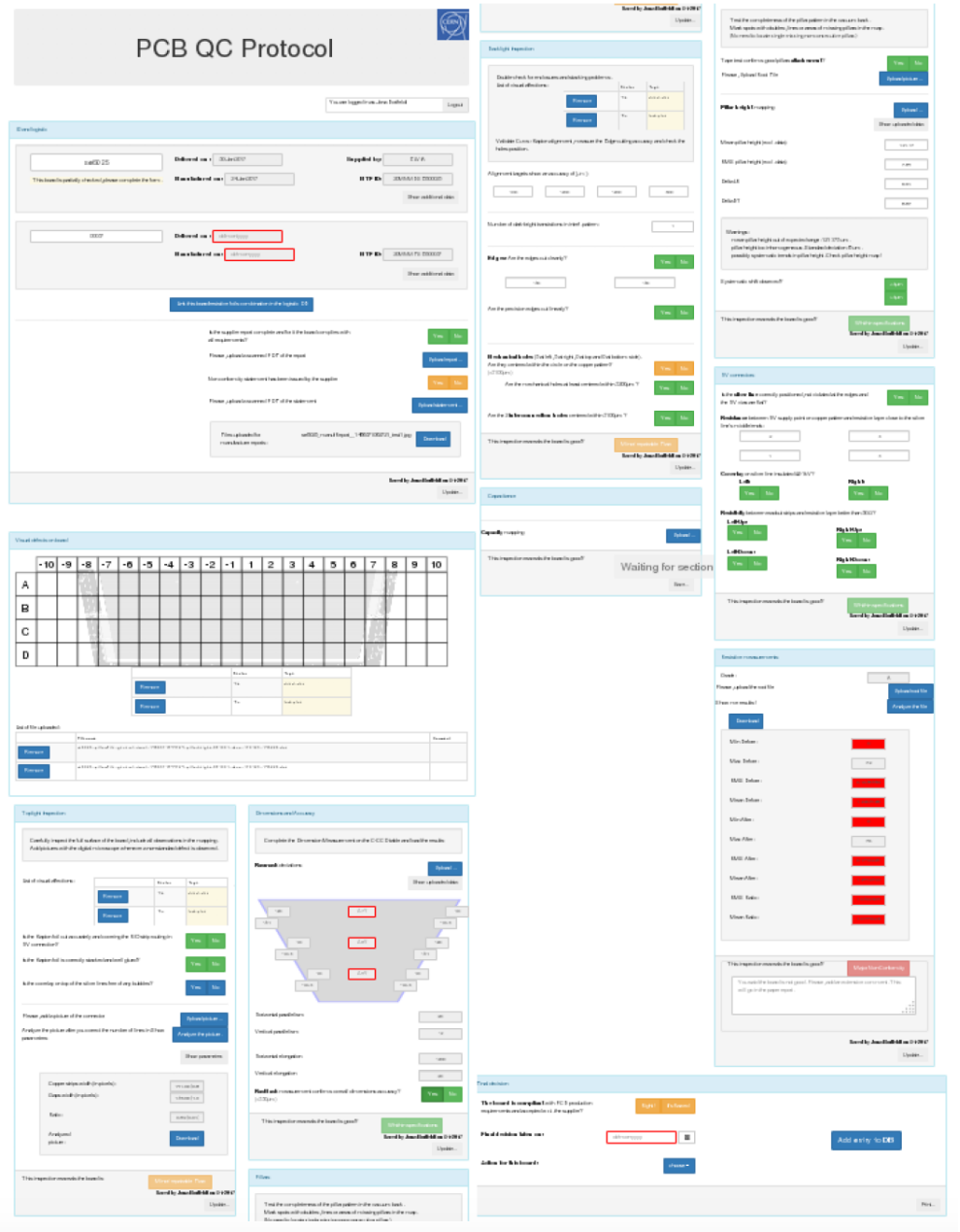

Figure 5.5: An online web form has been developed to retrieve and insert PCB information. In the image a *collage* of the different sections is shown

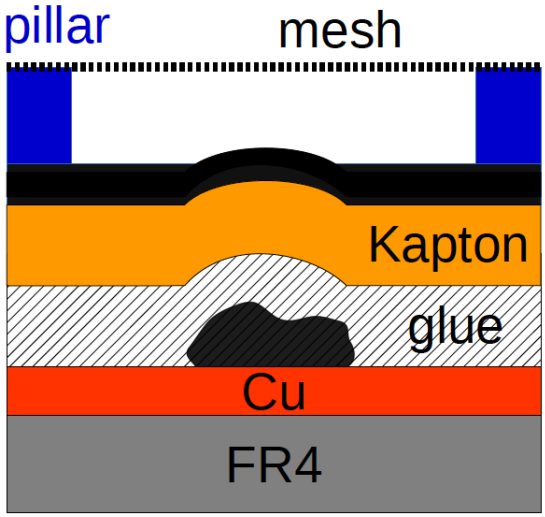

Figure 5.6: Any material trapped below the Kapton® introduces a weakness in the detector, reducing the amplification gap

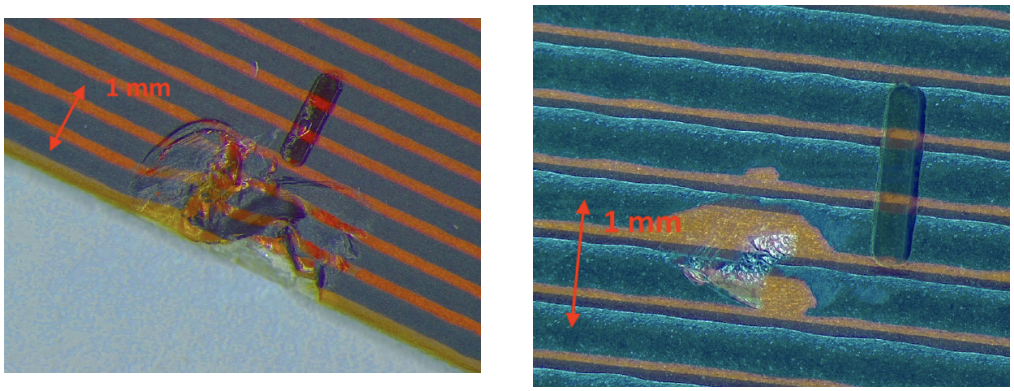

(a) (b)

Figure 5.7: Defect as edge damages or scratch of the Kapton® surface may lead to the rejection of the board

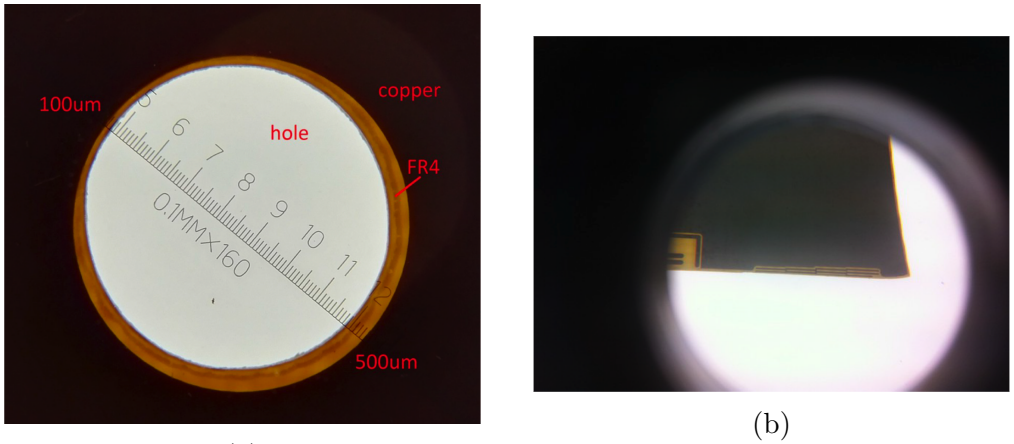

(a) (b)

Figure 5.8: Magnifying lenses allow to reveal the copper masks designed in the PCB to estimate drilling (a) and cut (b) precision

5.3.2 Backlight inspection

The backlight inspection desk, as the name suggests, is characterized by the presence of a light below the PCB surface, integrated in the table. The main goal of this inspection is to test the alignment of the resistive foil with respect to the copper pattern, the precision of the mechanical holes used later for the construction of the panels, the cleanness and the cut precision of the edges, checked with magnifying lenses. Most of these tests rely on the presence of copper masks in the PCB design, which are particularly evident if illuminated from below. Two examples are given in Fig. 5.8. On the left image a mechanical hole (a) is seen at the microscope. The precision of the drilling in the FR4 material is estimated with respect to the copper image, which is precise by design. On the right image (b), the precision of the cut is assessed by means of another mask, consisting of several echelons, allowing for a quick and visual measurement of the cut precision. Acceptance limits are rather tight. As already described in a previous chapter many PCB are used to make a single panel, but they could not overlap, or leave empty space between them. A cut precision of better than 250 µm is thus required.

The most important aspect investigated at backlight desk is to check the presence of all the pillars on the detectors surface. This test implies finding by eye the absence of even a single pillar, considering that a single board carries few thousand of them! On the other hand, if the pillars are the object keeping the mesh at the right distance, the absence of pillars will lead to a deformation of the mesh surface and a reduction of the distance between anode and cathode. As already seen this is not acceptable for detector operation. The adhesion of pillars is also tested with tape, and stressed by lateral forces. During the first phase of the PCB production many problems were raised from the low adhesion of pillars. If large fraction of pillars are missing, the board is sent to companies to perform a second coverlay lamination and pillar impression. If only few

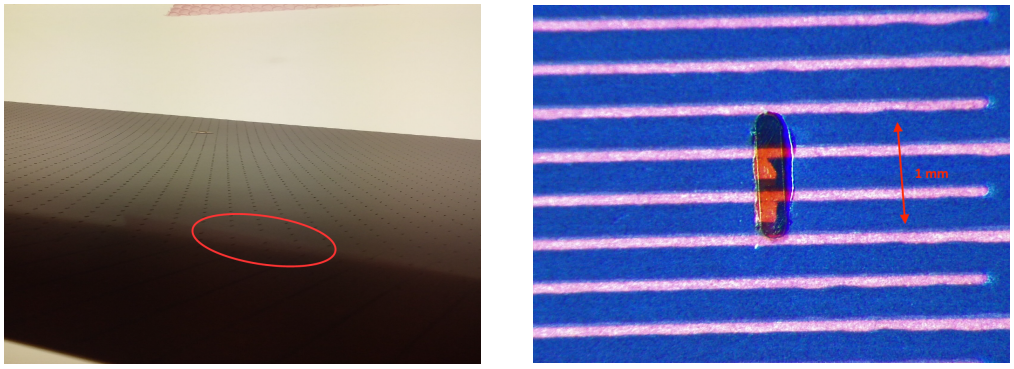

(a) (b)

Figure 5.9: Region of missing pillars precludes the good functioning of the detector (a). Reparation consists in regluing pillars one by one (b)

pillars are missing a dedicated reparation technique has been developed at CERN, consisting in the re-glueing of single pillars: first the region is polished with sandpaper, then a drop of glue is deposed, and finally a pillar (200 µm wide!) is placed in the right position. All this operation is performed at the stereo microscope. The time needed for a single pillar reparation is of about 30 minutes. An image of a region with many contiguous missing pillars is shown in Fig. 5.9 (a). On the right image (b) a picture taken with the stereo microscope of a reglued pillar is shown. After curing each single reglued pillar is checked and cleaned from glue excesses.

Another critical test is performed on the pillars, and it concerns the measurement of their height. The height is determined, at first, by the thickness of the two coverlay layers which are laminated on the resistive pattern, which is equal to about 60 µm each. Then several factors may arise, such a imperfect curing of the coverlay, an insufficient exposure to the UV light, leading to a reduction of the pillar height with respect to the nominal value. Pillars shorter than 80-100 µm cannot be accepted. In general, if known, a small systematic reduction can be tolerated for detector operation: as already seen, pillars determine the HV working point of the detector; if it is smaller the field needed at same gain will be lower. HV sectors having an homogeneous lower size of pillars can be grouped and operated at the appropriate voltages. What is, on the other hand, not acceptable, is the presence of dishomogeneities on the same HV sector. This implies region with different gain applied, whatever is the HV supplied, leading or to inefficient region, if the HV is tuned accordingly to the shortest pillars, or regions more prone to sparks and instabilities, if the HV is tuned according to the longest ones. A dedicated tool has been designed, composed of a flat and precise surface and four gauges: the tool sits on the pillars on the precise surface and the gauges measure the distance between the surface and the resistive pattern as shown in Fig. 5.10 (a). In case the gauge sits on a pillar, the distance measured is 0 by definition and the measurement is therefore discarded. The test in performed sampling different

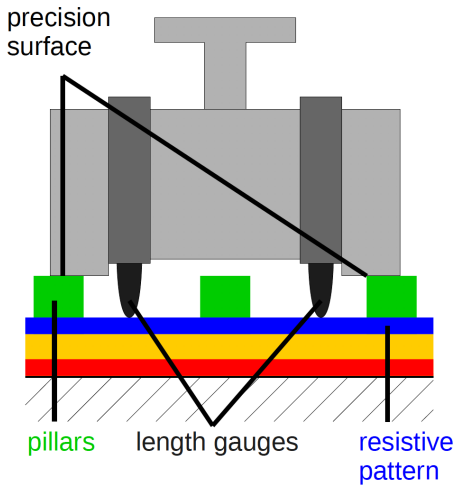

(a)

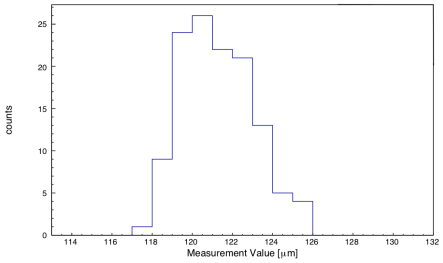

(b)

Figure 5.10: Pillar height measurement tool (a) based on precise surface sitting on the pillars and gauges to measure the height. Distribution of the pillar height for a board (b)

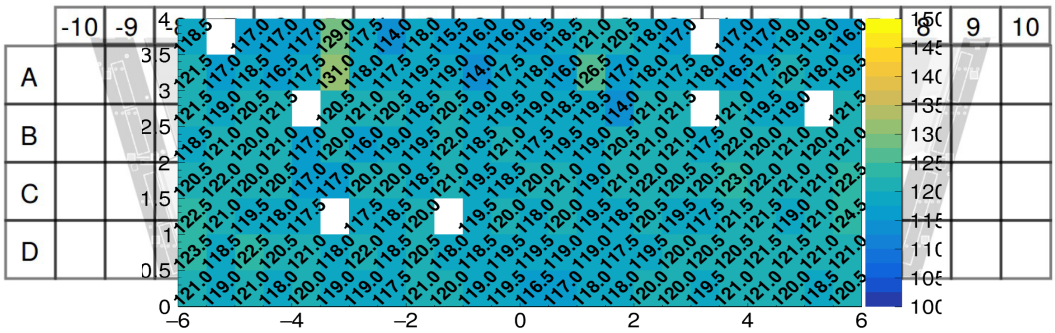

Figure 5.11: Pillar height map: systematic shift or low mean value automatically triggers an alarm in the web interface

regions of the boards, aiming to make a map of the pillars height and performing an automatic analysis of the homogeneity. Figure 5.10 (b) the distribution of the pillars height is reported for a board. The average value is about 120 µm. Figure 5.11 shows the distribution of the pillars height as a function of the position on the board. Large dishomogeneities can be dangerous for the detector operation, creating region with different amplification fields. An algorithm calculates the maximum difference between pillars at the right and left side of the board, and between the top and bottom part. The tool has been developed by a CERN/LMU/Tokyo collaboration.

The mean value of the pillar height measured so far on all the accepted board is shown in Fig. 5.12 as a function of the board type, without taking into account stereo/eta difference. The asymmetric errors on the values account

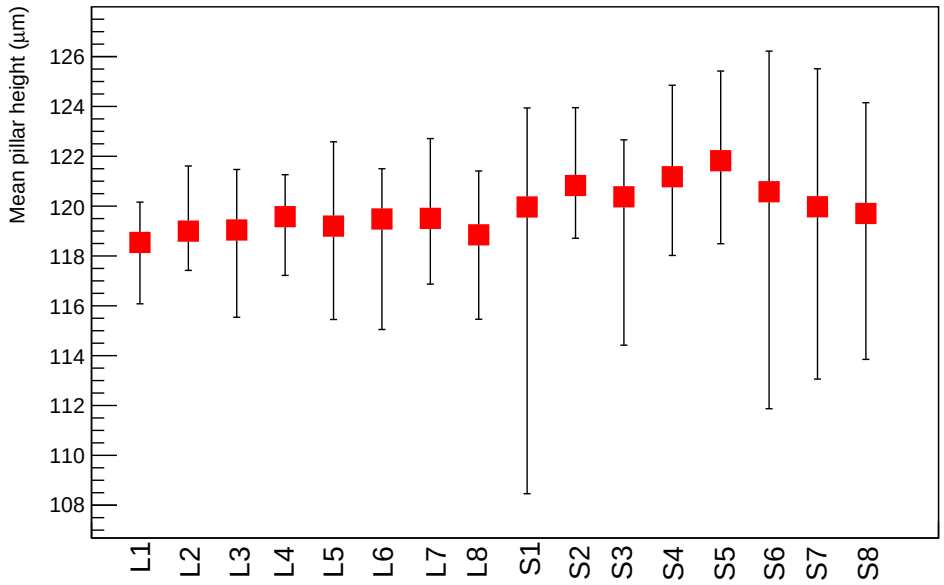

Figure 5.12: Pillar mean height as a function of the board type

for the minimum and maximum mean value among the boards considered. Among the different board types, the mean value is within ±1%, µm with a maximum fluctuation of ±8 µm observed with respect to the nominal value, still acceptable for a safe operation of the detectors if appropriately coupled to the HV channels.

5.3.3 Dimension measurement

The FR4 material is known to have an hygroscopic behaviour: it tends to expand accumulating water molecules. This effect has to be taken into account when building readout boards with dimension tolerances of the order of few hundreds of µm. In particular, copper images have been rescaled of -0.48 mm/m in short and -0.43 mm/m in long directions for what concerns ELVIA boards, while -0.43mm/m in short and -0.38mm/m in long direction for the ELTOS ones. The rescaling factors are based on measurements performed on a sample of pre-production boards, providing a benchmark of the expansion.
At CERN a dedicated dimension measurement is performed based on reading copper masks on the boards with c-CCD suveyors sitting on precise spheres. The position of the sphere is known at 10 µm precision. Taking into account the temperature stability of the granite table and the overall calibration of the system, an accuracy of 25 µm on the measurement is estimated. On the other hand, boards are subjected to expansion in the lab depending on the humidity by up to ±75 µm/m for ±10% humidity change. The acceptance criteria are different if the precise (short) dimension or the other one (long)

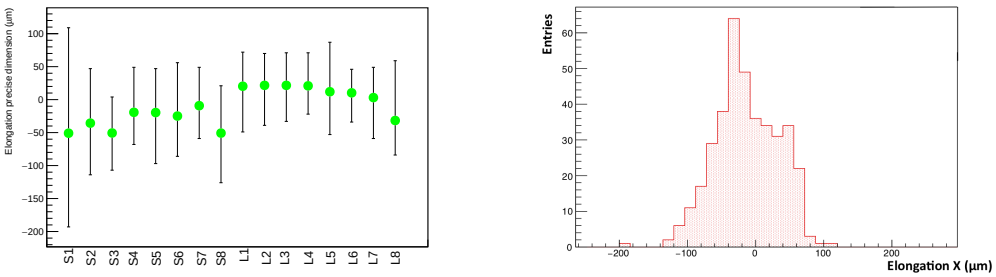

(a) (b)

Figure 5.13: Dimension test, precise (short) size: mean value of the elongation as a function of the board type (a), distribution of the elongation (b)

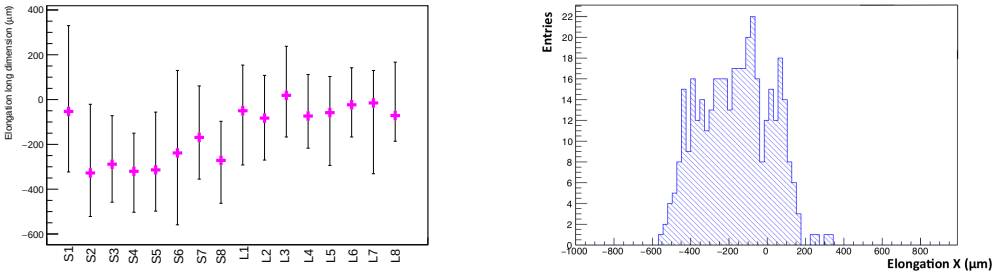

(a) (b)

Figure 5.14: Dimension test, less precise (long) size: mean value of the elongation as a function of the board type (a), distribution of the elongation (b)

are considered: for the short direction, an elongation of the board below 100 µm is required, while for the other one the requirement is loosen up to 500 µm. Figure 5.13 shows the results obtained on the boards accepted so far concerning the precise dimension. On the left plot (a) the observed elongation with respect to the design dimensions is reported as a function of the board type, without distinguishing between eta and stereo boards. The asymmetric error bars represent the minimum and maximum value of the elongation observed. Acceptance criteria have been set based on the experience and on potential risks for a safe detector operation. On the right (b) the elongation distribution is shown. More than 90 % of the boards lie within the ±100 µm interval. The equivalent plots related to the not-precise coordinate are reported in Fig. 5.14.

5.3.4 Resistivity measurement

The resistivity of the screen-printed pattern has been chosen to balance the particle rate capability and lower voltage drop at high current with resolution performance. Each foil goes through a detailed QC at Kobe (Japan), where they are produced and then shipped to CERN. At the companies, the glueing of the resistive pattern on the FR4 is performed at very high temperature and

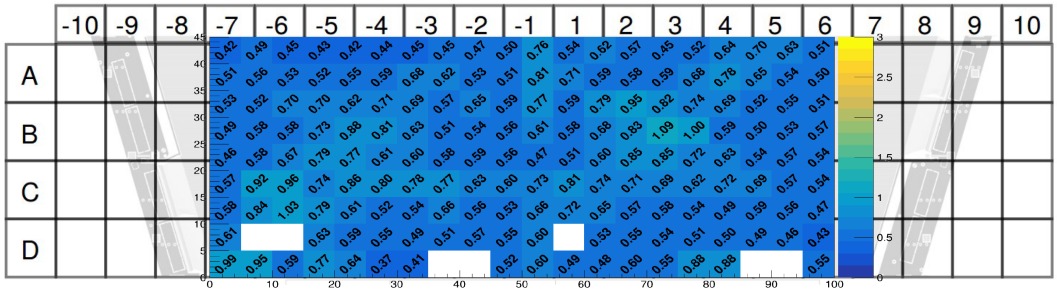

Figure 5.15: Map of the resistivity: changes in the values with respect to the QC performed in Japan may due to construction issues

pressure conditions. A change in the resistivity can be due to a problem in the production: pressing and polishing issues, coverlay not fully cured, mechanical stress. In collaboration with Tokyo and Wuerzburg colleagues a dedicated tool has been developed to remeasure the resistivity of the pattern and provide a direct comparison of the results before and after the glueing for the specific foil. The test is thus performed once in Japan, during the foil production and quality control, and once at CERN, after the glueing of the foil on the PCB. The tool is composed of 99 probes, mounted on acrylic glass template. Probes are alternatively readout by a multimeter, measuring the resistance. The final outcome is a resistance map as a function of the position on the board, as shown in Fig 5.15. The acceptable resistivity ranges from 0.3 to 2.5 $M\Omega/cm^2$. The mean value of the resistance, moreover, cannot increase of more than a factor 3 with respect to the measurement performed in Japan. Also in this case an automatic analysis tool suggests the user the decision to take depending on the results of the tests.

Figure 5.16 shows the results obtained from a board rejected for abnormal resistivity increase. In the left image a comparison between the pattern resistivity measured in Japan and after gluing on the PCB is reported, showing an increase of the mean value of the resistivity of more than a factor 3. The right image shows the resistivity map on the whole surface: a systematic large value of resistivity on the board, as it is shown in Fig. 5.16 (b) may cause its rejection.

5.3.5 RO strips capacitance measurement

Copper readout strips are not visible by eye, being hidden below the resistive pattern and the Kapton® layer. Their integrity is, on the other hand, *conditio sine qua non* for the detector operation. Strip cuts will simply create dead regions in the detector. The strip integrity is evaluated by measuring the capacitance of the strip with respect to the HV line (the place where the HV will be supplied in the final and assembled module). The value obtained depends on the length of the readout strips; if a strip is cut, the expected capacitance will drop. The tool, built at CERN, is shown is Fig. 5.17a. While

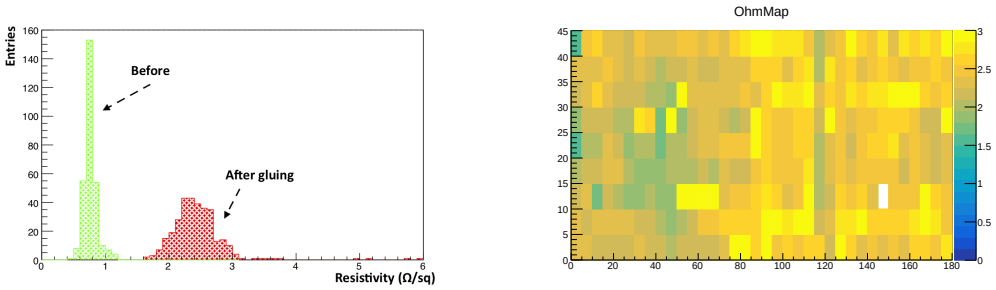

(a) (b)

Figure 5.16: Distribution of the resistivity before and after the glueing of the resistive foil (a). Bi-dimensional map of the resistivity (b)

a probe of the capacitance meter is kept connected to the HV line, the second one is coupled to a vertical and horizontal stages and moved by a motor, allowing to measure each strip separately. An example of strip capacitance as a function of the strip number is shown in Fig 5.17b. A typical value of about 100-150 pF (depending on the board size) is found for good strips. Few strips showing lower capacitance can arise from a bad contact of the tip with the strip. In few cases the measured capacitance is close to zero, due to broken or cut strips. Less than 3% of the strips should have a low capacitance, taking into account a 1-2% arising from false positive. It is worth to mention that a major production issue has been found and investigated thanks to this test; few details are given in the following. The copper strips, running all along the board, need to be coated with Silver paste in the region where the front-end electronic boards will be plugged. This coating is performed immersing the PCB on a chemical Ag bath, allowing the Ag to deposit according to a predefined pattern. The chemicals, however, also attack and dissolve the glue between readout and Kapton® layers as well, leaving some Cu material uncovered by the silver, (due to the too short time in the Ag bath, since most of it is taken by the dissolution process) but in contact with the neighbouring coated surface. This creates a chemical cell, leading in short time to the dissolution of the copper, resulting in the cut of the strip. The effect is shown in Fig 5.18. In the first image the interface between the silver coated strips and the not-coated, but covered with Kapton® is shown. No sign of cut is visible from this image. A small portion of Kapton® is then removed with a scalpel: at the interface, where the glue has been attacked by the chemicals, the copper has dissolved and no connection is present. A large fraction of the first PCB production was affected by this issue and some problematic boards have been rejected. The solution was found by doing a very quick first Ag deposition, about 0.1 µm thick, not long enough to attack the glue, followed by a longer deposition, but with the shrewdness of protecting the interface with additional Kapton® tape. In this way the glue is not attacked, no Cu dissolution takes place with the only contraindication that at the interface the thickness of Silver is thinner.

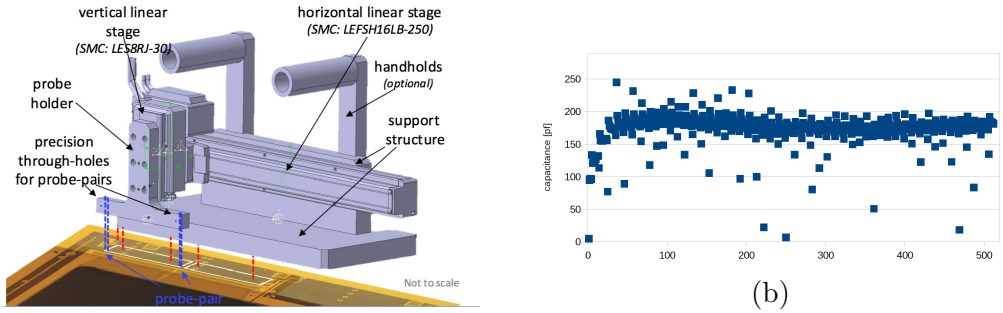

(a) (b)

Figure 5.17: Strip capacitance tool (a) and example of strip capacitance as a function of strip number (b)

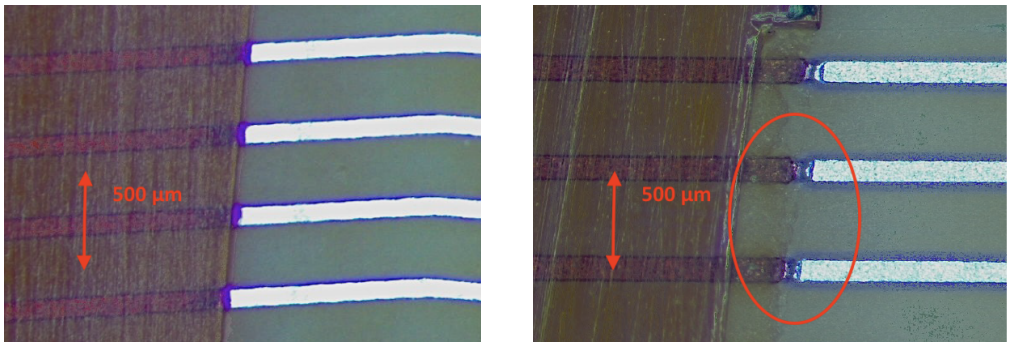

(a) (b)

Figure 5.18: Interface between Ag and Kapton® coated copper (a). Same region after removing a small portion of Kapton®: the glue has been attacked by the chemicals bath, copper has been dissolved and connection is broken

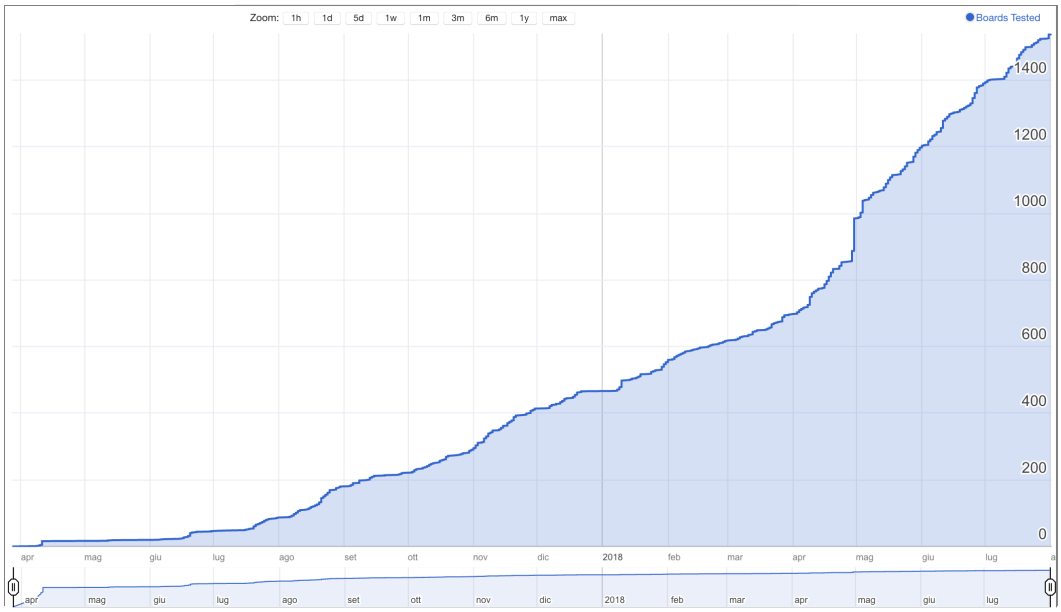

Figure 5.19: Boards tested as a function of time since April 2017

5.4 Status of PCB QC and delivery

Board deliveries started in April 2017. Since then an optimization of the QC and production allowed the speed up of the procedures to a rate sufficient to satisfy the module production requirements of about 40 boards per week. At the time of writing, end of July 2018, about 1500 boards have been checked, out of 1600 delivered by the companies. Out of this 1500 boards, about 800 have undergone the final inspection and declared suitable to become part of the new detector or rejected. The progression is clearly visible in Fig 5.19, which reports the cumulative number of boards tested as a function of time. So far, the rejection factor (percentage of boards rejected) is about 30%, but takes into account several major issues, now solved, that took place in the very first phase of the production, which lead to a systematic rejection of entire batches of newly delivered boards. Recent deliveries show a better percentage, close to 90% of acceptance.

Figure 5.20 shows the final grades obtained by the boards grouped in the different sections as provided by the online form. Four grades are available, *OK* if no defects/problems are found, *Minor* as a warning flag, *Bad* if major issues are observed, or *Unknown* if, for example, the tests in the section are not even performed due to a major rejection issue in a previous one. As clearly visible the section causing the highest percentage of rejection is the toplight. As already mentioned the toplight tests are devoted to spot bumps, damages of defects on the surface of the boards. Also the dimension test fails quite often; in this case, however, a red flag does not correspond to a direct board rejection. All these summary plots are directly available from a dedicated web page, providing also more insights concerning the quality of the boards QC and

Figure 5.20: Summary results on PCBs for each single section of the web form

a detailed picture of past deliveries and logistic. In total 2200 readout boards are needed to build the two New Small Wheels. The quality control of PCBs is expected to finish middle of 2019, at a rate of about 40 boards delivered to the construction sites per week.

Chapter 6

Search for Dark Matter produced in association with top quarks

In the following chapter a search for evidences of physics beyond the Standard Model is presented. In particular a signature of a Dark Matter candidate coupled to the Standard Model sector by means of a scalar or pseudoscalar mediator is investigated. The analysis has been the result of the common effort of a large group of people, in particular from the Bern group, the CERN group, and the Pavia group. I personally actively contributed to the analysis in many aspects, in particular being responsible of the normalization of the main irreducible background.

6.1 The Model

As already described in the introductory chapter to Dark Matter, Simplified Models have been introduced in order to overtake the limitations of the Effective Field Theories (EFT) when the momentum transferred becomes not negligible with respect to the mass of the heavy particles. They describe a single exchanged particle, without the need of introducing a complex UV-complete model as, for example, SUSY inspired models. The Simplified models are also attractive for the simplicity of accommodating them in the context of the Standard Model, as, for example, in Higgs extended sectors.
The target of this search is a scalar and pseudoscalar mediated simplified model having, in its general formulation, 5 parameters [66]. The dark matter particle, χ is a Dirac fermion, the mediator is called ϕ if scalar and a if the pseudoscalar

case is considered. The two Langrangians take respectively, the form:

$$\mathcal{L}_\phi = \mathcal{L}_{SM} + \frac{1}{2}(\partial_\mu \phi)^2 + \frac{1}{2}m_\phi^2\phi^2 + i\bar{\chi}\partial\!\!\!/\chi - m_\chi\bar{\chi}\chi + g_\chi\phi\bar{\chi}\chi - \sum_{fermions} g_\nu \frac{y_f}{\sqrt{2}}\phi\bar{f}f \tag{6.1}$$

$$\mathcal{L}_a = \mathcal{L}_{SM} + \frac{1}{2}(\partial_\mu a)^2 + \frac{1}{2}m_a^2 a^2 + i\bar{\chi}\partial\!\!\!/\chi - m_\chi\bar{\chi}\chi - ig_\chi a\bar{\chi}\gamma^5\chi - \sum_{fermions} ig_\nu \frac{y_f}{\sqrt{2}}a\bar{f}\gamma^5 f \tag{6.2}$$

where $\mathcal{L}_{SM}$ is the Standard Model Lagrangian, m_χ is the mass of the dark matter particle, the mediator masses are described by m_a and m_ϕ. The dark matter-mediator coupling is parametrized by g_χ, being g_q the one with the Standard Model particles. It is assumed that g_q is universal for all quarks and leptons families. The mediator width is chosen to assume the minimal value. In the analysis a further assumption is made, imposing $g_\chi = g_q = g$.

The coupling to the SM fermions is severely restricted by precise measurements of the flavour symmetry. In the Minimal Flavour Violation (MVF) scenario, as described in [29], compatible with the observation, the interaction between the fermions and the spin 0 mediator is proportional to the mass of the fermions via a Yukawa coupling, thus enhancing for third generation fermions. As for the SM Higgs, mediators are more likely to be produced at the LHC via loop-induced gluon fusion or in association with heavy quarks (top or bottom). A first channel exploited in the search for scalars and pseudoscalars foresees high momentum jets in the final state recoiling against missing transverse energy, both from ATLAS and CMS Collaborations as reported in [67] and in [68] respectively. CMS addressed Dark Matter production in association with heavy quarks in a search published in 2017 and described in [69], by using 2.2 fb^{-1} of data taken at $\sqrt{s} = 13$ TeV. Limits on the model have been obtained from the combination of the $t\bar{t}$ and $b\bar{b}$ search channels. More recently another analysis has been released by CMS, based on 36.1 fb^{-1} of data and targeting Dark Matter production in association with top quarks. More details on the analysis can be found in [70]. Upper limits on the signal strength are reported in Fig 6.1, for both scalar and pseudoscalar mediators.

ATLAS has performed, so far, searches focusing on final states characterized by fully hadronic or dileptonic top quark pair decays targeting supersymmetric partners of the top quarks as described in Ref. [71, 72]. The channel where one W decays hadronically and one into leptons, has been exploited in the context of the search for top squarks [73]. It should be reminded that these searches have been optimized to maximize the sensitivity with respect to supersymmetric scenarios, kinematically different if compared to DM simplified models.

In this analysis the associate production of $t\bar{t}\ \chi\chi$ is investigated, as a function of the mediator and Dark Matter masses, with both the top quarks decaying leptonically. The final state is thus characterized by two leptons, two b-jets and $E_{\mathrm{T}}^{\mathrm{miss}}$ from both the neutrinos and the Dark Matter particles.

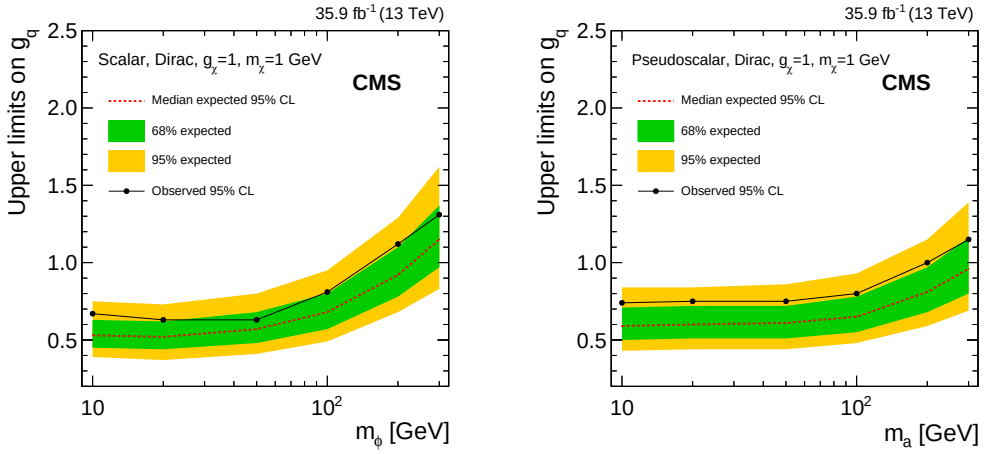

(a) (b)

Figure 6.1: Upper limits at 95% and 68 CL% on the coupling strength of the mediator to the Standard Model quarks for a scalar (a) and pseudoscalar mediators (b). Fermionic Dark Matter of 1 GeV and $g_\chi = 1$ are assumed

The relevant Feynman diagram at the lowest order is shown in Fig. 6.2.

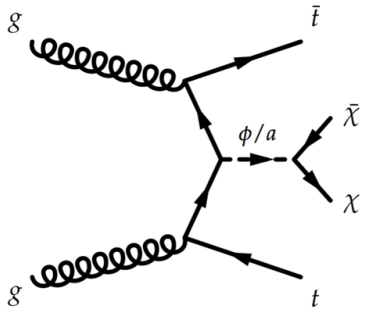

Figure 6.2: Feynman diagram for $t\bar{t}\chi\chi$ production though an s-channel spin-0 mediator.

The analysis aims to maximize the sensitivity to the model, providing an interpretation in terms of the dark matter mass (m_χ), having fixed the mediator mass (m_a or m_ϕ if pseudoscalar or scalar respectively) at 10 GeVor as a function of the mediator masses having fixed the dark matter mass to 1 GeV. The signal process samples have been generated at LO matrix with up to one extra parton, using the MadGraph v2.2.3 [74]. Parton showering and hadronisation have been modelized using generator Pythia 8.186 [75] with the A14 [76, 77, 78] tune. Parton luminosities are provided by the NNPDF30LO PDF set [79]. NLO k-factor have also been evaluated and taken into account to correct the LO cross sections. A briefly description of Montecarlo event generators (MC) is given in the next section.

6.2 Monte Carlo

Event generators interfaced to parton shower algorithm are employed to describe the background processes and to simulate the beyond Standard Model signal. A exhaustive dissertation on Monte Carlo tools available and the state of the art can be found at Ref. [80]. Here below a short description of the most relevant Monte Carlo event generators used in this analysis is provided.

- MadGraph5_aMC@NLO is a framework simulating process at LO accuracy for any user-defined Lagrangian, and at NLO for QCD and EW corrections to SM processes. It also provides the possibility of computing cross sections, generating hard events and matching with event generators [74].
- Sherpa [81] is a Matrix Element event generator interfaced with a parton shower. Several types of collisions are supported, such as lepton-lepton, lepton–photon, photon-photon, and of course, proton-proton.
- POWHEG [82, 83, 84] provides calculations at NLO accuracy. It can be interfaced to all Monte Carlo shower programs supporting the Les Houches Interface.

6.3 Data samples

Data used in this analysis has been collected in 2015 (from June to November) for a total integrated luminosity of 3.2 fb^{-1} and in 2016, from April to October for other 32.9 fb^{-1}. In total the available data corresponds to 36.1 fb^{-1}. Only datasets with the detector fully operating are taken into account in the analysis. Both data and MC simulations have been processed by the same reconstruction algorithm briefly described in the following section.

6.4 Background processes

All the Standard Model processes containing 2 leptons and jets in the final state are considered as background. Out of these, in particular, $t\bar{t}$ is expected to have larger contribution (reducible background), followed by the $t\bar{t}Z$, with the Z boson decaying into two neutrinos, which is, on the other hand, an irreducible background. Other processes include diboson (WZ and ZZ), $t\bar{t}W/Z/\gamma^*$, $t\bar{t}h$, $t\bar{t}W/Z/\gamma^*$. In Table 6.1 the background process simulated, with the details of the event generator used, the parton shower, the PDF and tune used, in agreement with the ATLAS recommendations, are reported.

MC samples are then processed through the ATLAS Geant4 simulation, to describe the detector response. Concerning the $t\bar{t}t$ process, a parametrization of the calorimeter response is also used [98]. Additional proton proton collisions are added both on-time and out-of-time (if belonging to the same bunch or a

Table 6.1: Simulated signal and background event samples: the corresponding generator, parton shower, cross-section normalisation, PDF set and underlying-event tune are shown.

Physics process	Generator	Parton shower	Cross-section normalisation	PDF set	Tune
$Z/\gamma^*(\to \ell\ell)$ + jets	Sherpa 2.2.1 [81]	Sherpa 2.2.1	NNLO [85]	NLO CT10 [86]	Sherpa default
$t\bar{t}$	powheg-box v2 [82]	Pythia 6.428 [87]	NNLO+NNLL [88, 89, 90, 91, 92, 93]	NLO CT10	Perugia2012 [94]
Wt	powheg-box v2	Pythia 6.428	NNLO+NNLL [95]	NLO CT10	Perugia2012
$t\bar{t}W/Z/\gamma^*$	MadGraph5_aMC@NLO 2.2.2	Pythia 8.186	NLO [74]	NNPDF2.3LO	A14
Diboson	Sherpa 2.2.1	Sherpa 2.2.1	Generator NLO	NLO CT10	Sherpa default
$t\bar{t}h$	MadGraph5_aMC@NLO 2.2.2	Herwig 2.7.1 [96]	NLO [97]	CTEQ6L1	A14
Wh, Zh	MadGraph5_aMC@NLO 2.2.2	Pythia 8.186	NLO [97]	NNPDF2.3LO	A14
$t\bar{t}WW$, $t\bar{t}t\bar{t}$	MadGraph5_aMC@NLO 2.2.2	Pythia 8.186	NLO [74]	NNPDF2.3LO	A14
tZ, tWZ, $t\bar{t}t$	MadGraph5_aMC@NLO 2.2.2	Pythia 8.186	LO	NNPDF2.3LO	A14
Triboson	Sherpa 2.2.1	Sherpa 2.2.1	Generator LO, NLO	CT10	Sherpa default

nearby one respectively). MC events are also reweighed so that the distribution of the average number of proton proton collisions per bunch crossing matches the data.

6.5 Event reconstruction

The ATLAS sub-detectors, described in the second chapter of the thesis, provide information concerning the particles as electric signals. These need to be interpreted and converted into meaningful physical objects usable by the analysis teams. This procedure is called reconstruction, and it should take into account all the detector peculiarities and performance. In this section, in particular, some details concerning the reconstruction of leptons (electrons and muons), jets (and b-jets) and missing transverse energy, used in the analysis, will be given.

6.5.1 Leptons

Muons

Muons are reconstructed independently in the Inner Detector and in the Muon Spectrometer. In the Muon spectrometer a hit pattern is searched in the MDT detectors in the bending plane by means of a Hough Transform. RPCs and TGCs contribute to the estimation of the perpendicular coordinate. Tracks are then built fitting together the hits reconstructed in the different detectors layers. The fitting procedure is based on a χ^2 minimization: hits providing large contributions are removed from the fit. Four *types* of muons are considered, depending on which detector is used in the reconstruction:

- Combined (CB) muons. Muons are reconstructed combining information from both the Inner and Muon spectrometer (MS). A global fit is performed using all the hits. Muons are usually recostructed with an

outside-in pattern recognition, where candidates are first reconstructed in the MS and then combined to Inner detector tracks.

- Segment-tagged (ST) muons. In this case Inner detector tracks are matched to one segment in the MS when extrapolated. This allows the reconstruction of muons at low p_T or passing through regions at low acceptance.

- Calorimeter-tagged (CT) muons. Inner detector tracks can be matched to energy deposit in the calorimeter, compatible with a MIP. This technique allows the rescuing of muons in the region at $|\eta| < 0.1$ with a momentum ranging between 15 and 100 GeV.

- Extrapolated (ME) muons. Muon tracks are reconstructed only in the MS. It is useful to extend the acceptance where the ID is not present ($2.5 < |\eta| < 2.7$).

Different muons reconstructions are adopted to satisfy the needs of different physics analyses:

- *Medium* muons: CB and ME tracks are considered, with supplementary requirements on the number of MDT/CSC hit multiplicities. Compatibility between the momentum reconstructed in the Inner and Muon detectors is also required to reject background.

- *Loose* muons: it extends the *Medium* selection including also CT and ST muons in the $|\eta| < 0.1$ region.

- *Tight* muons: it is designed to improve the muon quality, sacrificing the efficiency. It requires *Medium* muons with tight conditions on the quality of the combined fit to ensure stronger background rejection.

- *High* p_T muons: it is a selection designed for tracks with transverse momentum above 100 GeV and it requires at least three MS stations, leading to a reconstruction efficiency reduction of about 20%.

The muon reconstruction efficiency is measured as a function of η for different selection requirements with a *tag and probe* method using $Z \to \mu\mu$ events: a first muon is identified using tight criteria, the second is reconstructed by means of an orthogonal method and its invariant mass combined with the first electron should match the Z mass. Reconstruction efficiency can therefore be calculated for the second muon. As example the reconstruction muon efficiency for *Medium* muons is shown as a function of η for both data and MC in Fig. 6.3. Bottom plot shows the ratio of the measured efficiencies to the ones predicted through MC simulations.

Another powerful tool to improve the background rejection is the detector activity around the muon candidate, known as *isolation*. Two variables have been defined to assess the isolation, the track-based isolation variable, $p_T^{varcone30}$

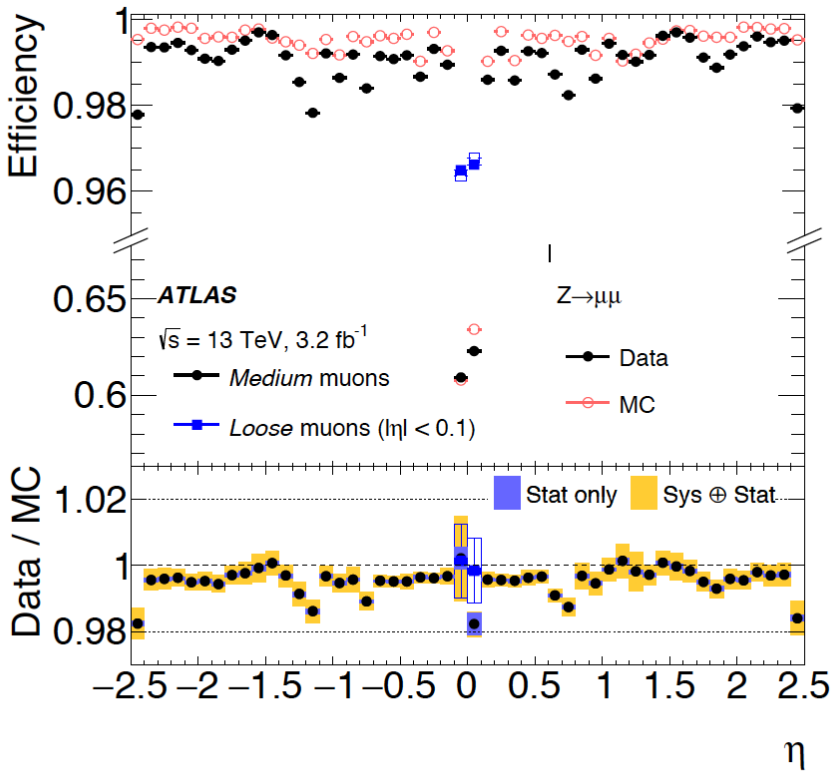

Figure 6.3: Reconstruction muon efficiency for *Medium* muons as a function of η

and the calorimeter-based isolation variable $E_T^{topocone20}$. The first is defined as scalar sum of the transverse momenta of the tracks with p_T >1 GeV in a cone of size $\Delta R = min(10 \quad GeV/p_T^{\mu}, 0.3)$, while the second is defined as the sum of the transverse energy of topological clusters in a cone of size $\Delta R = 0.2$ around the muon candidate. Seven working points are defined based on the ratio between the isolation variables and the muon momentum. Further details can be found in [99].

Electrons

Electrons reconstruction in the barrel region is based on the combination of information from both the Inner detector and the EM calorimeter. To reconstruct the EM energy in the calorimeter, a sliding window algorithm is applied, across the calorimeter towers, looking for total cluster transverse energy deposits above 2.5 GeV. For each EM seed a Region of Interest (RoI) is opened around the seed barycentre. The track in the Inner detector is obtained by means of a pattern recognition algorithm, based on a Kalman filter-smoother

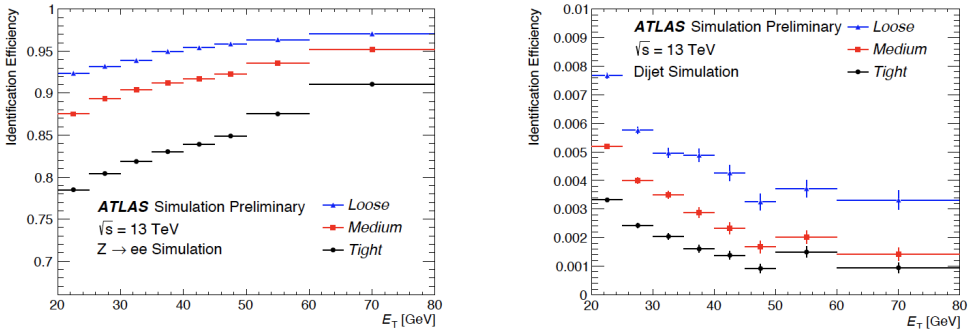

(a) (b)

Figure 6.4: Electron reconstruction efficiency and background rejection as studied on $Z \rightarrow ee$ events

formalism. Tracks are then combined with EM seed information. The initial electron candidates are likely to contain background objects such as hadronic jets or converted photons, requiring further identification algorithms (ID). The ID algorithms take profit of various quantities related to the electron clusters and track measurements such as calorimeter shower shapes, track properties, and variables measuring radiative effects. The main algorithm is the likelihood based (LH) method, based on the simultaneous evaluation of several properties of the electron candidates. Three levels of identification operating points are provided for electrons. These are *Loose, Medium, and Tight* and they are based on the use of different set of variables. The electron reconstruction efficiency and background rejection are studied on $Z \rightarrow ee$ events, for the three different selections and are shown in Fig 6.4.

As for muons, isolation information is also useful for improving background rejection, in particular discriminating the *prompt* electrons (such as coming from heavy resonance decays) from non-isolated electron candidates for example originating from converted photons produced in hadron decays, or electrons from heavy flavour hadron decays, or hadrons mis-identified as electrons. As in the muon case, two variables based on the calorimeter activity around electron candidate energy cluster and on the transverse momentum in a cone $\Delta R = min(10 \quad GeV/p_T^e, 0.2)$ around the electron track are considered. The same identification working point already mention for muons are defined for electrons. More insight can be found at Ref. [100]

Leptons selection

The analysis described in this write-up relies on both electrons and muons. In both cases two categories of objects have been considered, with different isolation and selection requirements, *baseline* and *signal*. *Baseline* leptons are required to satisfy the *Loose* requirement, having $E_T > 7$ GeV and $|\eta| < 2.47$. *Signal* leptons, on the other hand, need to pass the *Medium* selection

requirement, have $E_T > 20$ GeV, pass the *GradientLoose* isolation working point.

6.5.2 Jets

Jet reconstruction

Partons produced in the interaction undergo an hadronization process, generating collimated jets approximately in the direction of the original parton. Jets may develop complex structures: their reconstruction is of crucial importance to reconstruct the original physical properties of the parton originated in the hard process. The baseline algorithm used in ATLAS is the so called ANTI-KT algorithm [101]. It uses topological clusters based on energy deposition in the calorimeter as input, defining their respective distances d_{ij} and their distances with respect to the beam axis (d_{iB}) as follows:

$$d_{ij} = min(k_{Ti}^{2p}, k_{Tj}^{2p}) \frac{\Delta_{ij}^2}{R^2} \tag{6.3}$$

$$d_{iB} = k_{Ti}^{2p}, \tag{6.4}$$

where $\Delta_{ij}^2 = (y_i - y_j)^2 + (\phi_i - \phi_j)^2$ being k_{ti}, y_i and ϕ_i respectively the transverse momentum, rapidity and azimuth of particle i. p and R are intrinsic parameters of the algorithm. In the ANTI-KT algorithm $p = -1$ and R, the radius parameter, is by default equal to 0.4. The clusterization algorithm sequentially finds the smallest quantity between d_{ij} and d_{iB}. If it is the first, objects are merged in a single entity, if it is the second the object i is considered as a jet and removed from the list of entities. The jet energy reconstructed needs to be corrected for several detector effects, such as calorimeter non compensation, detector imperfection, contribution from pile-up [102] events, which accounts for additional proton-proton collisions (both *in-time* and *out-time*). In particular the energy from pileup interactions is typically subtracted from the signal interaction of interest by means of two variables, combining information from both the calorimeters and the Inner detector [103]. The first is the jet-vertex-fraction (corrJVF), defined as the sum of the scalar transverse momentum of the tracks that are associated with the jet and originating from the hard-scatter vertex, divided by the scalar sum of the transverse momentum of all associated tracks and taking into account the momentum of the tracks originating from pile-up interactions. The second one, R_{pT} is defined as the scalar transverse momentum sum of the tracks that are associated with the jet and originate from the hard-scatter vertex divided by the fully calibrated jet momentum. A discriminant called the jet-vertex-tagger (JVT) is constructed using the two mentioned variables as a 2-dimensional likelihood. Without entering into details, Figure 6.5 shows the distributions of the corrJVF and R_{pt} for Hard Scatter jest (HS) and Pile-up jets (PU) for jest with momentum ranging from 20 to 30 GeV.

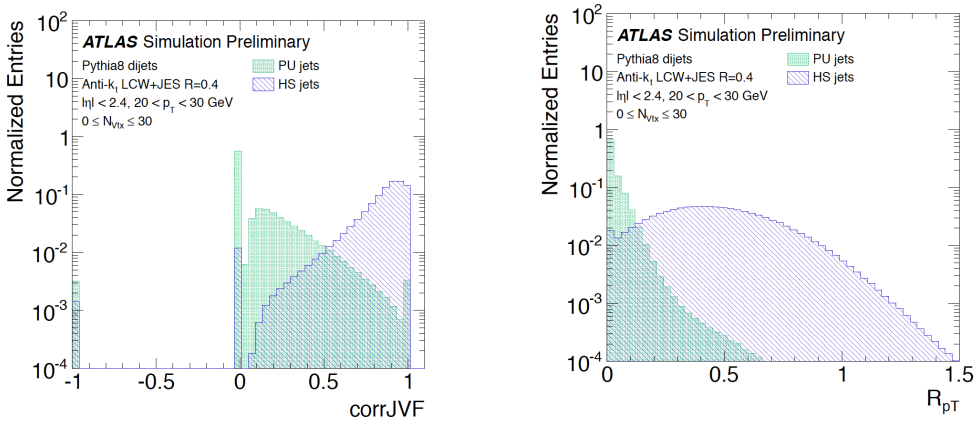

(a) (b)

Figure 6.5: corrJVF (a) and R_{pt} (b) distributions for Hard Scatter jest (HS) and Pile-up jets (PU) for jest with $20 < p_T < 30$ GeV

Finally, the jet energy and direction are corrected by terms derived from the comparison of kinematic observables of reconstructed jets and truth jets as obtained in MC simulations. Systematic uncertainties on the Jet Energy Scale calibration are also derived and used in the analysis. A detailed description of the procedure can be found at Ref. [104] and [105].

b-tagged jets

The possibility to identify jets produced by the hadronisation of a bottom quark, is a crucial aspect of many analyses. It is based on the long lifetime of hadrons containing bottom quarks, leading to displaced vertexes with respect to the hard-scatter interaction point. *b-tagging* algorithms take profit of trajectories reconstructed in the Inner detector, and they follow three different strategies: impact parameter based algorithms, secondary vertex finding algorithm (SV) and decay chain multi-vertex algorithm (JetFitter). Impact parameter based algorithms use the information of the transverse impact parameter (d_0), which is the distance in the $r - \phi$ plane of the track to the primary vertex and the longitudinal impact parameter ($z0 \sin\theta$) to distinguish b-hadrons decay products due to their large values. A log-likelihood-ratio (LLR) discriminant is built for b-jets, c-jets and light jets separations.
The vertex based algorithm explicitly reconstructs inclusive secondary vertexes, while the JetFitter algorithm tries to reconstruct the full b-hadron decay. A combination of the output of the above mentioned algorithm is used as input parameter for a Boosted Decision Tree algorithm (BDT). Different training samples have been used varying the percentage of the c-jet fraction in the training. The MV2c10 algorithm, suggested for ATLAS analyses, for example, uses a 7% c-jet fraction in the training. Different working points can be defined cutting on the MV2 output, leading to different rejection performance

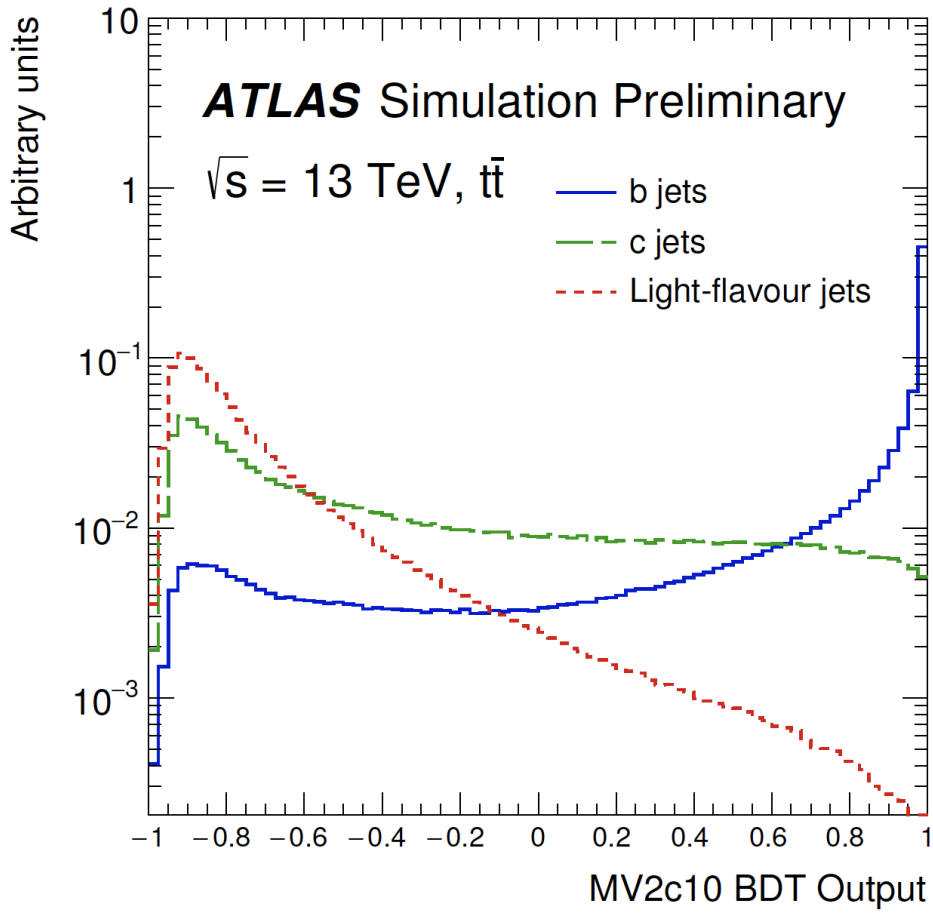

Figure 6.6: BDT MV2c10 output for b-jets, c-jets and light flavour jets

of light and c-jets. The distribution of the MV2c10 BDT output for b-jets, c-jets and light-flavour jets is reported in Fig 6.6. More details are given in Ref. [106].

Jet selection

Jets in the analysis have been reconstructed using the already described anti-k_t algorithm, with the default choice of $R = 0.4$. Jets have been considered if having at least $p_T > 20$ GeV and lying within $|\eta| < 2.5$. To reduce pile-up contributions jets with JVT$<$ 0.59 are rejected if having $p_T < 60$ GeV. Concerning b-jets, the MV2c10 tagging algorithm has been used, at the 77% working point.

6.5.3 Transverse missing energy

Interesting events at LHC involve hard scattering of partons with high momentum transfer. These events are energy balanced in the transverse plane, but

not along the beam axis. An imbalance in the vector sum of visible transverse momenta is known as missing transverse momentum $\mathbf{p}_{\mathrm{T}^{miss}}$, with magnitude $E_{\mathrm{T}}^{\mathrm{miss}}$. A large amount of missing transverse momentum may indicate the presence of particles escaping the detector, such as weakly interacting particles (neutrinos in the SM) or, if Beyond Standard Model (BSM) models are considered, possible unseen new particles. $E_{\mathrm{T}}^{\mathrm{miss}}$ is reconstructed starting from calibrated objects as follows:

$$E_{x(y)}^{miss} = E_{x(y)}^{miss} + E_{x(y)}^{miss,e} + E_{x(y)}^{miss,\gamma} + E_{x(y)}^{miss,\tau} + E_{x(y)}^{miss,jets} + E_{x(y)}^{miss,\mu} + E_{x(y)}^{miss,soft}, \tag{6.5}$$

where each term is the negative sum of the momenta for the respective calibrated objects. The last term of the sum includes transverse energy deposit not associated with any reconstructed object. Several algorithms have been developed to estimate this contribution, influencing performance and $E_{\mathrm{T}}^{\mathrm{miss}}$ uncertainty. More details are given in Ref. [107].

6.6 Analysis strategy

The strategy adopted in this analysis is here summarized:

- A region in the phase-space is defined, enriched in signal (signal region). The selection optimization is performed only relying on the Monte Carlo simulations and aims to provide the best sensitivity possible. The results and final interpretation on the signal models will be provided from this region

- Background contributions in the signal regions are estimated via Monte Carlo simulations. For most relevant processes ($t\bar{t}$ and $t\bar{t}Z$) a data driven approach has been used, defining dedicated selections (control regions) enriched in the background process without strong contamination of signal. These regions need to be kinetically close to signal region, but orthogonal to it. In the control regions the background normalization is derived and then reported to the signal region.

- The background normalization obtained from control regions is tested on validation regions: also in this case the orthogonality with the signal region needs to be granted.

- Finally a simultaneous fit of both the signal and background enriched regions is performed and an hypothesis test is performed on the signal strength. If no excess is found exclusion limits on the signal models are derived.

6.7 Event selection

The analysis focuses on a final state including two leptons, two b-jets and $E_{\mathrm{T}}^{\mathrm{miss}}$. The initial phase of the analysis is a preselection stage selecting events with the final state topology. The kinematic cuts applied are the following:

- Events with at least 2 tracks associated to the primary vertex are considered
- Exactly two signal leptons. They could be same flavour (SF) or different flavour (DF), but they are required to have opposite charge
- The invariant mass between the two leptons ($m_{\ell\ell}$) is required to be greater than 20 GeV and, in case of two SF leptons, not lying within 20 GeV from the Z mass peak. This last choice has been made to suppress backgrounds containing Z bosons.
- The transverse momentum of the leading lepton is required to be greater than 25 GeV. The sub-leading lepton is required, moreover, to have a p_T greater than 20 GeV.

In Figure 6.7 a comparison between data and MC simulations is reported for two of the most relevant observables, $m_{\ell\ell}$ and $E_{\mathrm{T}}^{\mathrm{miss}}$ for three distinct cases: when the two leptons are of opposite flavour, when both are electrons, and when both are muons.

The agreement between data and MC expectation is good. The most relevant contributions to be background come from dibosons, Z+jets, $t\bar{t}$ and Wt productions. These processes are reducible backgrounds; in order to discriminate between background and signal kinematic variables have been exploited, as described in the following. The remaining relevant background process is $t\bar{t}Z$ with Z boson decaying into neutrinos. In this case the event topology is exactly as the target signal and the background process is irreducible. For each observable described below, the comparison between data and MC is provided, with two additional requirements on the events:

- One jet is required to be *b-tagged*
- The variable m_{T2}, defined in the following, is required to be greater than 100 GeV.

Transverse mass (m_{T}) The transverse mass is calculated as

$$m_{\mathrm{T}} = \sqrt{2|\mathbf{p}_{\mathrm{T},1}||\mathbf{p}_{\mathrm{T},2}|(1-\cos(\Delta\phi))},$$

where $\Delta\phi$ is the angle between the particles with transverse momenta $\mathbf{p}_{\mathrm{T},1}$ and $\mathbf{p}_{\mathrm{T},2}$ in the transverse plane.

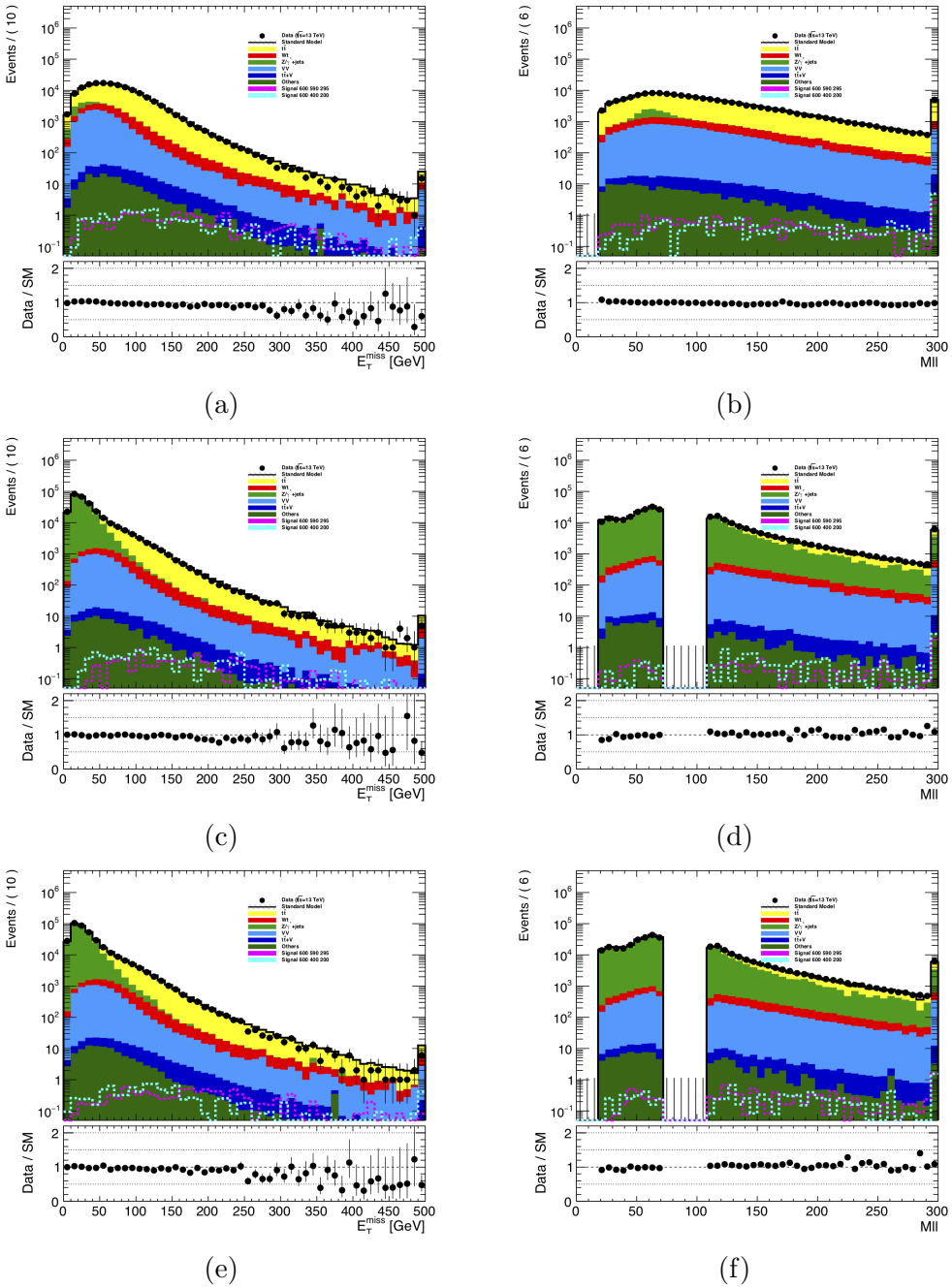

Figure 6.7: Distribution of $m_{\ell\ell}$ and $E_{\mathrm{T}}^{\mathrm{miss}}$ variables after preselection considering two opposite flavour leptons (a and b), two electrons (c and d) and two muons (e and f)

Stranverse mass (m_{T2}) The m_{T2} [108, 109] is an extension of the m_{T} variable when more than one particle in the final state is not seen by the detector. It is defined as follows:

$$m_{\mathrm{T2}}(\mathbf{p}_{\mathrm{T},1}, \mathbf{p}_{\mathrm{T},2}, \mathbf{q}_{\mathrm{T}}) = \min_{\mathbf{q}_{\mathrm{T},1}+\mathbf{q}_{\mathrm{T},2}=\mathbf{q}_{\mathrm{T}}} \{\max[\, m_{\mathrm{T}}(\mathbf{p}_{\mathrm{T},1}, \mathbf{q}_{\mathrm{T},1}), m_{\mathrm{T}}(\mathbf{p}_{\mathrm{T},2}, \mathbf{q}_{\mathrm{T},2})\,]\}\,,$$

where $\mathbf{p}_{\mathrm{T},1}$ and $\mathbf{p}_{\mathrm{T},2}$ are the transverse momenta of two observed objects, chosen depending on the characteristic of the event to be reconstructed. The minimization is operated on all the possible decompositions of $\mathbf{q}_{\mathrm{T},1}$ and $\mathbf{q}_{\mathrm{T},2}$ satisfying the condition $\mathbf{q}_{\mathrm{T},1} + \mathbf{q}_{\mathrm{T},2} = \mathbf{q}_{\mathrm{T}}$, being $\mathbf{q}_{\mathrm{T}} = \mathbf{p}_{\mathrm{T}}{}^{miss}$. In case of a WW dileptonic decay, and considering the two leptons as the observed objects, and the $E_{\mathrm{T}}^{\mathrm{miss}}$ only produced by the two neutrinos from the W decays, the m_{T2} variable is bounded from above at the W boson mass. In case some supplementary missing energy is present in the event, tails at higher m_{T2} are expected. The m_{T2} distribution for both data and background is shown in Fig. 6.8.

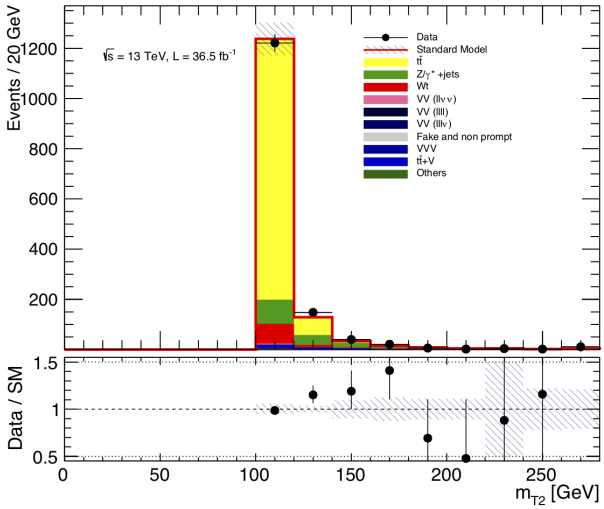

Figure 6.8: Stranverse mass (m_{T2}) distribution

$\mathbf{p}_{\mathrm{Tb}}^{\ell\ell}$ The $\mathbf{p}_{\mathrm{Tb}}^{\ell\ell}$ is defined as the opposite of the vector sum of all the transverse hadronic activity in the event.

$\Delta\phi_b$ It is the azimuthal angle between $\mathbf{P}_T^{miss}$ and $\mathbf{p}_{\mathrm{Tb}}^{\ell\ell}$. This variable is powerful to reject events in which the missing transverse momentum is aligned with the direction of jets, most probably due to a jet mismeasurement. $\Delta\phi_b$ distribution is shown in Fig. 6.9.

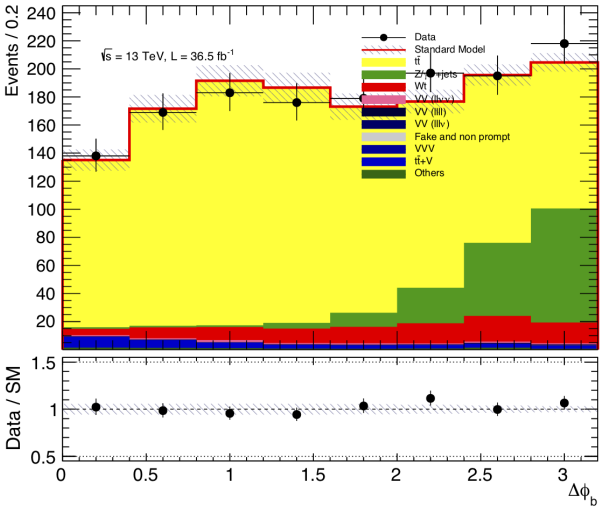

Figure 6.9: $\Delta\phi_b$ distribution

$\Delta\phi_{min}$ This variable is the smallest azimuthal angle between $\mathbf{P}_T^{miss}$ and the transverse momentum of a jet having at least a $p_T > 25$ GeV. As in the previous angular variable, also in this case it is useful to reject events with badly reconstructed $E_{\mathrm{T}}^{\mathrm{miss}}$. $\Delta\phi_{min}$ distribution, for both data and MC background processes, is reported in Fig. 6.10.

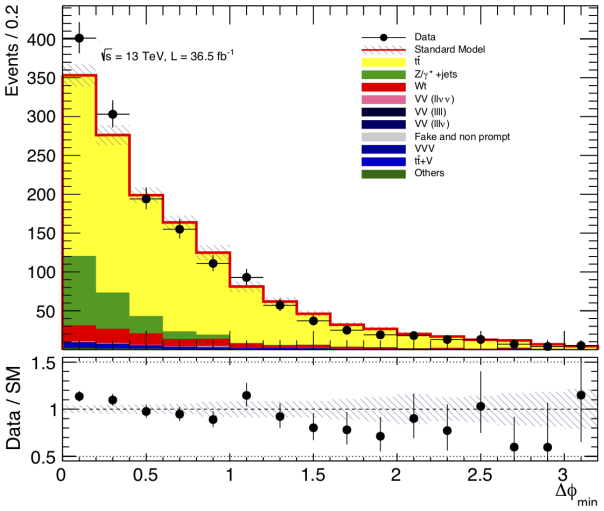

Figure 6.10: $\Delta\phi_{min}$ distribution

min $m_{b\ell}$ This variable is defined as the minimum invariant mass calculated between the leading b-jet and each of the two leptons. If the event topology includes top quarks decaying leptonically, as the targeted signature, this variable

is bounded from above at about 150 GeV. min $m_{b\ell}$ distribution is reported in Fig. 6.11.

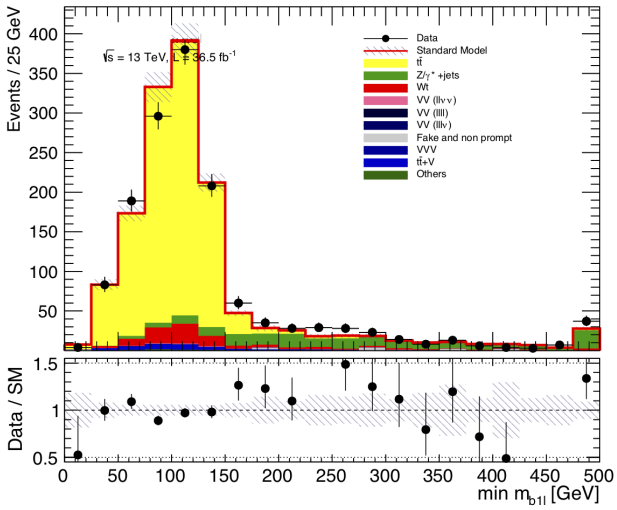

Figure 6.11: min $m_{b\ell}$ distribution

c_{em} It is a linear combination of m_{T2} and $E_{\mathrm{T}}^{\mathrm{miss}}$, defined as follows:

$$c_{em} = m_{\mathrm{T2}} + 0.2E_{\mathrm{T}}^{\mathrm{miss}}$$

This variable is the most relevant for the rejection of the main background process ($t\bar{t}$), while preserving a good fraction of the signal. The correlation between the m_{T2} and $E_{\mathrm{T}}^{\mathrm{miss}}$ can be seen in Fig. 6.12. In the plot (a) the bidimensional correlation in the case of the top background is reported, while on Figure (b) the case of a pseudoscalar signal (mass of the mediator equal to 100 GeV) is shown. The plots have been made after a preselection on the event as described previously and requiring one b-tag jet having a p_T of at least 30 GeV. c_{em} distribution for data and MC background processes is reported in Fig. 6.13.

6.8 Signal region definition

As it was already mentioned, the final state investigated involves two leptons, 2 b-tagged jets, and a considerable amount of $E_{\mathrm{T}}^{\mathrm{miss}}$ coming from SM neutrinos, and, possibly, dark matter particles. The first group of background processes goes under the category of the reducible backgrounds: those are Z+jets and dibosons, with moderate hadronic activity, $t\bar{t}$ and Wt production. In all these cases the $E_{\mathrm{T}}^{\mathrm{miss}}$ of the event comes from W decays, and therefore is kinetically bounded, or from a mismeasurement of jets, which could be reduced by means

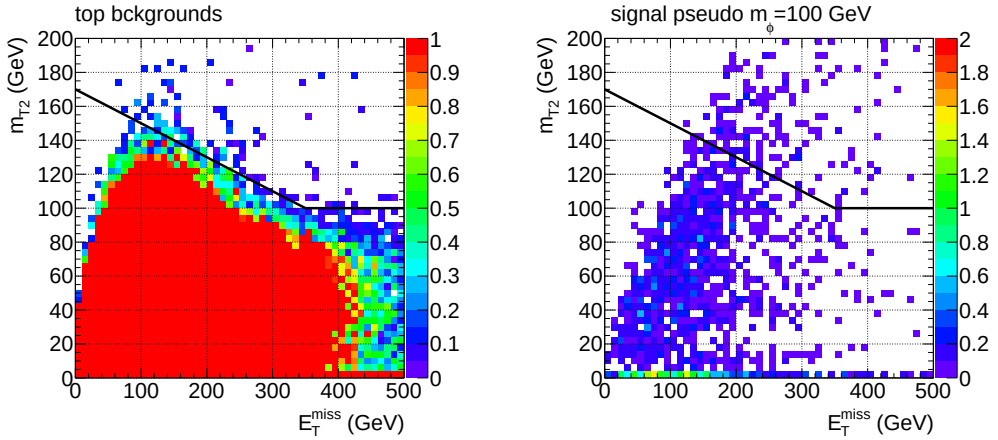

(a) (b)

Figure 6.12: The c_{em} variable to reject the $t\bar{t}$ background: a linear combination of $E_{\mathrm{T}}^{\mathrm{miss}}$ and m_{T2} allows to discard most of the background (a) while preserving the signal (b)

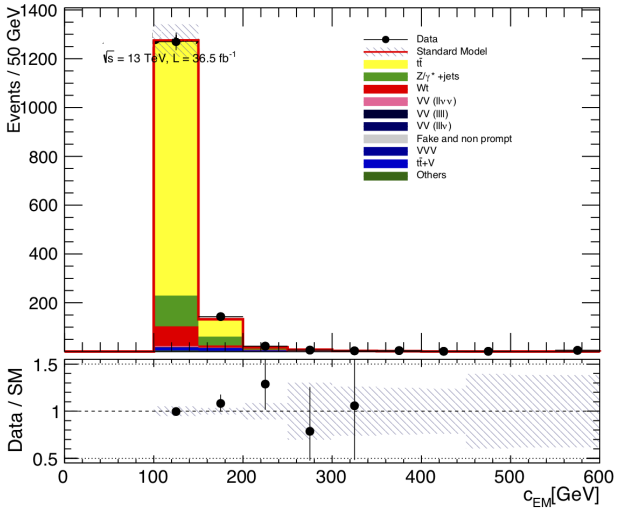

Figure 6.13: c_{em} distribution

of the angular observables. For backgrounds including Ws, the natural variable to be considered is the m_{T2}. As already observed this observable has a sharp bound for this type of processes at around 80 GeV. A cut at $m_{\mathrm{T2}} > 100$GeV would reduce considerably their contribution. On the other hand, target signal includes two top quarks, hence a selection on the min $m_{b\ell}$ variable is recommended to reduce the non-top background processes. A limit on min $m_{b\ell}$ of 170 GeV has been considered. As already observed, reducible background not including W decays should show, at high m_{T2}, a strong correlation between the direction of $E_{\mathrm{T}}^{\mathrm{miss}}$ and the hadronic activity. This can be seen looking at Fig.

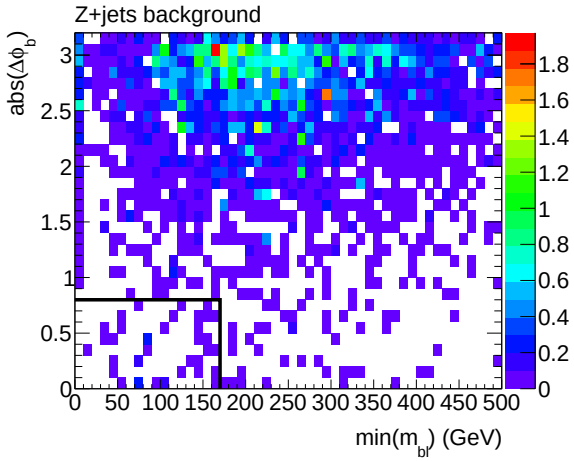

(a)

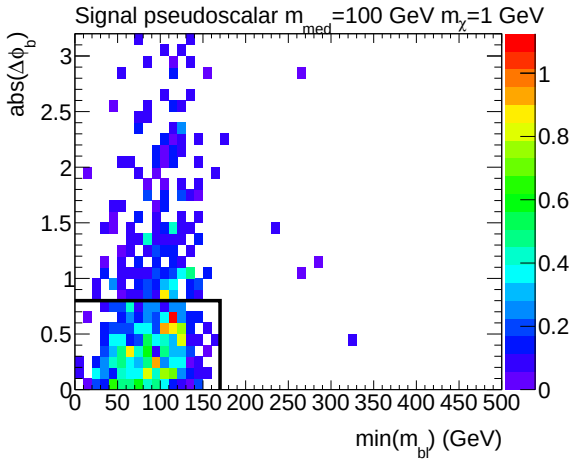

(b)

Figure 6.14: Distribution of $\Delta\phi_{\mathrm{b}}$ as a function of min $m_{b\ell}$ for Z+jets, and Pseudoscalar signal with mediator mass set at 100 GeV.

6.14 where the $\Delta\phi_b$ variable is reported as a function of min $m_{b\ell}$ for both the signal (pseudoscalar with mediator mass equals to 100 GeV) and the Z+jets background. A selection on the $\Delta\phi_b$ to be smaller than 0.8, as shown in the figures, allows to efficiently reject the Z background, without almost affecting the signal.

To target the signal, and to improve the discrimination of the $t\bar{t}$ background a further requirement on the c_{em} observable is required as already pointed out in Fig. 6.12. Events with $c_{em} > 170$ GeV are considered. In Table 6.2 a list of the selection operated for the signal region definition is report.

The adopted selection is found to have a good discrimination power on a wide range of masses of both scalar and pseudoscalar.

Var/Region	SR	
n_{lep}	2	
p_{T} lep 1, 2	$> 25, 20$ $m_{\ell\ell}$ DF	> 20
$m_{\ell\ell}$ SF	$[20, 71]$ or > 111 GeV	
m_{T2} [GeV]	>100	
c_{EM} [GeV]	>170	
min $m_{b\ell}$ [GeV]	<170	
$\Delta\phi_{\mathrm{b}}$	<0.8	
n_{b-jets} (p_{T} >30 GeV)	≥ 1	

Table 6.2: SR definition criteria.

6.9 Background estimation

In this section more details concerning the main background processes estimation are given, starting from the irreducible background, the $t\bar{t}Z$ process, and then the $t\bar{t}$. Two dedicated control regions have been defined to normalized the background to data. All the other minor processes are estimated via MC. The estimation of the contribution from fake and non prompt leptons is also briefly described.

6.9.1 $t\bar{t}Z$ background estimation

The $t\bar{t}Z$ process, with the Z boson decaying into neutrinos, invisible to the detectors, is expected to be the dominant background contribution to the SR, since it has the same final state as the signal, with a very similar event topology. One possible approach to the estimation of this background is to consider the $t\bar{t}Z$ process with four leptons in the final state, assuming, in this way, the decay of the Z boson into two visible leptons. Due to the very low branching fraction, with the available statistic, only a handful of events of this type is produced, and this type of channel cannot be used for the estimation. The second approach foresees to consider the $t\bar{t}Z$ process with three leptons in the final state, considering, in this way, the leptonic decay of the Z boson, one W decaying leptonically and one W decaying into hadrons. The difficulty, in this case, is that the event topology is not as the one targeted by the SR, and it is not possible to fully mimic the observables used for the signal region definition. The strategy can be summarized as follows:

- Define a pure selection of $t\bar{t}Z \rightarrow 3l$ events mimicking, when possible, the preselection used for the 2 leptons analysis and estimate by means of MC and data driven techniques the background processes

- Define, starting from the 3 leptons selection a dedicated control region populated by events that, at parton level, with undecayded $t\bar{t}$ and Z boson would kinematically populate also the 2 leptons SR. This aspect

is of extreme importance: the predictive power of the CR is based on its superposition with the 2 leptons SR

- The number of expected and observed events in the CR are used in the background fitting procedure

Selection of $t\bar{t}Z$ with 3 leptons final state

The selection used in the three leptons selection is summarized in Table 6.3. Exactly three leptons are required, with at least a couple being of the same flavour, but opposite sign, to be compatible with the Z decay. The same requirement on the lepton momenta is applied: 25 GeV for the leading and 20 GeV for the other two. The event is accepted if two OS-SF (opposite sign, same flavour) leptons are found to be compatible with Z boson decay. The invariant masses of all the OS-SF pairs in the event are calculated and the event is accepted if at least in one case it lies within 20 GeV from the Z boson mass peak. If more than one couple satisfy the condition, the closest to the Z peak is considered.

$t\bar{t}Z$ sample selection	
N_{lep}	3
	at least 1 OS-SF pair
$p_T(\ell_1)$	>25 GeV
$p_T(\ell_2, \ell_3)$	>20 GeV
Leptonic Z decay	81 GeV$<m_{\ell\ell}<$101 GeV
n_{b-jets}	> 1 and $n_{jets} > 2$
	$== 1$ and $n_{jets} > 3$
m_{bl}	< 170 GeV

Table 6.3: Definition criteria for 3ℓ CR

The selection has itself a SM background, consisting of all process with three leptons and jet activity. A requirement of having at least 3 jets, one of which b-tagged is added. Among all the configurations allowed by this requirement, the one having exactly 3 jets one of which b-tagged is vetoed, due to the large contribution from diboson processes. At last, a further selection on the minimum invariant mass calculated from the remaining lepton (not coming from the Z decay) and all the b-tag jets is added, to be lower than 170 GeV. This selection is justified by the fact that a top quark has decayed into a W boson and a b-quark.

CR definition

As already remarked in the general strategy, the main difficulty in this background estimation is that the event topology in the 3 leptons case is different

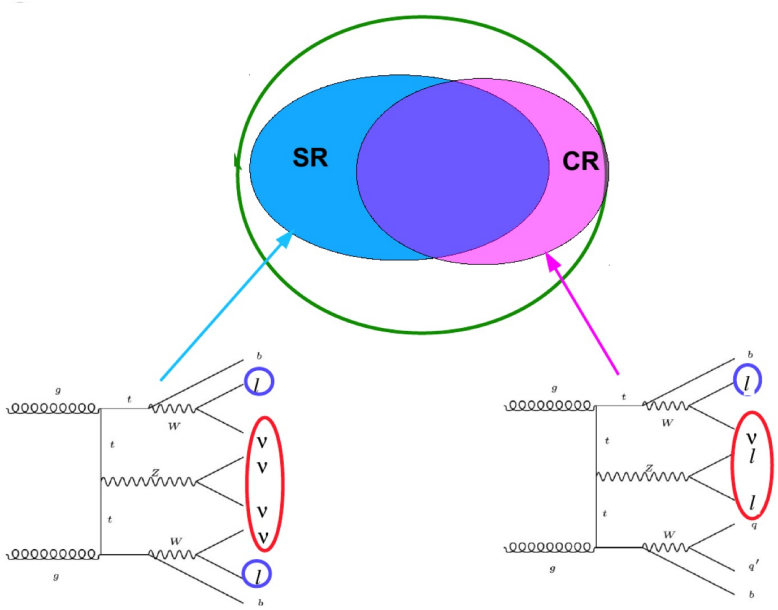

Figure 6.15: Graphical representation of the $ttZ \to \nu\nu$ background estimation strategy. The 2-lepton signal region is populated by events having high m_{T2}, built by using the 4 neutrinos and the 2 leptons from the W decays. A CR is defined in the 3-lepton sample to mimic as much as possible the SR. A m_{T2}-like variable has been defined in the 3 leptons sample, taking the two leptons from the Z decay, adding them to $E_{\mathrm{T}}^{\mathrm{miss}}$ and calculating the m_T between E_T^{mcorr} and the remaining lepton.

with respect to the one targeted in the SR and it is impossible to define variables exactly mimicking the ones used in the 2 leptons case. The main discriminant variable was the m_{T2}, made with the 2 leptons and the $E_{\mathrm{T}}^{\mathrm{miss}}$ from, at least in the SM case, four neutrinos. The first step to imitate m_{T2} has been to add the two leptons reconstructed as decaying from the Z boson to the $E_{\mathrm{T}}^{\mathrm{miss}}$, creating the so-called E_T^{mcorr}. At this point the nearest variable to the m_{T2} is the m_T variable built using the remaining lepton and the E_T^{mcorr}.

The strategy is shown in Fig. 6.15. The c_{em}^{corr} observables, nearest approximation to the c_{em} variable achievable with a 3 leptons sample, can be therefore defined as: $c_{em}^{corr} = m_T^{corr} + 0.2E_T^{mcorr}$. The CR has been defined requiring c_{em}^{corr} to be greater than 120 GeV and E_T^{mcorr} greater than 80 GeV.

Plots showing the Data/Monte Carlo comparison in the thus defined CR are shown in Figure 6.16.

CR-SR overal estimation

The success of the 3 leptons approach is based on the overlap between the CR and SR. In other words how the 3 leptons selection is kinematically close to the SR and how many of those events, with undecayed $t\bar{t}$ would populate the

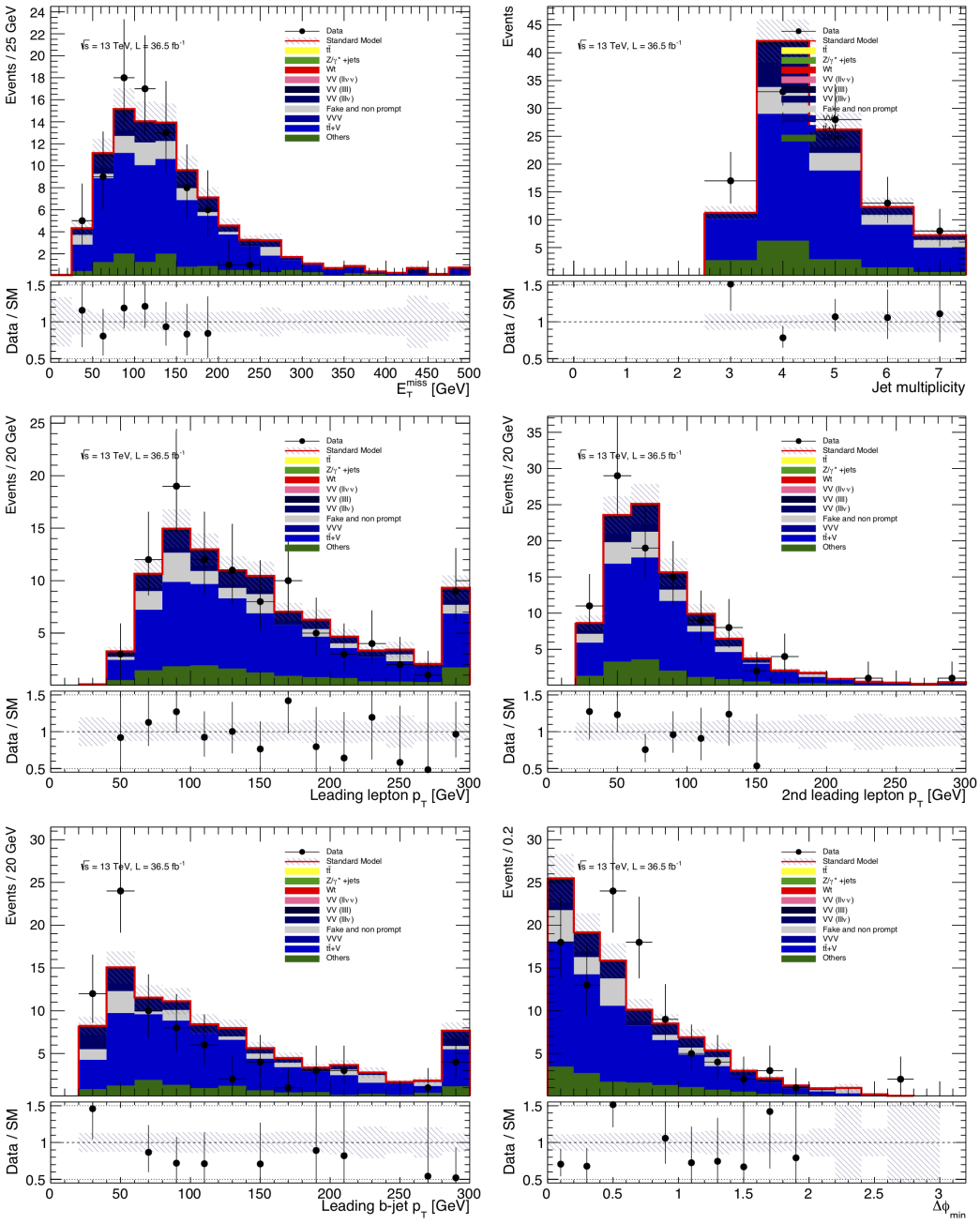

Figure 6.16: Distribution of some key variables in the $t\bar{t}Z$ CR. The band represents the total statistical uncertainty.

SR as well. To perform this evaluation $t\bar{t}Z \to \nu\nu$ MC events at parton level have been used. The usual $E_{\mathrm{T}}^{\mathrm{miss}}$, m_{T2} and c_{em} have been computed by using the information from the neutrinos. c_{em} distribution is shown in Fig. 6.17 in blue. Using the same sample the E_T^{mcorr} and c_{em}^{corr} are calculated and a cut of 120 GeV(as in the CR) is applied. The c_{em} variable is then recalculated for the

event passing the selection and it is shown in the same figure (red line). The high c_{em} region is completely included in the CR, and around 30% of the CR has a c_{em} higher than 120 GeV. If an additional cut on the E_T^{mcorr} is added, this percentage increases up to 40%. This overlap between the two regions has been considered to be satisfactory and enough to estimate the $t\bar{t}Z$ background by means of a 3-lepton CR.

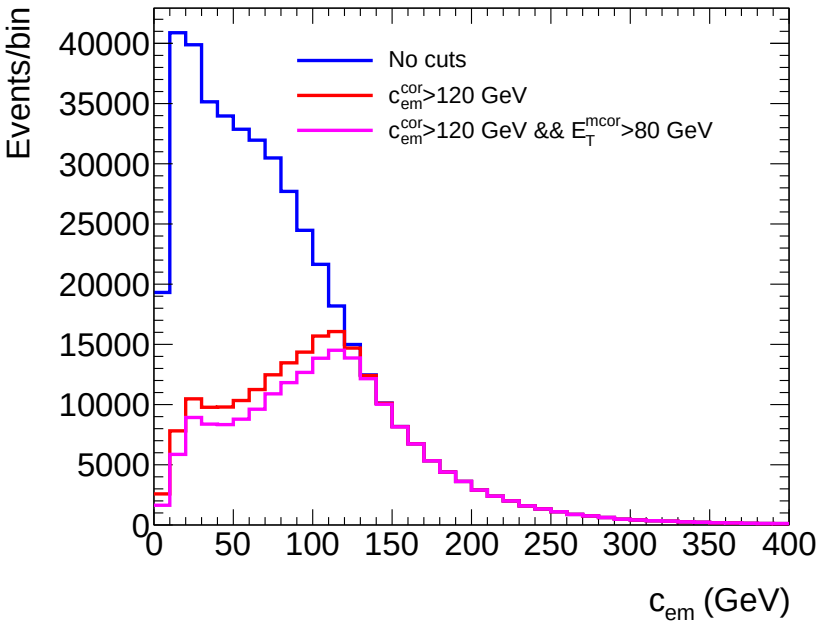

Figure 6.17: Distribution of the c_{em} obtained from $ttZ \to \nu\nu$ truth sample, without cuts (blue line) after the cut on c_{em}^{corr} (red line), and on $c_{em}^{corr} + E_T^{mcorr}$ (pink line) described in the text.

6.9.2 $t\bar{t}$ background estimation

A second CR has been defined to normalize the $t\bar{t}$ process. In this case the same selection operated in the SR has been used with the exception of the c_{em} cut, which has been inverted in order to guarantee the orthogonality with the signal region. Summary of the selection is given in Table 6.4.

The most relevant discriminating variables are shown in Fig. 6.18,6.19 and 6.20. A good agreement is visible.

Validation of $t\bar{t}$ the background estimation

A validation region has been developed to check the $t\bar{t}$ background estimated in the CR. As for the CR, validation regions (VR) need to be kinetically close

Var/Region	CRT
m_{T2} [GeV]	>100
c_{EM} [GeV]	<150
min $m_{b\ell}$ [GeV]	<170
$\Delta\phi_{\mathrm{b}}$	<0.8
Num. $B-$tagged jets	≥ 1

Table 6.4: Definition criteria of CRT.

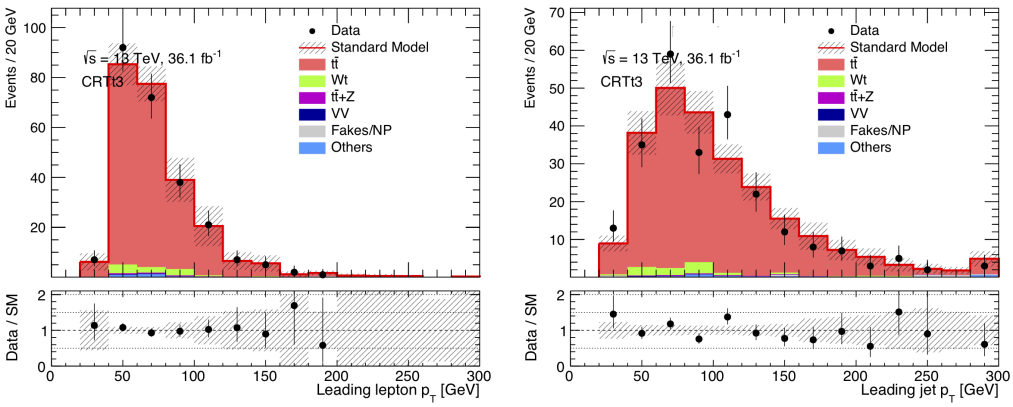

Figure 6.18: p_{T} distribution of leading lepton and jet respectively

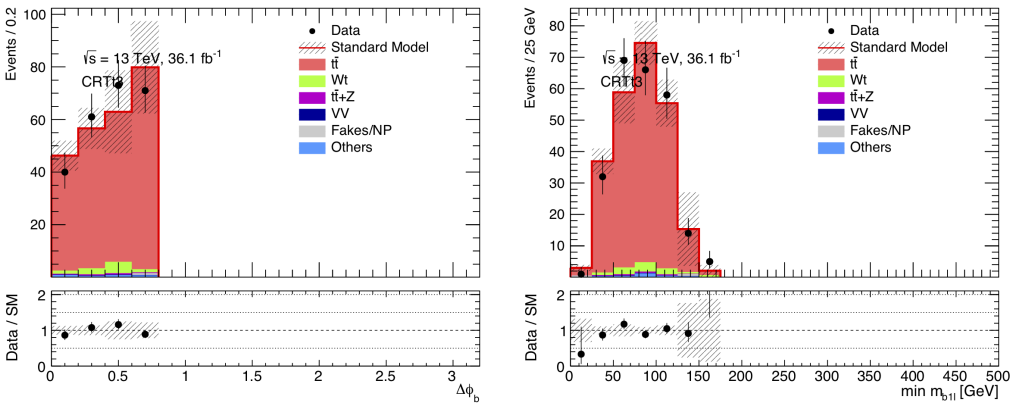

Figure 6.19: $\Delta\phi_{\mathrm{b}}$ distribution (left) and min $m_{b\ell}$ (right) in events passing the CRT requirements.

to the SR. The exact selection operated is reported in Table 6.5. The orthogonality with the SR is guaranteed by the $\Delta\phi_b$ selection. The distributions of the most relevant variables (c_{EM} and $E_{\mathrm{T}}^{\mathrm{miss}}$) are shown in Fig. 6.21.

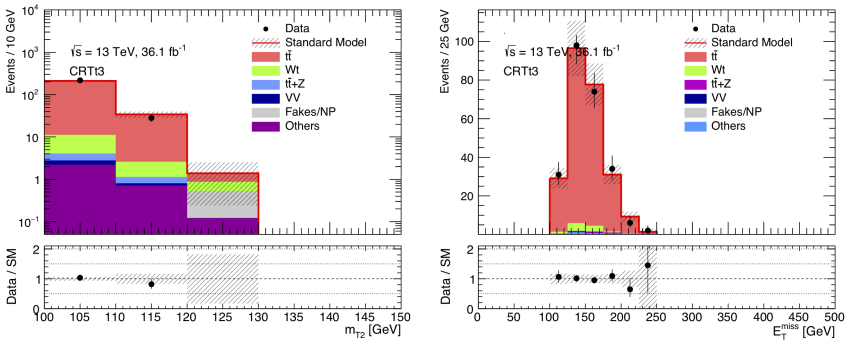

Figure 6.20: m_{T2} distribution (left), and $E_{\mathrm{T}}^{\mathrm{miss}}$ (right) in events passing the CRT requirements.

Var/Region	VRB
m_{T2} [GeV]	>100
c_{EM} [GeV]	>150
min $m_{b\ell}$ [GeV]	<170
$\Delta\phi_{\mathrm{b}}$	>1.5
Num. $B-$tagged jets	≥ 1

Table 6.5: Definition criteria of the analysis VR.

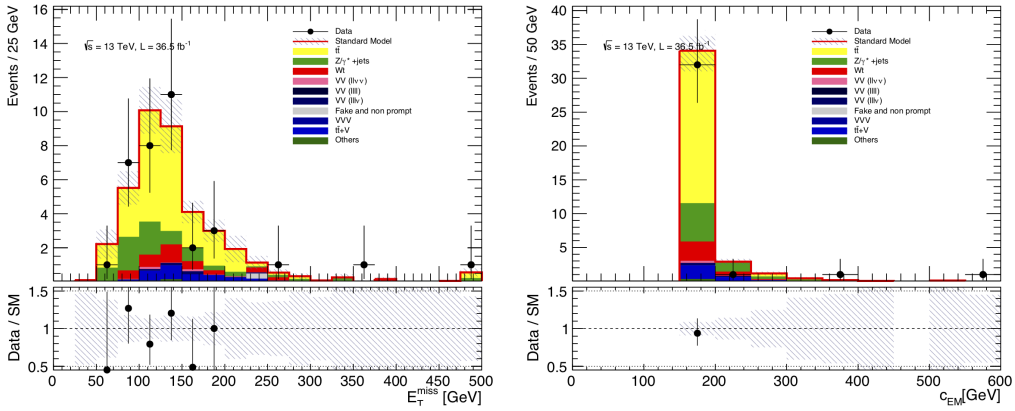

Figure 6.21: $E_{\mathrm{T}}^{\mathrm{miss}}$ distribution (left) and c_{EM} (right) in events passing the VR requirements.

6.9.3 Fake and non prompt leptons

A not-negligible background processes contributing to the SR comes from semileptonic $t\bar{t}$ decay and W+jets where one lepton is prompt and the other one is misidentified. The procedure to estimate such background sources, follows a data driven technique called *matrix method* [110]. It is based on the event count in the signal region considering different leptons selection criteria.

In our case the two selection criteria considered are the *tight* and *loose*. The number of events passing the tight and loose selection criteria can be expressed as:

$$N^{loose} = N^{loose}_{real} + N^{loose}_{fake} \tag{6.6}$$

$$N^{tight} = rN^{loose}_{real} + fN^{loose}_{fake} \tag{6.7}$$

where r and f are the fractions of events in the loose selection to pass the tight one as well. If r and f are obtained it is possible to estimated the number of fake leptons simply inverting the previous equations. This is done measuring those parameters in control samples enriched in either prompt or non-prompt leptons. More insights on the method are described in Ref. [111].

6.10 Results

In this section, before moving to the results of the anlaysis, a brief description of the mathematical approach to the interpretation of the results is given. For a more complete discussion on the topic refer to Ref. [112].

6.10.1 Statistical interpretation of the results

As already mentioned in the previous section, CRs and VRs are used to constrain the MC background estimation to the data in order to use this information in the signal region. Mathematically the result of the analysis is based on a statistic test on a likelihood function, defined as product of the Poisson distributions of the event counts in the CRs and SRs and of any additional distribution representing, for example, systematic uncertainties, as follows:

$$\mathcal{L} = (n, \theta^0 | \mu_{sig}, b, \theta) = \mathcal{P}_{SR} * P_{CR} * C_{syst} = \tag{6.8}$$

$$= \mathcal{P}(n_s \ \lambda_s(\mu_{sig}, b, \theta)) \times \prod_{i \in CRs} \mathcal{P}(n_i \ \lambda_i(\mu_{sig}, b, \theta)) \times \mathcal{C}_{syst}(\theta^0, \theta), \tag{6.9}$$

where $\mathcal{P}$ represents the Poisson measurement of n_i and n_s events in the CRs and SRs respectively. The expectation values λ_s and λ_i are function of the background process estimations, including the normalization (transfer factor) obtained with a background only fit in the CRs and also of the signal strength μ_{sig}. If μ_{sig} is equal to 0, the signal component is not considered. $\mathcal{C}_{syst}$ is the product of the probability corresponding to the systematic uncertainties rising from the detector simulation and event generation. Those additional contributions are usually Gaussian, except in the case of the statistical uncertainty, which is treated as Poisson distribution.
In a search for new physics, the null hypothesis, including only the SM background, is tested against the $\mathcal{H}_1$ hypothesis, which includes both background and the signal characterized by a signal strength (μ_s). A profile log ratio is

then considered, defined as the following:

$$q_{\mu_{sig}} = -2log\left(\frac{\mathcal{L}(\mu_{sig}, \hat{\hat{\theta}})}{\mathcal{L}(\hat{\mu}_{sig}, \hat{\theta})}\right), \tag{6.10}$$

where $\hat{\mu}_{sig}$ and $\hat{\theta}$ maximize the likelihood function and $\hat{\hat{\theta}}$ maximizes the likelihood function for a specific value of μ. The $p-value$ can be calculated considering the probability density distribution of the test statistic. Usually data are considered incompatible with the null hypothesis ($\mu = 0$) if

$$p_0 < 2.87 \cdot 10^{-7} \tag{6.11}$$

which corresponds to the 5σ limit needed to claim a discovery. Technically, all the minimization steps are performed by the statical framework HistFitter [113].

6.10.2 Systematic uncertainties

Experimental and theoretical uncertainties are taken into account in the analysis as systematics. The experimental uncertainties are estimated by means of calibrations of leptons, muons, jets, $E_{\mathrm{T}}^{\mathrm{miss}}$ and soft terms. The detector related most relevant are the jet energy scale and resolution, derived depending on the jet flavour composition and pile-up, as a function of η and p_T as described in Ref. [105]. Since the signal region largely relies on a $E_{\mathrm{T}}^{\mathrm{miss}}$ selection, the related uncertainty is expected to have a not-negligible contribution. It is estimated by propagating the uncertainties related to energy and momentum reconstruction of leptons, muons, and jets as described in Ref. [107].
Concerning the theoretical uncertainties, the $t\bar{t}$ process has been estimated by varying the initial and final state radiation, and the renormalisation and factorisation scale as described in Ref. [114]. Different generators and parton shower predictions have been also considered to account for related uncertainties. Finally an additional uncertainty is considered in the fake lepton estimation, deriving from the potentially different composition of the SR with respect to the CR used to background estimation. For the SR an overall systematic uncertainty of 28% has been estimated, mainly dominated (18%) from the MC statical uncertainty, followed by $E_{\mathrm{T}}^{\mathrm{miss}}$ and theoretical $t\bar{t}$ uncertainties.

6.10.3 Fit results

The fit of the two CRs to estimated $t\bar{t}$ and $t\bar{t}Z$ processes provided the following normalization factors, with all systematic uncertainties included:

$\mu_{t\bar{t}} = 1.17 \pm 0.08$

$\mu_{t\bar{t}Z} = 0.79 \pm 0.19$

The observed events in the data and the expected background rate in the SR after the background fit are shown in Table 6.6. The background estimation is compatible with the observed data and limits are derived both on the model and on a generic BSM signal. Figure 6.22 shows the most relevant distribution for the SR, after the background fit.

	SR
Observed events	18
Fitted bkg events	15.17 ± 4.26
$t\bar{t}$ events	4.48 ± 2.54
$t\bar{t} + Z$ events	4.40 ± 1.85
Wt events	$0.33^{+0.53}_{-0.33}$
Z/γ^*+ jets events	0.28 ± 0.12
VV events	0.61 ± 0.25
$t\bar{t} + W$ events	1.56 ± 0.36
Fake and non prompt events	2.65 ± 1.32
Others events	0.85 ± 0.45

Table 6.6: Background fit results for the SR for an integrated luminosity of 36.1 fb^{-1}. Combined statistical and systematic uncertainties are shown. Uncertainties on the predicted background event yields are quoted as symmetric except where the negative error reaches down to zero predicted events, in which case the negative error is truncated.

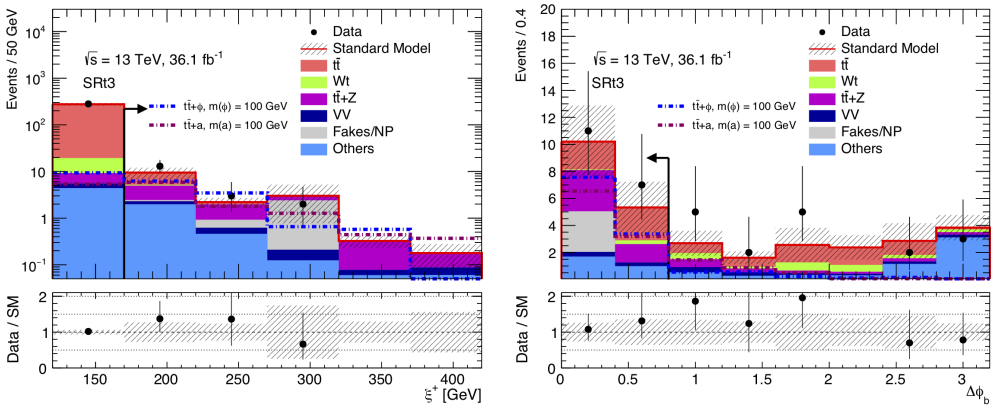

Figure 6.22: Distribution of c_{em} (left), $\Delta\phi_{\text{b}}$ (right) for events passing all the SR selections except the variable shown itself.

The model independent limits are obtained at the 95% CL, considering the product $\sigma \times \epsilon \times \mathcal{A}$, where σ is the non-SM cross section, ϵ the selection

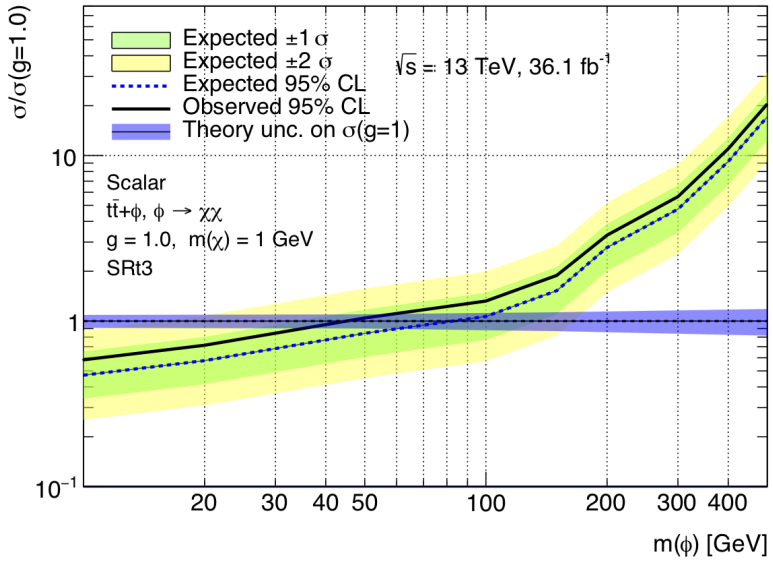

Figure 6.23: Model dependent limit for the scalar mediator models as a function of the mediator mass and with a fixed DM mass of 1 GeV. All systematic uncertainties and NLO k-factors are included.

efficiency, and $\mathcal{A}$ the acceptance of kinematic cuts. Limits obtained are shown in Table 6.7.

Table 6.7: Left to right: the visible cross-section upper limit, 95% CL observed and expected upper limits on the number of non-SM events ($S^{95}_{\text{exp.(obs.)}}$) and the p-value of the background only hypothesis. Numbers are calculated using toy MC pseudo-experiments.

Signal Region	$\langle\epsilon\sigma\rangle^{95}_{\text{obs.}}$ [fb]	$S^{95}_{\text{obs.}}$	$S^{95}_{\text{exp.}}$	$p(s=0)$
SR	0.44	15.9	$13.1^{+5.3}_{-1.8}$	0.33

Considering, on the other hand, the simplified dark matter model targeted by the analysis, limits have been provided as a function of the mediator mass m_a and m_ϕ for a 1GeV dark matter particle and are shown in Fig. 6.23 and 6.24. Similar limits are also derived as a function of the dark matter mass at fixed mediator masses, both scalar and pseudoscalar (Figure 6.25 and 6.26).

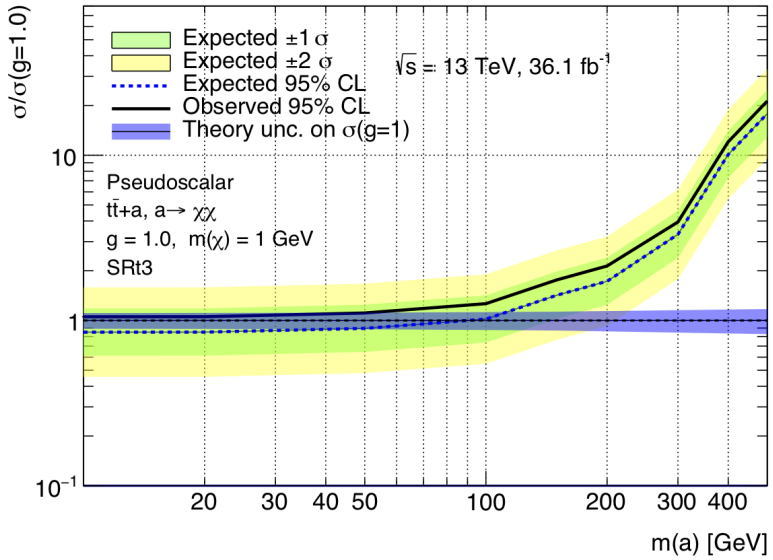

Figure 6.24: Model dependent limit for the pseudoscalar mediator models as a function of the mediator mass and with a fixed DM mass of 1 GeV. All systematic uncertainties and NLO k-factors are included.

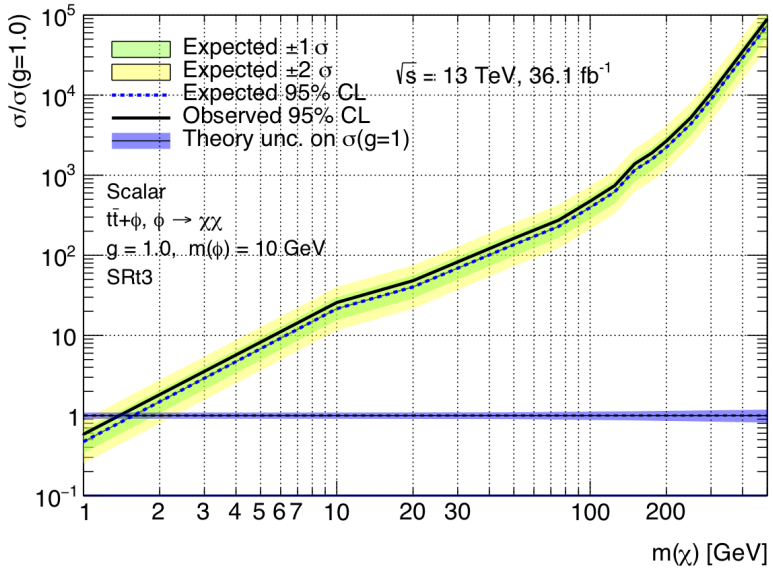

Figure 6.25: Model dependent limit for the scalar mediator models as a function of the DM mass and with a fixed mediator mass of 10 GeV. All systematic uncertainties and NLO k-factors are included.

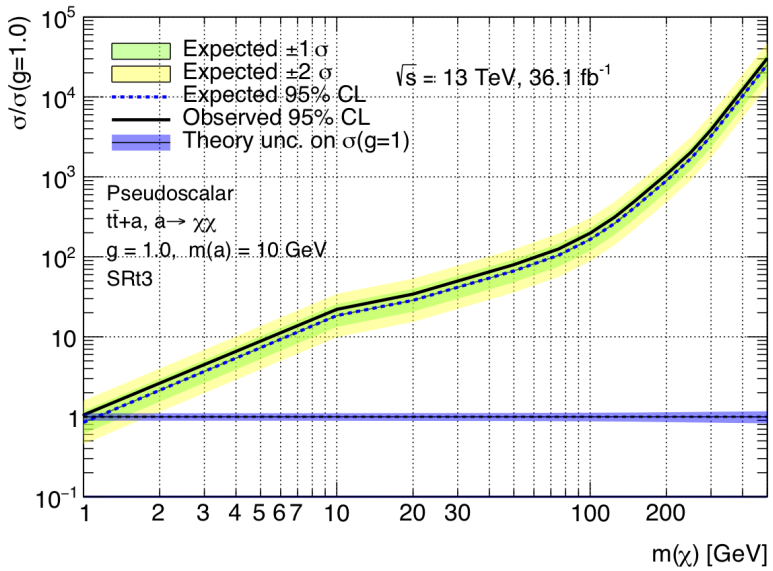

Figure 6.26: Model dependent limit for the pseudoscalar mediator models as a function of the DM mass mass and with a fixed mediator mass of 10 GeV. All systematic uncertainties and NLO k-factors are included.

6.11 Recasting of the results in a Two-Higgs-Doublet Model

A natural extension of the simplified model described above is to consider the mixing of the Higgs boson with the mediator. A possible way to accommodate the stringent Higgs physics constraints is to add a second Higgs doublet [115]. In this way the couplings to SM fermions are obtained by mixing with the second doublet. After electroweak symmetry breaking, five physical Higgs bosons are obtained, two CP-even state h and H, one CP-odd state A and two charged Higgs ($H^{\pm}$). The model foresees 15 free parameters, many of them constrained by EM precision measurement of the Higgs boson. Only 5 free parameters remain, m_a, m_A, m_H, $\tan\beta$ and $\sin\theta$, where a is the pseudoscalar mediator. The parameter $\sin\theta$ is the mixing angle between the CP-odd state A and the pseudoscalar mediator a, while $\tan\beta$ is the ratio between the vacuum expectation values of the two doublets. The searches which are expected to be sensitive to the model are those having $E_{\mathrm{T}}^{\mathrm{miss}}$ and Z, h, jet or two top (as the analysis previously presented) or bottom quarks in the final state. To map the exclusion limits in the 2HDMa model, it is possible to start from the excluded cross section obtained in the context of the DM simplified analysis for each value of m(a) according to the following formula:

$$\sigma_{exc}(2HDMa) = \sigma_{exc}(DMSIMP) \times \frac{\epsilon(DMSIMP) \times Acc(DMSIMP)}{\epsilon(2HDMa) \times Acc(2HDMa)}, \tag{6.12}$$

once the analysis acceptance is known. ϵ is the analysis efficiency and it is assumed to be the same for both the models, being due to the cuts defining the final state topology. The acceptance is, on the other hand, model dependent. It could be noticed, however, that for the 2HDMa model the dominant process of dark matter production in association with top quarks is $gg \to t\bar{t}a \to t\bar{t}\chi\bar{\chi}$, which is exactly the same of the simplified model. If this is confirmed to be the only contribution to the dark matter production also the acceptance of the two analyses is the same and the excluded cross section depends only on the production cross section. To prove the previous hypothesis a study at parton level of the process $gg \to t\bar{t}\chi\bar{\chi}$ is performed in the context of the two models. In both the models m(a) has been set to 150 and 300 GeV. The masses of the Higgs bosons of the 2HDMa model have been set to m(h) = 125 GeV and m(A) = m($H^{\pm}$) = m(H) = 750 GeV. In Figure 6.27 a comparison of the invariant mass of the dark matter pair is shown for both the models, for both choices of the m(a). In both cases a large discrepancy is observed due to the contribution coming from the pseudoscalar A and from the mixing between a and A. The relative contribution of the heavy pseudoscalar A depends on the choice of the parameters and a strategy is needed to handle correctly the rescaling.
A further comparison is performed, still at parton level, reducing the contributing from A, by selecting only events having a dark matter invariant mass close

to the a peak. In Figure 6.28 the $E_{\mathrm{T}}^{\mathrm{miss}}$ and m_{T2} distributions are shown for both models. The observed agreement is very good, meaning that if only the contribution from a is considered the kinematic of the two models is the same.

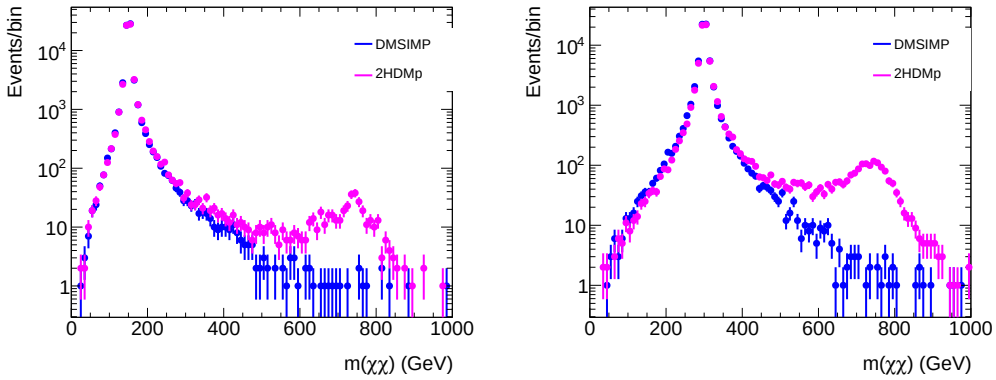

Figure 6.27: Invariant mass of the dark matter pair for both models when m(a)=150 GeV (a) and m(a)=300 GeV are used

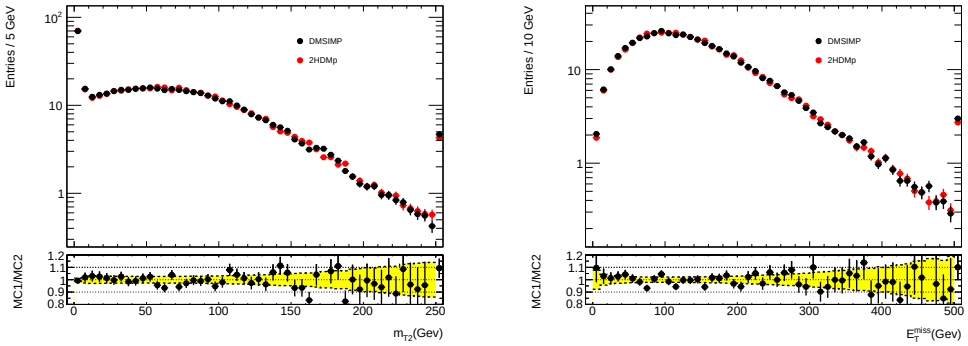

Figure 6.28: Comparison of the distributions of the variables M_{T2}, E_T^{miss} for the $DMSIMP$ model (black points) and $2HDMa$ model (red points). The distributions are obtained for $m(a) = 150$ GeV, and the $2HDMa$ distributions contain events passing the $m(\chi\chi) < 200$ GeVrequirement.

A possible approach for a correct evaluation of the analysis acceptance for the 2HDMa model is to consider the independent contribution due to a, having mass m(a), and A, characterized by mass m(A), weighted by the respective cross-sections ($\sigma(a)$ and $\sigma(A)$) according to following formula:

$$Acc_{2HDMa}(m(A), m(a)) = \frac{\sigma_a \times Acc_{DMSIMP}(m(a)) + \sigma_A \times Acc_{DMSIMP}(m(A))}{\sigma_a + \sigma_A}, \tag{6.13}$$

$$\epsilon_{2HDMa}(m(A), m(a)) = \frac{\sigma_a \times \epsilon_{DMSIMP}(m(a)) + \sigma_A \times \epsilon_{DMSIMP}(m(A))}{\sigma_a + \sigma_A}. \tag{6.14}$$

Figure 6.29 and 6.30 show the acceptance as a function of $\tan\beta$ and $\sin\theta$ in case of the DM simplified model considering only the contribution from a (grey band), the 2HDMa model (black points) and the simplified model where both a and A are taken into account (red band). The masses of A and a have been set to 600 and 150 GeV respectively. The comparison has been performed on several selections related to the process $gg \to t\bar{t}\chi\bar{\chi}$ with top quarks decaying hadronically and dileptonically [116], or decaying into a final state characterized by a single lepton [117]. The agreement is good and the strategy is proved to work in the space of the parameters relevant for this analysis. A further signature that could benefit of the recasting is the $gg \to b\bar{b}\chi\bar{\chi}$, also described in Ref. [116]. In this case, however, due to the choice of the 2HDMa parameters, the contribution due to A has been found to be negligible and it can be neglected.

The results of the recasting according to the Formula 6.12, providing limits in the $\tan\beta$-M_a bidimensional space, are shown in Fig. 6.31 for the $t\bar{t}\chi\bar{\chi}$ channel where the analysis providing the best expected limit (0, 1, 2 leptons) is taken into account for each single signal point. For what concerns the $b\bar{b}\chi\bar{\chi}$ no sensitivity has been obtained for the chosen set of parameters.

Limits as a function of $\sin\theta$ for different values of M_a, 200 and 350 GeV respectively, have been derived and shown in Fig 6.32 (200 GeV) and in Fig. 6.33 (350 GeV). As stated in the exclusion plots, the value of $\tan\beta$ has been chosen to enhance the sensitivity of the analysis. Finally, despite no dependence from the dark matter mass is expected, limits as a function of the dark matter mass ($m(\chi)$) are shown in Fig. 6.34.

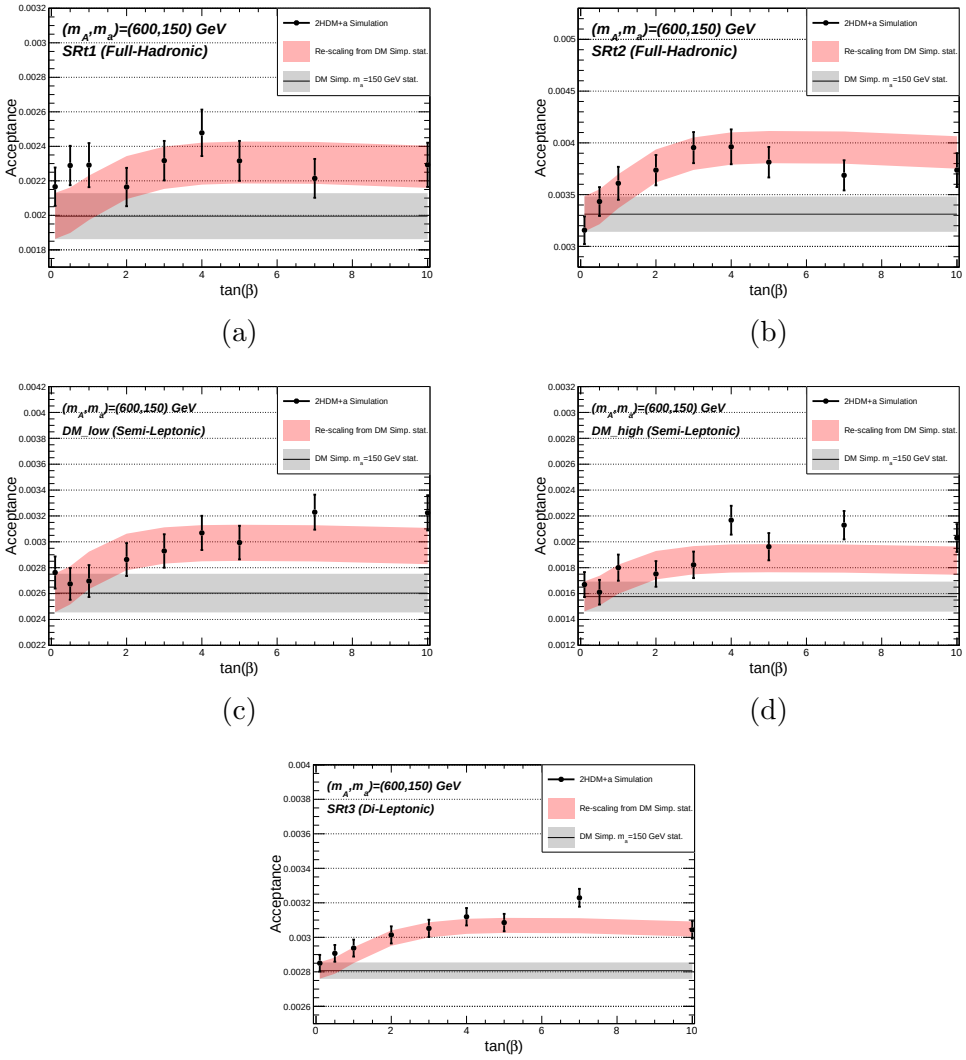

Figure 6.29: Comparison between $2HDMa$ and simplified model acceptances at parton level, before and after the reweighing. In (a) and (b) the $t\bar{t}\chi\bar{\chi}$ with top quark decaying hadronically case is shown, for two SRs respectively. Figures (c) and (d) show the $t\bar{t}\chi\bar{\chi}$ 1 lepton analysis, for the two SRs. Finally, figure (c) shows the $t\bar{t}\chi\bar{\chi}$ channel into 2 leptons case. Acceptance are shown as a function of $\tan\beta$

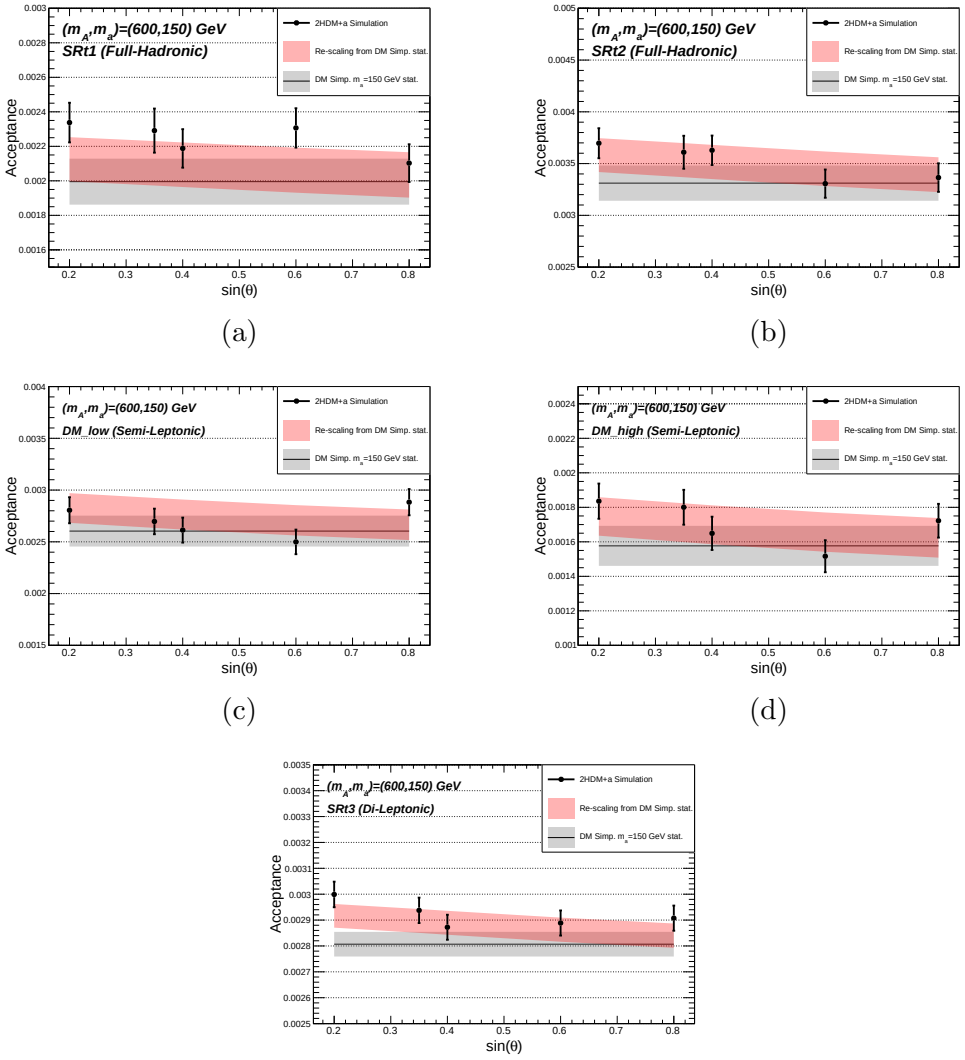

Figure 6.30: Comparison between $2HDMa$ and simplified model acceptances at parton level, before and after the reweighing. In (a) and (b) the $t\bar{t}\chi\bar{\chi}$ with top quark decaying hadronically case is shown, for the two SRs respectively. Figures (c) and (d) show the $t\bar{t}\chi\bar{\chi}$ 1 lepton analysis, for the two SRs. Finally, figure (c) shows the $t\bar{t}\chi\bar{\chi}$ into 2 leptons case. Acceptance are shown as a function of $\sin\theta$

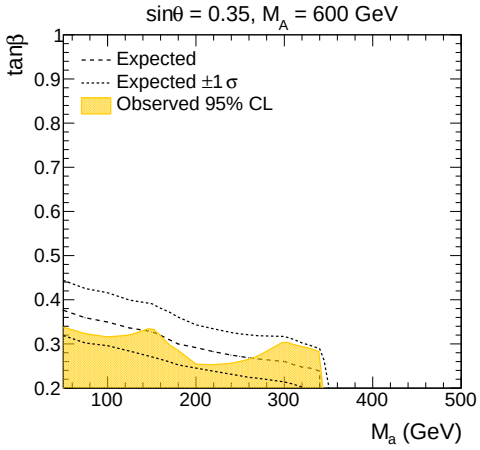

Figure 6.31: $t\bar{t}\chi\bar{\chi}$ recasting limit results obtained taking the best expected SR for each signal point in the plane defined by m(a) and $\tan\beta$.

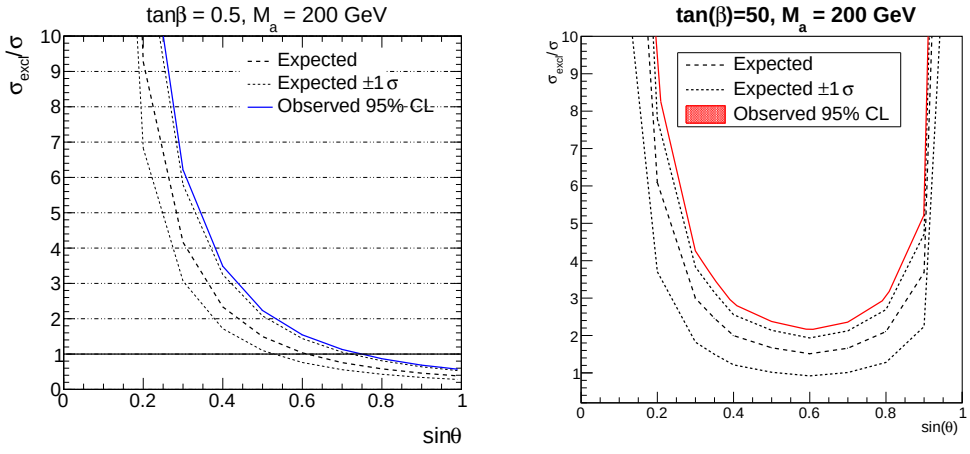

(a) (b)

Figure 6.32: Interpretation of the results for the $t\bar{t}\chi\bar{\chi}$ final state (left) and the $b\bar{b}\chi\bar{\chi}$ final state (right) as a function of $\sin\theta$ for $M_a = 200$ GeV. For the $t\bar{t}\chi\bar{\chi}$ final state the signal region providing the best expected sensitivity is used

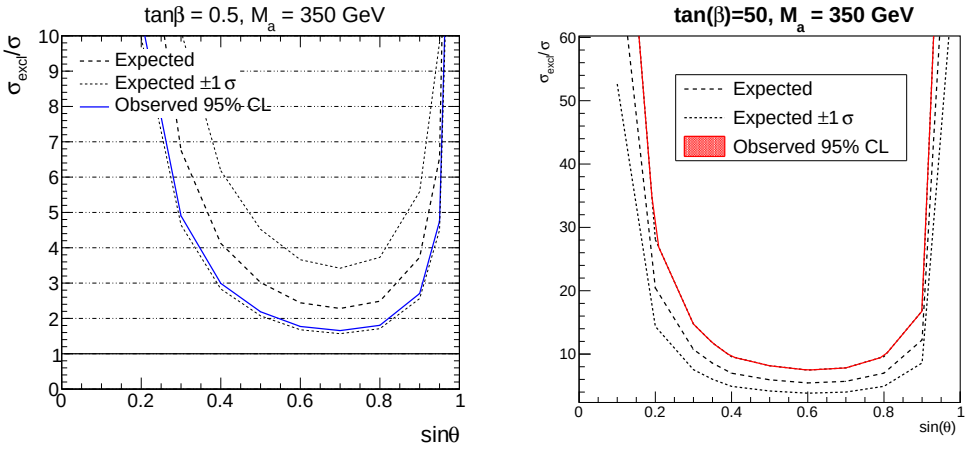

(a) (b)

Figure 6.33: Interpretation of the results for the $t\bar{t}\chi\bar{\chi}$ final state (left) and the $b\bar{b}\chi\bar{\chi}$ final state (right) as a function of $\sin\theta$ for $M_a = 350$ GeV. For the $t\bar{t}\chi\bar{\chi}$ final state the signal region providing the best expected sensitivity is used

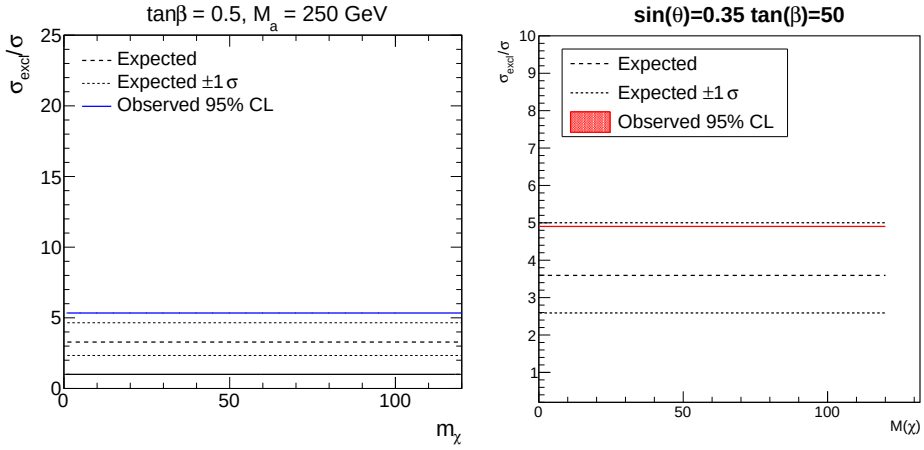

Figure 6.34: Interpretation of the results for the $t\bar{t}\chi\bar{\chi}$ final state (left) and the $b\bar{b}\chi\bar{\chi}$ final state (right) as a function the dark matter mass. For the $t\bar{t}\chi\bar{\chi}$ final state the signal region providing the best expected sensitivity is used .

6.12 Conclusion

The present analysis has investigated dark matter production in association with top quarks based on a Simplified Model. The analysis used 36.1 fb^{-1} of data from pp collisions at 13 TeV. Data has been found to be compatible with the SM expectations, leading to exclusion limits both model independent and dependent. In particular limits on the signal strength have been set on the DM and mediator masses for a coupling $g = 1$. Signal strength equal to 1 has been excluded for mediator mass up to 50 GeV in the scalar case for a DM particle of 1 GeV.
The recasting of the analysis results in terms of the 2HDMa model has allowed to set the first ATLAS limits on this model, that will be more deeply investigated with the full Run-II data, in future analyses.

Conclusions and perspectives

A search for Dark Matter (DM) production in association with top quarks based on a Simplified Model has been presented. Data collected at the ATLAS experiment in 2015 and 2016 for a total integrated luminosity of 36.1 fb^{-1} were analysed, at $\sqrt{s} = 13$ TeV. The model describes the coupling between Dark and Standard Model sectors as mediated by a spin 0 scalar or pseudoscalar particle. A final state with two leptons, from the top quarks decays, $E_{\text{T}}^{\text{miss}}$ and jets has been considered. The data event counts observed has been compared to the expected SM background, showing a good compatibility. Results have been interpreted in terms of limits on the model as a function of the mass of the mediator and the Dark Matter particle and in the context of a generic BSM signal. In particular scalar mediators with mass up to 50 GeV have been excluded for a DM particle of 1 GeV. The same results have been also reinterpreted in terms of a model extending the Simplified one, described above, and foreseeing two Higgs doublet (2HDMa). This model is particularly attractive since it extends the SM, while being compatible with the stringent Higgs physics constraints. It will be the focus of many other searches in the next analyses round based on the full dataset collected in Run II for about 150 fb^{-1}.

The near future will also be a challenge for detector upgrades. The ATLAS New Small Wheels (NSW) upgrade of the muon spectrometer has entered the mass production phase for what concerns the Micromegas quadruplets, with the goal to build all the detectors in time for their installation during the LS2, starting in 2019. In the thesis many details have been provided concerning the readout Printed Circuit Boards (PCB) production and quality control performed at CERN, together with some of the most relevant challenges that have been faced. At the same time the performance of the Micromegas detectors has been evaluated in a dedicated test facility at CERN, in a very high particle rate environment. The ageing effects on these detectors have been evaluated after accumulating 0.3 C/cm^2 in about 3 years, several times what is expected in 10 years of LHC operations. Both studies have been successful. No degradation of the performance has been observed up to 70 kHz/cm^2, considering that the highest rate in the NSW, close to the beam pipe, has been estimated in 15 kHz/cm^2. No ageing effects have been observed either.

Appendix A

Particle interactions with matter

In this chapter a brief summary of the physics processes governing the interaction between particles and matter is presented, with a particular emphasis on those responsible for the signal generation on gaseous detectors. In Section A.4 some aspects of the charge amplification are also discussed.

A.1 Interaction of charged particles with matter

A relativistic heavy charged particle travelling in the matter interacts with the electrons of the material, feeling the coulomb potential. In any of such interactions, depending on the proximity, the energy transferred may be sufficient to raise the electron to an outer shell (excitation), or to completely remove it, ionizing the atom. The mean value of the energy deposition is well described in a wide range of energies (namely $0.1 < \beta\gamma < 1000$, where $\beta = \frac{v}{c}$ and γ is the relativistic factor) by the Bethe-Block formula:

$$\frac{dE}{dx} = -Kz^2\frac{Z}{A}\frac{1}{\beta^2}ln\frac{2m_ec^2}{I}\beta^2\gamma^2 - 2\beta^2 - \frac{\delta(\beta)}{2} \tag{A.1}$$

where $K = 4\pi N_A r_e^2 m_e c^2$ with N_A being the Avogadro's number, r_e the classical electron radius, and m_e the electron mass. z is the charge of the incident particles, while Z and A are the atomic and mass numbers of the absorber respectively. I is the mean excitation potential of the gas. This equation for intermediate-Z materials shows an accuracy of few percent. In figure A.1 several examples of stopping powers are shown for different particles. What is relevant to notice out of this equation is that there is no dependence to the mass of the charged particle, but only to its charge and velocity squared. Moreover the material composition enters in the formula with the effective atomic number Z/A. For values $\beta\gamma \sim 3$ the stopping power shows a minimum: particles in

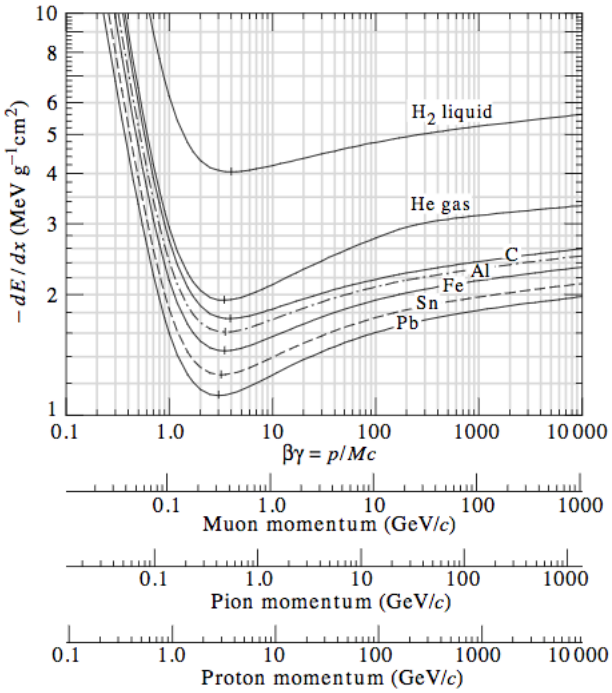

Figure A.1: Stopping power, or loss of energy E per unit path length, as a function of the momentum for different particles in different materials. Radiative effects, relevant at higher and lower momenta are not included.

this regime are called Minimum Ionizing Particles (MIP). Another extremely important feature of the ionization process is the so-called *Bragg additivity*: mixtures or compounds can be imagined as thin layers of pure elements in the right proportion and the total energy deposition can be calculated independently in each layer. For what concerns electrons and positrons, at low energy they mainly deposit energy by ionization, with contributions from other processes, such as Bhabha scattering, annihilation, Moller scattering. At higher energy, namely few tens of MeV in most materials, the loss of energy due to the emission of a photon produced by the acceleration of the particle in the coulomb field (Bremsstrahlung) becomes dominant.

Ionization in gases

As described in the above section, an heavy particle travelling in the matter, and in a gas as well, loses energy leading to the excitation or the ionization of the atoms. While the excitation in a generic atom of the gas requires a well defined energy, being a resonant reaction, the ionization has no energy requirements, while presenting, on the other hand, a high energy threshold. Typical cross sections values for ionization are of the order of $\sigma = 10^{-16}\text{cm}^2$. Electrons and ions produced directly by the incident radiation are called primary ionizations. If the energy transferred to the electrons is high enough (delta rays)

Gas	ρ (g/cm^3) (STP)	I_0 (eV)	W_i (eV)	dE/dx (MeVg^{-1}cm^2)	n_p (cm^{-1})	n_t (cm^{-1})
H_2	$8.38 \cdot 10^{-5}$	15.4	37	4.03	5.2	9.2
He	$1.66 \cdot 10^{-4}$	24.6	41	1.94	5.9	7.8
N_2	$1.17 \cdot 10^{-3}$	15.5	35	1.68	(10)	56
Ne	$8.39 \cdot 10^{-4}$	21.6	36	1.68	12	39
Ar	$1.66 \cdot 10^{-3}$	15.8	26	1.47	29.4	94
Kr	$3.49 \cdot 10^{-3}$	14.0	24	1.32	(22)	192
Xe	$5.49 \cdot 10^{-3}$	12.1	22	1.23	44	307
CO_2	$1.86 \cdot 10^{-3}$	13.7	33	1.62	(34)	91
CH_4	$6.70 \cdot 10^{-4}$	13.1	28	2.21	16	53
C_4H_{10}	$2.42 \cdot 10^{-3}$	10.8	23	1.86	(46)	195

Figure A.2: Properties of the most common gases

supplementary *secondary* ionizations occur. Primary ionizations are statistical phenomena and the their occurrence follows the Poissonian distributions. The mean value of ionizations, however, can be estimated by:

$$n_t = \frac{\Delta E}{W_i} \tag{A.2}$$

where ΔE is the mean energy loss for a minimum ionizing particle and W_i is average energy needed per ion pair. Typical values are 25-35 eV/ion pair and, surprisingly, does not depend strongly on particle type. Properties of the most common gases are reported in Fig. A.2.

A.2 Photons interactions with matter

A large variety of processes involves photons and their interactions with matter. However, only three of them are relevant for radiation measurement. Those are the photoelectric effect, the Compton scattering, and the pair production. Typically the interaction involves the production of electrons, which are later detected by ionization. Unlike the interaction of charged particles, photons interactions are a binary process. Or the photon is absorbed and then eventually re-emitted at lower energy or the interaction does not occur. Given this peculiarity, and defined I_0 as the original mono-energetic photon beam intensity, the intensity after traversing a layer of thickness x is given by:

$$I(x) = I_0 exp(-\frac{\mu}{\rho}x) \tag{A.3}$$

where ρ is the density of the material and μ/ρ is the mass attenuation coefficient. The inverse of the mass attenuation coefficient can also be seen as

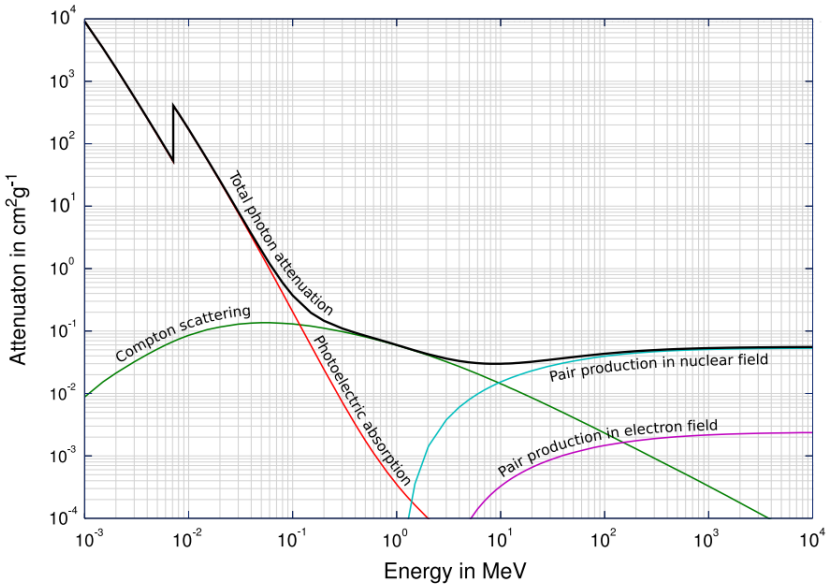

Figure A.3: Mass attenuation coefficient as a function of photon energy for a generic material.

the mean free path between two successive interactions. The three processes dominate at different photon energy ranges, as it is shown in Fig. A.3. At lower energy, namely smaller than 100 keV the photoelectric effect dominates. For energies bigger than 10 MeV it is the pair production process to have the highest cross section. In the energy range between those the most probable interaction is the Compton scattering.

Photoelectric effect

Photoelectric process takes place when the photon is absorbed by an electron on a shell of a nucleus. The energy of the photon has to be higher than the binding energy of the electron. Consequentially to the absorption, the electron is emitted leaving an empty vacancy in the shell as shown in Fig. A.4. This hole is then filled by an electron from an outer shell, emitting a fluorescent photon with energy equal to the difference between the two shells. The energy from the electronic transition may be eventually be transferred to a weakly bounded electron of the same shell. This last is called Auger effect.

Compton scattering

The Compton scattering, as already observed, is the dominant process in the keV-MeV energy range. It consists in a scattering of the photon on the electrons, with a partial transfer of the photon energy to the electron as shown in

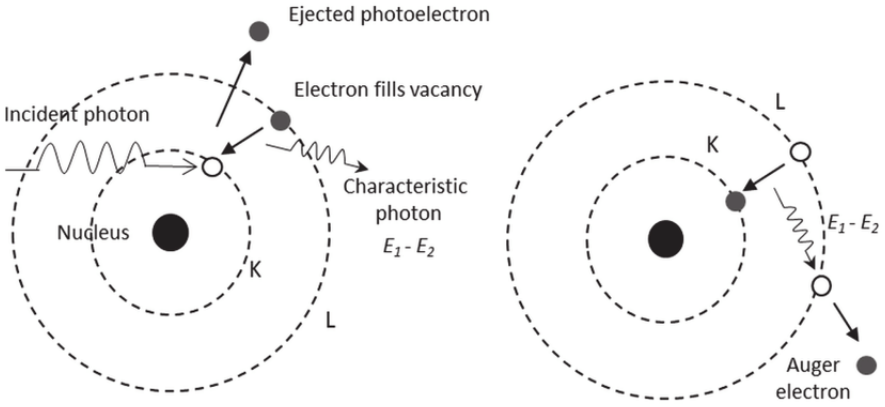

Figure A.4: Schematic of the photoelectric effect with emission of a photon (left) and with emission of an Auger electron (right).

Fig. A.5. The photon wavelength is shifted by:

$$\Delta\lambda = \frac{h}{m_e c}(1 - cos(\theta) \tag{A.4}$$

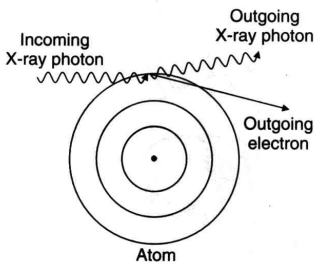

Figure A.5: Scheme of the Compton scattering.

Pair production

The pair production process can only occur when the photon energy is more than twice the rest mass of the electron. It consists in the trasformation of a photon in a electron-position couple (Fig. A.6).

A.3 Drift of Electrons and Ions in Gases

Ions and electrons, generated by the radiation, in presence of an electric field, drift along the field lines. For ions, the drift velocity can be approximated by the following relation:

$$\vec{v} = \frac{\mu\vec{E}}{p} \tag{A.5}$$

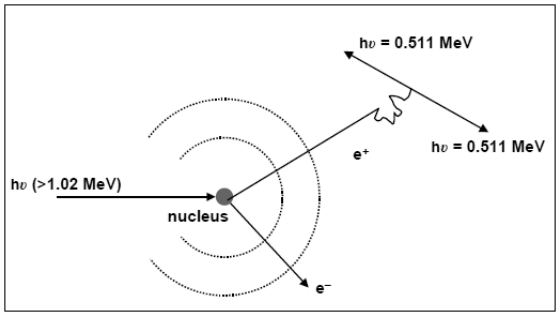

Figure A.6: Pair production of a photon in a nucleus field.

where μ is the ions mobility, $\vec{E}$ is the electric field and p is the gas pressure. Mobility for ions depends on the gas considered and it is fairly constant over a wide range of electric field. Typical values are between 1 and $1.5 \cdot 10^{-4}$ m^2atm/V. Therefore, for atmospheric pressure and field of about 10^4 V/m drift velocity assumes values of the order of 1 m/s. Electrons, on the other hand, are about 1000 times faster. This is due to their lower mass, allowing greater acceleration between successive interactions with the neutral gas molecules. The drift velocity of the ions, being the slower, is a critical parameter in gaseous detectors, since it defines the length of the signal. Reaching higher drift velocity would allow to improve the rate capability of the detectors. In [118] and [119] a comprehensive study of the drift velocity for different combinations of Argon and $C0_2$, relevant for this thesis, and a much more detailed analysis of the topic, have been performed.

A.4 Gas amplification

The number of electrons and ions produced by the radiation are not enough to provide a readable signal. A process of amplification is thus needed. In gaseous detectors this is performed by accelerating the electrons with an adequate electric field in order to further ionize the atoms. The amplification process can be describe by

$$n(x) = n_0 exp(\alpha x) \tag{A.6}$$

where n_0 is the number of electrons entering the intense electric field region, x is the path length and α is the Townsend coefficient. The so-called gas gain is the ratio between the number of electrons at the end of the amplification and the initial ones. The gas gain can be largely influenced by the density of the gas. In gases, the density can be expressed in terms of pressure (p) and temperature (T) by

$$n = \frac{p}{K_B T} \tag{A.7}$$

where K_B is the Boltzmann constant. A parametrization of the Townsend coefficient [120] as a function of the density of the gas is given by

$$\alpha = A_0 n \exp\left(-\frac{B_0 n}{E_{amp}}\right) \tag{A.8}$$

where $A_0 = k_B A$ and $B_0 = k_B B$. A and B are gas dependent parameters. The above mentioned relation, works as long as the space charge due to ions is negligible with respect to the field. When this situation is not satisfied any more, the electrons charge enhances the field, leading to an even higher amplification resulting in discharges and breakdown. An empirical limit to the amplification, before breakdown occurs, can be found in [121].

Appendix B

The Gamma Irradiation Facility at CERN (GIF++)

In this chapter the main aspects of the GIF++ facility will be provided. This appendix is supporting the ageing studies carried out on the Micromegas prototypes described in the core of the thesis. The main reference is [62].

B.1 Description of the facility

The Gamma Irradiation facility (GIF++) at CERN, is located at the former SPS West Area and it is dedicated to the long term ageing studies in high particle rate background of gaseous detectors designed for LHC High Luminosity experiment upgrades. It combines a radioactive source, ^{137}Cs, having an initial activity of 14 Tb and an half-time of about 30 years, with a muon and high rate pion beams.

The Cesium source has been chosen to guarantee long lifetime, with respect

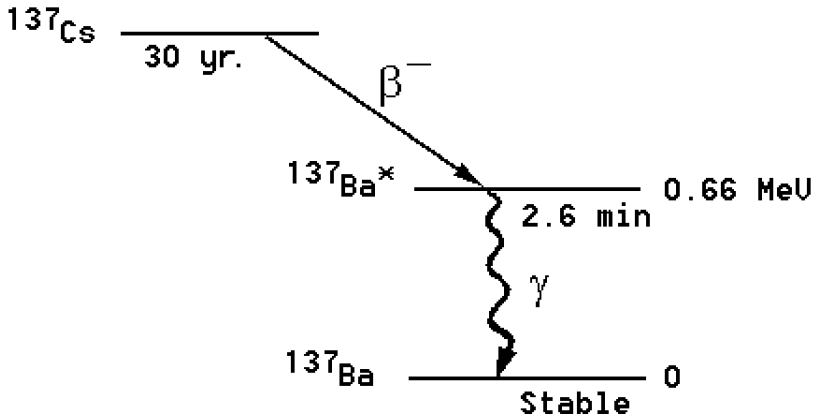

Figure B.1: ^{137}Cs decay

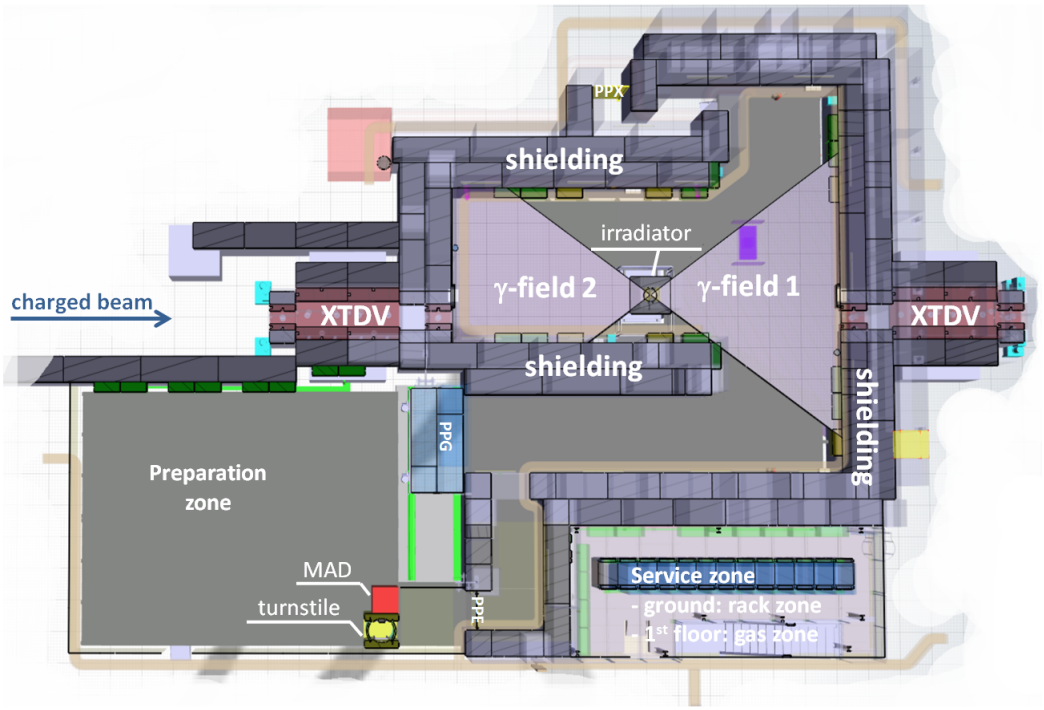

Figure B.2: Layout of the bunker

to ^{60}Co, and also because the neutron-induced background radiation in LHC environment is well described by the energy spectrum of the source, mainly dominated by 662 keV photons. Figure B.1 shows the reference Cesium decay. The Cesium decays in a excited state of ^{137}Ba via beta decay, followed by a gamma emission decay to the ground state.

The facility has been designed to maximize the number of setup installed for a total surface of about 100 m^2 with a total height of 4.8 m. The layout of the facility is shown in Fig. B.2.

The source is placed in the middle of the bunker area, creating two different radiation zones, upstream and downstream. The photon flux can be modified by means of filters, 9 in total, that can be combined in series of three for a total possible number of combinations equal to 27. A dedicate simulation of the whole bunker and of the source has been carried out in order to characterize the photon field at different position in the bunker. Figure B.3a shows the expected photon current in a vertical plane at the same height of the source without any attenuation filter. Collimators have been designed to make photon flux as uniform as possible on the x-y plane. Figure B.3b shows the source spectrum as simulated at about 1 meter from the source for three different attenuation values. About half of the current comes from the 662 keV peak, plus a lower energy background due to scattering.

A measurement campaign has been performed to compare the expected reduction of the photon flux with the measured one for different combinations of the available filters.

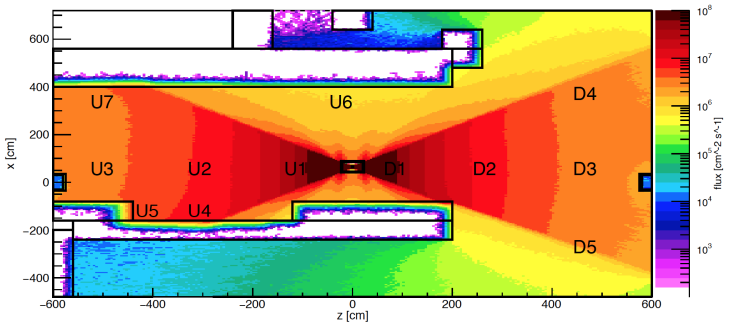

(a)

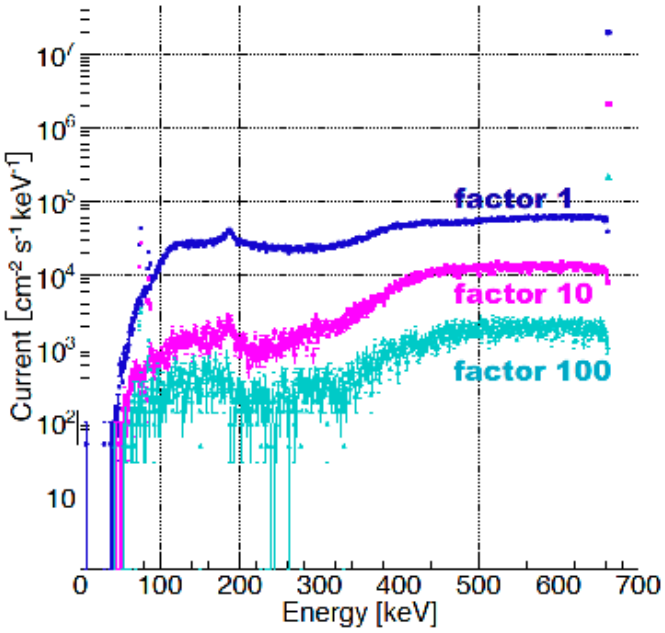

(b)

Figure B.3: Total flux simulated with source fully opened. Indication of some reference positions in the bunker are given (a). Spectrum of the photons for different attenuation filters (b)

Table B.1: Comparison between expected and measured attenuation doses for various filter combinations

	Measured Attenuation	
Expected att. of 662 KeV gammas	Dose [mSv/h]	Meas. att.
1	470.00	-
1.5	400.00	1.2
2.2	2110.00	2.2
4.6	105.00	4.5
10	55.00	8.8
100	6.50	72.3
100	6.20	75.8
464	1.59	295.6
4642	0.22	2156.0
46420	0.05	9400

Results are reported in Table B.1: at higher fluxes, the expected and measured attenuations are very similar, while the difference increases at lower fluxes where the contribution from low energy photons from scattering become relevant. More information concerning the measurement and the setup used can be found in Ref. [62]. The expected photon current, considering different bins of energy, is reported in Table B.2 for the same reference positions in the bunker already shown in Fig. B.3a. The last column reports the percentage of the photon flux due to the Cesium peak; in average about 50% of the photons have an energy of 662 keV.

Table B.2: Photon current expect at different reference positions. Almost half of the current comes from the 662 keV peak

photon current ($10^6 cm^{-2} s^{-1}$)										
//	Energy bins (keV)									//
Position	0-100	100-200	200-300	300-400	400-500	500-600	600-662	0-662	661-662	%
D1	0.36	2.92	2.44	3.29	5.18	5.88	23.8	43.9	20	45.5
D2	0.17	0.72	0.45	0.35	0.67	0.83	3.34	6.52	2.79	42.8
D3	0.14	0.47	0.22	0.2	0.23	0.29	1.14	2.7	0.95	35.2
D4	0.12	0.38	0.19	0.13	0.14	0.15	1.28	2.39	1.17	48.7
D5	0.11	0.32	0.17	0.13	0.15	0.15	1.29	2.32	1.17	50.3
U1	0.39	2.96	2.44	3.3	5.14	5.89	23.8	43.9	20	45.5
U2	0.21	0.81	0.41	0.34	0.66	0.83	3.38	6.64	2.82	42.6
U3	0.19	0.57	0.28	0.2	0.23	0.28	1.15	2.91	0.96	33.1
U4	0.29	0.95	0.49	0.27	0.33	0.35	3.82	6.51	3.54	54.4
U5	0.34	0.86	0.45	0.32	0.29	0.26	1.71	4.23	1.52	35.9

Appendix C

Development of Small Pad resistive Micromegas

The following appendix describes the development of a Micromegas detector based on resistive pads I have been actively contributing to. The aim of the project is to develop a detector design suitable for very high particle rate environments of the order of few MHz/cm^2. The results here reported are based on the conference proceeding prepared and submitted by myself in occasion the MPGD 2018 international conference.

C.1 Small-pad resistive Micromegas

Resistive Micromegas technology has been developed, as it has been showed in the main core of the thesis, in view of its use in large area detectors in the context of the ATLAS New Small Wheels upgrade. The detector design is based on standard Micromegas structure, composed of a drift and amplification gaps, and copper readout strips. The term *resistive*, as already seen, denotes the presence of a resistive strip pattern, insulated from the readout ones by means of a Kapton® foil. With this design high rate tests have been performed and no degradation of the performance in high particle rate environment up to 70 kHz/cm^2 has been observed. The main obstacles to reach even higher particle rate are represented by the voltage drop due to the resistivity of the strips, leading to a reduction of the effective amplification field, and by the occupancy increase, which, at its turn, lead to the impossibility to distinguish overlapping events.
However, it is of great importance to investigate and improve these two aspects, as future applications will require detectors to sustain particle rate of about 10 MHz/cm^2.
An approach, already reported in [122],[123], to overtake both the limitations, has been proposed, based on the replacement of the readout and resistive strips with rectangular pads. The PCB schema of the newly developed prototype is

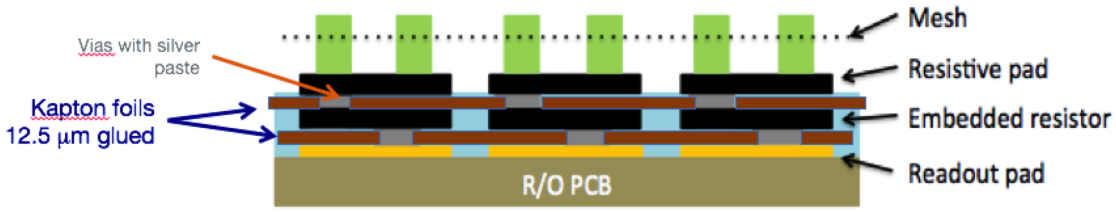

Figure C.1: The resistive pads readout PCB introduces pads and embedded resistor instead of strips

shown in Fig. C.1. To evacuate the charges embedded resistors have been used, as shown in the figure, having a resistivity of few MΩ. The pattern of the pads is a matrix of 48×16 for a total number of 768 pads, each pad being 1×3 mm^2. Each pad corresponds to an individual readout channel, routed at the edge of the board, where the APV 25 electronics is plugged. The detector is completed by a 5 mm drift gap, and a amplification one of about 100 µm. The active area is 5×5 cm^2.

C.2 Small-pad detector performance

The first characterization of the detector has been performed by means of X-rays and Iron sources (^{55}Fe). The gas used for all the tests here reported is always $ArCO_2$ (93:7), the usual mixture used also in the context of the NSW detectors. Amplification voltage is applied between pads and mesh, drift voltage between mesh and drift electrode. The energy resolution of the detector has been measured by exposing the detector to an Iron source and acquiring the detector current from the readout pads with a Multi Channel Analyser (MCA) for different values of amplification voltage as shown in Fig. C.2. An energy resolution of about 30% has been obtained, slightly worse than previous results obtained using standard resistive Micromegas detectors. This results is not surprising: due to the highly segmented pattern and large border effects, the electric field is rather inhomogeneous.

Always by using iron sources, the detector gain as a function of the amplification voltage has been measured. In particular two sources have been used, one characterized by a low activity (1.3 kHz detected hits), and a second one about 100 times more intense (128 kHz). The measurements, reported in Fig. C.3, show a reduction of the gain of about 20% if the more intense source is considered with respect to the weak one. A similar effect is also observed if the dependence of the gain as a function of time is measured: Figure C.4 shows the current evolution after placing the intense iron source on the detector for few tens of seconds, also in this case for different amplification voltages. This current reduction suggests that charge-up of the dielectric takes place when the intense source is used (higher particle rate), implying a local reduction of

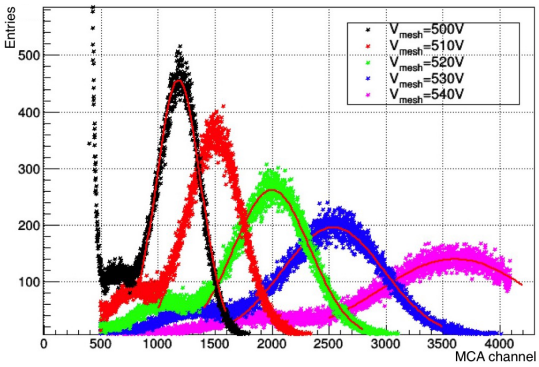

Figure C.2: Iron source spectrum for different values of the amplification field as obtained by a multi channel analyser (MCA).

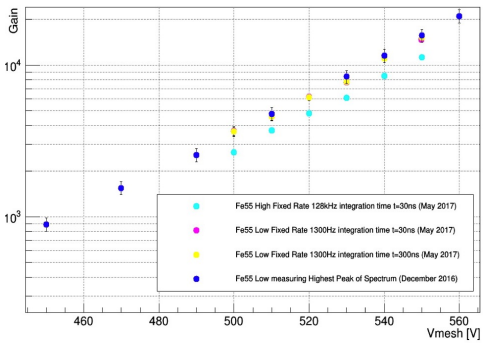

Figure C.3: Gain as a function of the amplification voltage for the two iron sources (Low = 1.3 kHz, High = 128 kHz). Comparison among measurements performed in different periods is shown

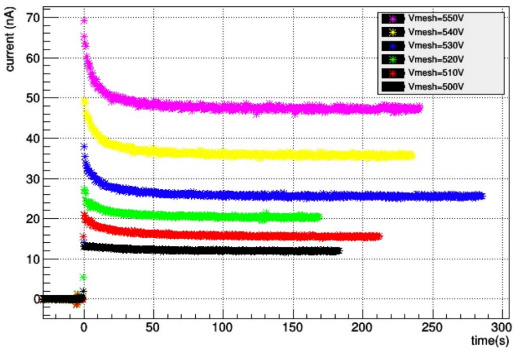

Figure C.4: Detector current as a function of time in the first seconds after placing the high rate (128 kHz) iron source on the detector

the amplification field. A saturation behaviour is then reached after initial charge-up.

The rate capability of the detector and the gain behaviour as a function of the rate have been studied extensively by means of an X-rays gun available at the Gas Detector Development (GDD) laboratory at CERN, providing 8 keV photons from a Cu anode.

The particle rate reaching the detector could be tuned by setting the current of the X-ray gun and by focusing photons with a 3 mm Cu collimator or with a 10 mm hole absorber. The particle rate has been estimated by reading the signal rate on the mesh as already done for the gain measurement and described in the main core of the thesis. Figure C.5 shows the gain as a function of the particle rate for different values of the amplification voltage. Also in this case, as expected after the previous considerations on the charge-up effect, a reduction of the gain of about 25% has been observed at higher

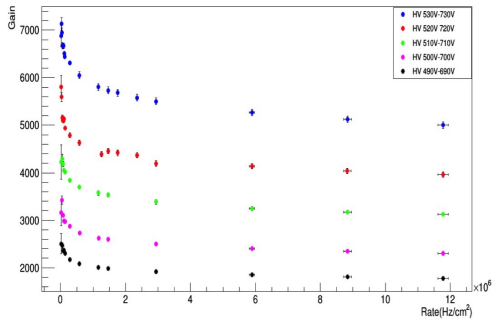

Figure C.5: Detector readout current as a function of the rate for different values of the amplification field. An X-ray gun with a 10 mm hole absorber has been used for the measurements.

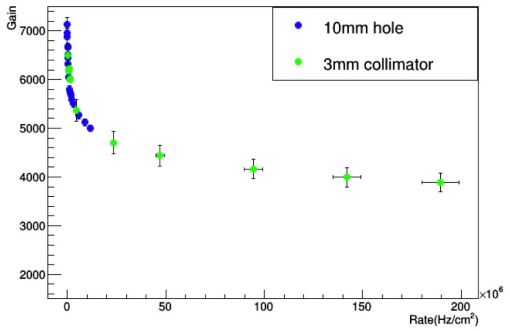

Figure C.6: Detector current as a function of the rate for a fixed amplification value. An X-ray gun with a 10 mm hole (blue points) or a 3 mm collimator (green points) have been used for the measurements.

particle rate. In this case, however, in addition to the charge-up effect, also the voltage drop due to resistivity of the pads is contributing to the reduction of the gain. Figure C.6 shows the gain as a function of the particle rate measured for a fixed value of the amplification field (530 V between readout and mesh) using the absorber and the collimator. Despite the gain reduction, a value of 4×10^3 has been measured at 150 MHz/cm^2. This result confirms that the detector could be still operated efficiently at this rate.

Performance at testbeam

Detector performance, such as the efficiency to particles, tracking capabilities and resolution have been studied in a testbeam campaign at the SPS facility at CERN, where high energy muon and pion beams are available. Data have been acquired with the usual APV-25 hybrids and RD51 SRS system already briefly described in the core of the thesis. Two double view Micromegas bulk detectors, the same used also as tracking chambers in the GIF++ testbeam, have been used to reconstruct the expected position of the track on the pad detector. The reconstruction of the clusters on the pad detector has been

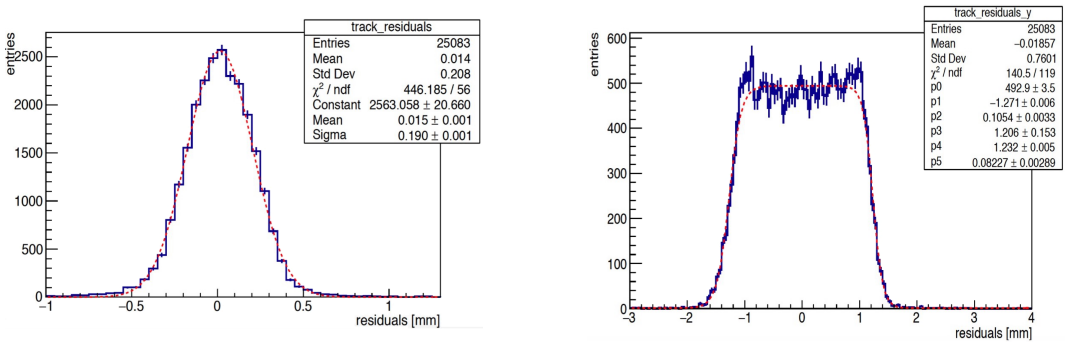

(a) (b)

Figure C.7: Residual distribution between expected and reconstructed cluster position for precise coordinate (C.7a) and second coordinate (C.7b)

performed by combining the information from neighbouring fired pads. The resolution has been evaluated comparing the cluster position reconstructed on the detector with the expected position obtained from tracking detectors, and then subtracting the uncertainty on the track interpolation. Figure C.7a shows the residual distribution considering the most accurate coordinate, corresponding to the short side (1 mm) of the pads. A resolution of 190 µm has been observed. For what concerns the less accurate coordinate, corresponding to the 3 mm side of the pads, a resolution of 800 µm has been found.

Another relevant aspect of the detector is the efficiency to muons as a function of the amplification voltage. An event is considered if one and only one cluster is detected on the tracking chambers and defined efficient if a cluster on the pad detector is found within 3 times the resolution of the accurate coordinate around the expected position. Figure C.8 shows the efficiency curve, which saturates toward a value of around 98%. The red points show the trend of the efficiency when the whole chamber, instead of the small fiducial region, is considered.

As a final remark, the number of fired pads in a cluster has been found to depend on the position of the particle traversing the detector. If the track crosses a pad close to its center, a higher probability to generate a cluster composed of an odd number of pads has been observed, as shown in figure C.9a. On the other hand, if the track passes close to the edge of a pad (as limit case, exactly in between two pads), an higher probability to reconstruct a cluster having an even number of fired pads has been measured (figure C.9b).

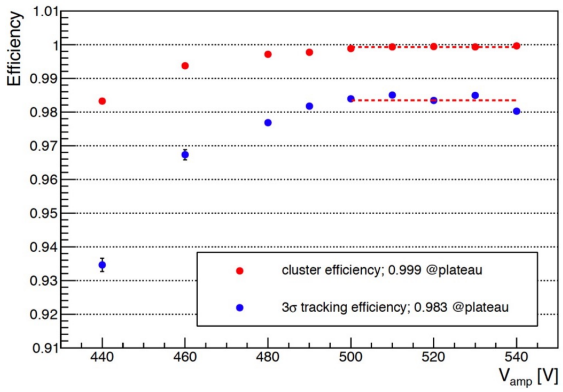

Figure C.8: Cluster efficiency as a function of the amplification field. The red points show the efficiency when clusters are selected in the whole detector: the plateau reaches about the 99.9%. The blue points represent the efficiency obtained by selecting clusters lying closer than 3 times the resolution of the accurate coordinate (3σ) from the expected position. In this case, the plateau reaches the 98%.

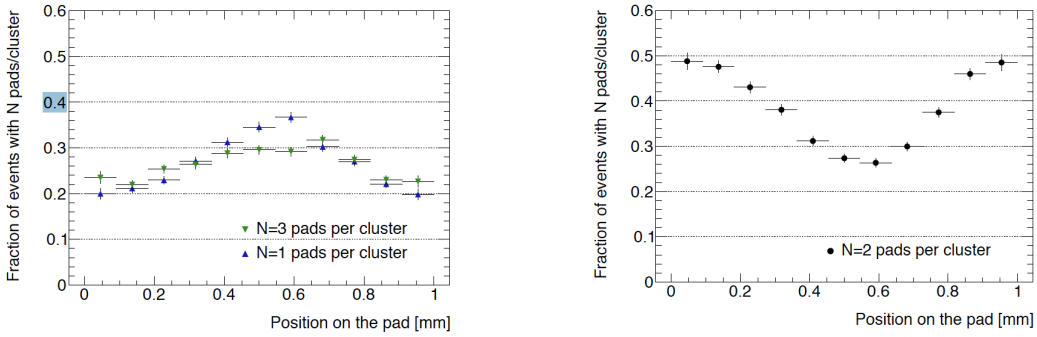

(a) (b)

Figure C.9: Probability of firing an odd (a) and even (b) number of pads per cluster as a function of the position of the extrapolated track in the pad.

Appendix D

Development of the INFN Micromegas QAQC DB

In this chapter the main aspects of the ATLAS New Small Wheels databases are reported, in particular focusing on the INFN QAQC database development, its own web interface and some aspects of the strategy adopted by the Italian construction sites to provide the data. I have been personally worked on the architecture of the Italian database, on its development, and on its web interface, with the help and support of the NSW CERN databases responsible, Kim Temming, which I am deeply grateful.

D.1 NSW Databases

The ATLAS NSW databases have been designed to record all the items (starting from bolts and screws, up to to entire quadruplet assembled) build or used by the Collaboration. It also contains all the functionalities to know the exact location at every time of the objects and also to keep track where items are mounted, for example which PCBs have been used in a specific panel. This last feature is known as *parenting*. Two dedicated databases, based on Oracle® have been realized:

- The Logistic Database records all the items, their locations and manage the parenting.
- The QAQC Database contains all the data related to the quality control performed on the object (both raw material or final modules) selected to be centrally stored. Only objects defined in the Log database can have data in the QAQC database.

The Log database is already used since almost 2 years, and it proved to be a solid and reliable system. It is used not only by the detector construction sites, but the integration, electronics, service installation groups as well. Concerning

the QAQC database, more details are given in the following.
A schema of the internal database tables is reported in Fig. D.1. Among all, the most relevant are the so-called *Central measurement* and *Contexts*. Without entering into details, the first one contains the values that have been measured and stored, the unique ID of the object that has been measure (linking to the LOG database) and another ID referring to the *context* table, containing an entry for each physics quantity to be registered. Filling the database means finding the unique ID of the object under test (for example Readout panel), recall the ID of the measurement itself (mean value of the planarity vacuum on) and upload the previous two IDs, combined with the value measured in the *Central measurement* table. This approach has been adopted to provide the best versatility as possible. Adding a new type of measurement, for example, does not require any modification in the database structure, but simply a new entry, with relative new ID, in the *Contexts* table.

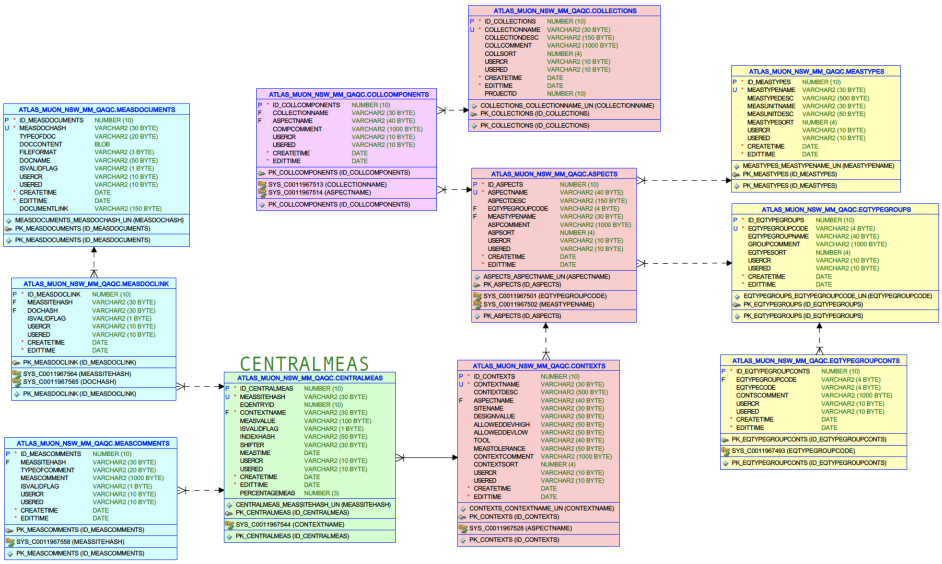

Figure D.1: Simplified view of the QAQC DB structure. Connection to the logistic database is not drawn

While the LOG database is filled by the construction sites, directly accessible through a dedicated web interface, the QAQC one does only provide a read only interface. Data is automatically fetched by local databases developed, maintained and filled by the construction sites. The interplay among the databases is shown in Fig. D.2. The external collaboration will access only the information made available in the Central Database and in the Log. The Italian sites, for example, building a panel, will update the information concerning the status, the object parenting and the shipment information directly in the Log database. At the same time, QAQC data will be uploaded to a local database, the *INFN QAQC database*, which, at its turn, will pull the information in the Central Database.

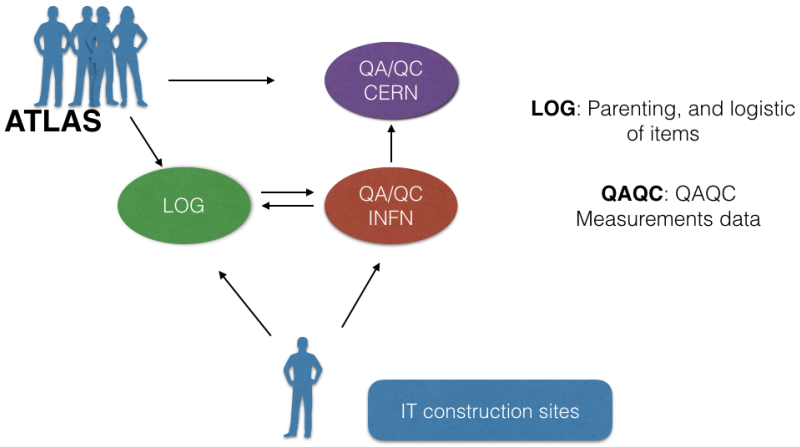

Figure D.2: Interplay among databases

The most efficient strategy for the development of local databases would have been to replicate a structure as close as possible to the central one, to be automatically compatible when transferring the data. Indeed, the strategy that has been implemented for Italy and then copied by almost all the other sites, has been to develop a new database, owing copies of the *Central measurement* table, while referring for what concerns the other ones directly to the central database. All the functionalities are thus provided; all the changes made in the central database are automatically inherited by all the local databases without any possible issue. The *Central measurement* table is then slightly modified to host a flag allowing or preventing the central database from fetching the new entries.

In Italy, five different sites have to provide information and they are shown in Fig. D.3.

- Pavia is responsible for the Readout panels (RO) production.
- Rome 1 has to build the drift panels, then sent for the assembly together with the RO panels.
- Rome 3 prepares the meshes, stretched on a metallic frame, called *transfer frame*. Meshes are mounted on drift panel at Frascati site.
- Frascati 1 is where drift panels are finalized, mounting the meshes on the drift structure built in Rome 1.
- Frascati 2 proceeds with the final assembly, coupling RO and Drift panels and closing the quadruplet structure.

To perform the QAQC measurements defined by the Collaboration, each site has developed its own strategy, according to the available manpower, expertise, and construction procedure. To fill the database the simplest and

Figure D.3: Italian consortium

less impacting strategy on the already present procedures has been adopted. Each site already provides data as output of a Labview steering programme, or filled by dedicated script. These outputs become inputs for dedicated scripts, which reorganize the information in a form suitable for being digested by the database, and, if instructed, proceed to the final upload. The procedure is shown in Fig D.4. At time of writing, July 2018, 3 out of 5 sites are already filling successfully the database.

Figure D.4: Filling schema strategy for Italian sites. Output files from steering programs (LabView) are converted in a suitable form by automatic script and uploaded to the database

Providing a tool to consult the database information has been another crucial task. This feature is now available through a dedicated web interface, which is shown in Fig. D.5. Three search possibilities are provided: the easiest one simply displays the tables content, the second one runs predefined queries and deploys distributions that can be printed and saved for later use, while the third one allows the user to perform customized searches based on criteria such

as location, equipment type, measurement type. The development of the web interface is still on-going based on the feedbacks provided by the the users.

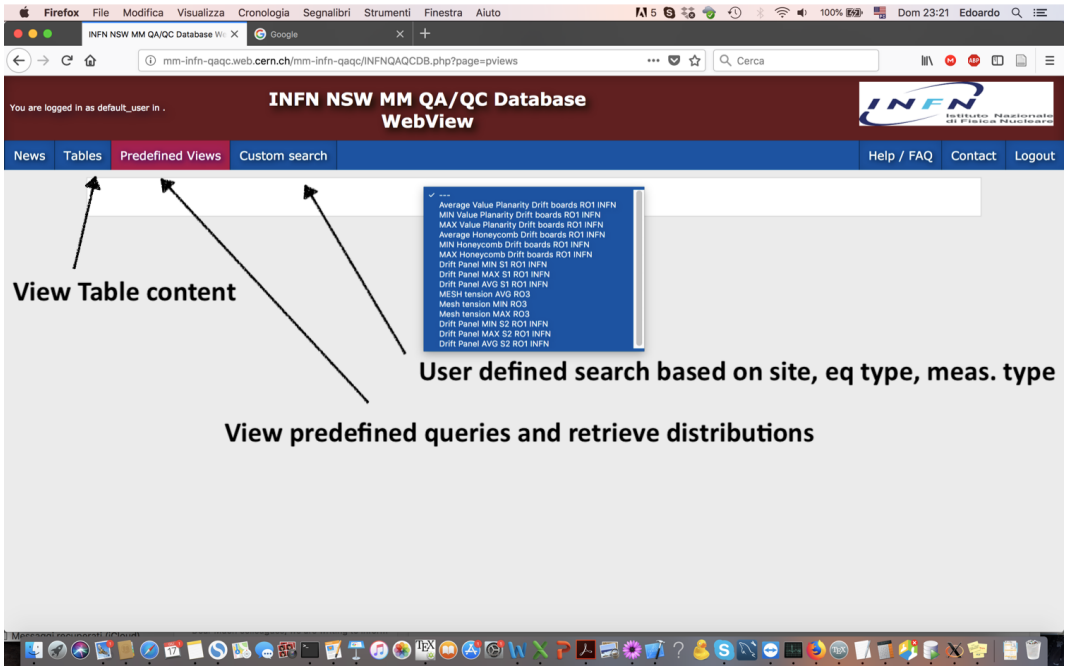

Figure D.5: Web Interface

Bibliography

[1] ATLAS Collaboration. Observation of a new particle in the search for the standard model higgs boson with the atlas detector at the lhc. *Physics Letters B*, 716(1):1 – 29, 2012.

[2] CMS Collaboration. Observation of a new boson at a mass of 125 gev with the cms experiment at the lhc. *Physics Letters B*, 716(1):30 – 61, 2012.

[3] Samoil M. Bilenky and J. Hosek. Glashow-Weinberg-Salam theory of electroweak interactions and the neutral currents. *Phys. Rept.*, 90:73–157, 1982.

[4] Peter W. Higgs. Broken symmetries and the masses of gauge bosons. *Phys. Rev. Lett.*, 13:508–509, Oct 1964.

[5] G. P. Lepage. Lattice QCD for novices. In *Strong interactions at low and intermediate energies. Proceedings, 13th Annual Hampton University Graduate Studies, HUGS'98, Newport News, USA, May 26-June 12, 1998*, pages 49–90, 1998.

[6] Jonathan L. Feng. Naturalness and the Status of Supersymmetry. *Ann. Rev. Nucl. Part. Sci.*, 63:351–382, 2013.

[7] Stephen P. Martin. A Supersymmetry primer. pages 1–98, 1997. [Adv. Ser. Direct. High Energy Phys.18,1(1998)].

[8] S. Dawson. SUSY and such. *NATO Sci. Ser. B*, 365:33–80, 1997.

[9] P. Fayet. Supersymmetry and weak, electromagnetic and strong interactions. *Physics Letters B*, 64(2):159 – 162, 1976.

[10] Dragan Huterer and Daniel L Shafer. Dark energy two decades after: Observables, probes, consistency tests. *Rept. Prog. Phys.*, 81(1):016901, 2018.

[11] Miao Li, Xiao-Dong Li, Shuang Wang, and Yi Wang. Dark Energy: A Brief Review. *Front. Phys.(Beijing)*, 8:828–846, 2013.

[12] Katherine Garrett and Gintaras Duda. Dark Matter: A Primer. *Adv. Astron.*, 2011:968283, 2011.

[13] J H Oort. The force exerted by the stellar system in the direction perpendicular to the galactic plane and some related problems. *Bull. Astron. Inst. Netherlands*, 6:249–287, 1932.

[14] Vera C. Rubin, W. Kent Ford, Jr., and Norbert Thonnard. Extended rotation curves of high-luminosity spiral galaxies. IV. Systematic dynamical properties, Sa through Sc. *Astrophys. J.*, 225:L107–L111, 1978.

[15] Anton G. Bergmann, Vahe Petrosian, and Roger Lynds. Gravitational lens models of arcs in clusters. *ApJ*, 350, 03 1990.

[16] C. L. Bennett et al. Nine-Year Wilkinson Microwave Anisotropy Probe (WMAP) Observations: Final Maps and Results. *Astrophys. J. Suppl.*, 208:20, 2013.

[17] D. J. Fixsen. The Spectrum of the Cosmic Microwave Background Anisotropy from the Combined COBE FIRAS and WMAP Observations. *The Astrophysical Journal Letters*, 594:L67–L70, September 2003.

[18] P. A. R. Ade et al. Planck 2015 results. XIII. Cosmological parameters. *Astron. Astrophys.*, 594:A13, 2016.

[19] M. C. Weisskopf, H. D. Tananbaum, L. P. van Speybroeck, and S. L. O'Dell. Chandra x-ray observatory (cxo):overview. *Proc. SPIE Int. Soc. Opt. Eng.*, 4012:2, 2000.

[20] Maxim Markevitch, A. H. Gonzalez, D. Clowe, A. Vikhlinin, L. David, W. Forman, C. Jones, S. Murray, and W. Tucker. Direct constraints on the dark matter self-interaction cross-section from the merging galaxy cluster 1E0657-56. *Astrophys. J.*, 606:819–824, 2004.

[21] Douglas Clowe, Marusa Bradac, Anthony H. Gonzalez, Maxim Markevitch, Scott W. Randall, Christine Jones, and Dennis Zaritsky. A direct empirical proof of the existence of dark matter. *Astrophys. J.*, 648:L109–L113, 2006.

[22] B. Gold, N. Odegard, J. L. Weiland, R. S. Hill, A. Kogut, C. L. Bennett, G. Hinshaw, X. Chen, J. Dunkley, M. Halpern, N. Jarosik, E. Komatsu, D. Larson, M. Limon, S. S. Meyer, M. R. Nolta, L. Page, K. M. Smith, D. N. Spergel, G. S. Tucker, E. Wollack, and E. L. Wright. Seven-year wilkinson microwave anisotropy probe (wmap) observations: Galactic foreground emission. *The Astrophysical Journal Supplement Series*, 192(2):15, 2011.

[23] R. Agnese et al. Search for Low-Mass Weakly Interacting Massive Particles with SuperCDMS. *Phys. Rev. Lett.*, 112(24):241302, 2014.

[24] Klaus Eitel. The edelweiss dark matter search: Status and perspectives. *Physics Procedia*, 61:61 – 66, 2015. 13th International Conference on Topics in Astroparticle and Underground Physics, TAUP 2013.

[25] M.C. Carmona-Benitez and othes. First results of the lux dark matter experiment. *Nuclear and Particle Physics Proceedings*, 273-275:309 – 313, 2016. 37th International Conference on High Energy Physics (ICHEP).

[26] R. Bernabei et al. First model independent results from DAMA/LIBRA-phase2. 2018.

[27] Jennifer M. Gaskins. A review of indirect searches for particle dark matter. *Contemp. Phys.*, 57(4):496–525, 2016.

[28] Felix Kahlhoefer. Review of LHC Dark Matter Searches. *Int. J. Mod. Phys.*, A32(13):1730006, 2017.

[29] G. D'Ambrosio, G. F. Giudice, G. Isidori, and A. Strumia. Minimal flavor violation: An Effective field theory approach. *Nucl. Phys.*, B645:155–187, 2002.

[30] Jalal Abdallah et al. Simplified models for dark matter searches at the lhc. *Physics of the Dark Universe*, 9-10:8 – 23, 2015.

[31] Daniel Abercrombie et al. Dark Matter Benchmark Models for Early LHC Run-2 Searches: Report of the ATLAS/CMS Dark Matter Forum. 2015.

[32] Lyndon Evans and Philip Bryant. LHC machine. 3(8):S08001.

[33] Herwig Schopper. *LEP - The Lord of the Collider Rings at CERN 1980-2000*. 01 2009.

[34] Stephen Holmes, Ronald S Moore, and Vladimir Shiltsev. Overview of the tevatron collider complex: goals, operations and performance. *Journal of Instrumentation*, 6(08):T08001, 2011.

[35] The ALICE experiment at the CERN LHC. 3(8):S08002.

[36] The CMS Collaboration. The CMS experiment at the CERN LHC. 3(8):S08004.

[37] The LHCb Collaboration. The LHCb detector at the LHC. 3(8):S08005.

[38] The ATLAS experiment at the CERN large hadron collider. 3(8):S08003.

[39] *ATLAS magnet system: Technical Design Report, 1.* Technical Design Report ATLAS. CERN, Geneva, 1997.

[40] M Aleksa, F Bergsma, P-A Giudici, A Kehrli, M Losasso, X Pons, H Sandaker, P S Miyagawa, S W Snow, J C Hart, and L Chevalier. Measurement of the ATLAS solenoid magnetic field. Dec 2007. Accepted as Scientific Note SN-ATLAS-2008-068.

[41] *ATLAS inner detector: Technical Design Report, 1.* Technical Design Report ATLAS. CERN, Geneva, 1997.

[42] M Capeans, G Darbo, K Einsweiller, M Elsing, T Flick, M Garcia-Sciveres, C Gemme, H Pernegger, O Rohne, and R Vuillermet. ATLAS Insertable B-Layer Technical Design Report. Technical Report CERN-LHCC-2010-013. ATLAS-TDR-19, Sep 2010.

[43] *ATLAS liquid-argon calorimeter: Technical Design Report.* Technical Design Report ATLAS. CERN, Geneva, 1996.

[44] *ATLAS tile calorimeter: Technical Design Report.* Technical Design Report ATLAS. CERN, Geneva, 1996.

[45] ATLAS muon spectrometer: Technical design report. 1997.

[46] ATLAS Collaboration. Performance of the ATLAS Trigger System in 2015. Performance of the ATLAS Trigger System in 2015. *Eur. Phys. J. C*, 77(CERN-EP-2016-241. 5):317. 76 p, Nov 2016. 77 pages in total, author list starting page 61, 50 figures, 1 table. Published in Eur. Phys. J. C. All figures including auxiliary figures are available at http://atlas.web.cern.ch/Atlas/GROUPS/PHYSICS/PAPERS/TRIG-2016-01/.

[47] Georges Aad et al. Performance of the ATLAS Trigger System in 2010. *Eur. Phys. J.*, C72:1849, 2012.

[48] ATLAS Collaboration. Luminositypublicresults. `https://twiki.cern.ch/twiki/bin/view/AtlasPublic/LuminosityPublicResults#Multiple_Year_Collision_Plots`.

[49] G. Apollinari, O. Bruning, T. Nakamoto, and Lucio Rossi. High Luminosity Large Hadron Collider HL-LHC. *CERN Yellow Report*, (5):1–19, 2015.

[50] Expected pileup values at the HL-LHC. Technical Report ATL-UPGRADE-PUB-2013-014, CERN, Geneva, Sep 2013.

[51] Letter of Intent for the Phase-I Upgrade of the ATLAS Experiment. Technical Report CERN-LHCC-2011-012. LHCC-I-020, CERN, Geneva, Nov 2011.

[52] Collaboration ATLAS. Letter of Intent for the Phase-II Upgrade of the ATLAS Experiment. Technical Report CERN-LHCC-2012-022. LHCC-I-023, CERN, Geneva, Dec 2012.

[53] T Kawamoto, S Vlachos, L Pontecorvo, J Dubbert, G Mikenberg, P Iengo, C Dallapiccola, C Amelung, L Levinson, R Richter, and D Lellouch. New Small Wheel Technical Design Report. Technical Report CERN-LHCC-2013-006. ATLAS-TDR-020, Jun 2013. ATLAS New Small Wheel Technical Design Report.

[54] Morad Aaboud et al. Performance of the ATLAS Trigger System in 2015. *Eur. Phys. J.*, C77(5):317, 2017.

[55] J Galán, D Attié, E Ferrer-Ribas, A Giganon, I Giomataris, S Herlant, F Jeanneau, A Peyaud, Ph Schune, T Alexopoulos, M Byszewski, G Iakovidis, P Iengo, K Ntekas, S Leontsinis, R de Oliveira, Y Tsipolitis, and J Wotschack. An ageing study of resistive micromegas for the hl-lhc environment. *Journal of Instrumentation*, 8(04):P04028, 2013.

[56] Y. Giomataris. Development and prospects of the new gaseous detector "micromegas". *Nuclear Instruments and Methods in Physics Research Section A: Accelerators, Spectrometers, Detectors and Associated Equipment*, 419(2):239 – 250, 1998.

[57] S Zimmermann and G Herten. High Rate and Ageing Studies for the Drift Tubes of the ATLAS Muon Spectrometer, 2004. Presented on 18 May 2004.

[58] S Martoiu, H Muller, and J Toledo. Front-end electronics for the scalable readout system of rd51. In *Nuclear Science Symposium and Medical Imaging Conference (NSS/MIC), 2011 IEEE*, pages 2036–2038. IEEE, 2011.

[59] M Bianco, Philipp Loesel, Sorin Martoiu, Ourania Sidiropoulou, and Andre Zibell. Development and test of a versatile DAQ system based on the ATCA standard. *PoS*, TIPP2014:202. 8 p, 2014.

[60] Edoardo Farina. Characterization of large area Micromegas prototype for the ATLAS New Small Wheel upgrade and preliminary aging studies . Master's thesis, University of Pavia, 2015.

[61] S. Agostinelli et al. GEANT4: A Simulation toolkit. *Nucl. Instrum. Meth.*, A506:250–303, 2003.

[62] Dorothea Pfeiffer, Georgi Gorine, Hans Reithler, Bartolomej Biskup, Alasdair Day, Adrian Fabich, Joffrey Germa, Roberto Guida, Martin Jaekel, and Federico Ravotti. The radiation field in the Gamma Irradiation Facility GIF++ at CERN. *Nucl. Instrum. Meth.*, A866:91–103, 2017.

[63] Nikolaos Karastathis. *Determination of the Spin and Parity of the Higgs Boson in the $WW^* \to e\nu\mu\nu$ Decay Channel with the ATLAS Detector*. PhD thesis, Twente U., Enschede, 2016.

[64] Geant4 physics list reference. `https://geant4.web.cern.ch/support/physics_lists/particle_physics/use_cases`.

[65] Hough transform. `https://en.wikipedia.org/wiki/Hough_transform`.

[66] Matthew R. Buckley, David Feld, and Dorival Goncalves. Scalar Simplified Models for Dark Matter. *Phys. Rev.*, D91:015017, 2015.

[67] Georges Aad et al. Search for new phenomena in final states with an energetic jet and large missing transverse momentum in pp collisions at $\sqrt{s}$ =8 TeV with the ATLAS detector. *Eur. Phys. J.*, C75(7):299, 2015. [Erratum: Eur. Phys. J.C75,no.9,408(2015)].

[68] Albert M Sirunyan et al. Search for dark matter produced with an energetic jet or a hadronically decaying W or Z boson at $\sqrt{s} = 13$ TeV. *JHEP*, 07:014, 2017.

[69] A. M. Sirunyan et al. Search for dark matter produced in association with heavy-flavor quark pairs in proton-proton collisions at $\sqrt{s} = 13$ TeV. *Eur. Phys. J.*, C77(12):845, 2017.

[70] Albert M Sirunyan et al. Search for dark matter particles produced in association with a top quark pair at $\sqrt{s} = 13$ TeV. *Submitted to: Phys. Rev. Lett.*, 2018.

[71] Morad Aaboud et al. Search for a scalar partner of the top quark in the jets plus missing transverse momentum final state at $\sqrt{s}$=13 TeV with the ATLAS detector. *JHEP*, 12:085, 2017.

[72] M. Aaboud et al. Search for direct top squark pair production in final states with two leptons in $\sqrt{s} = 13$ TeV pp collisions with the ATLAS detector. *Eur. Phys. J.*, C77(12):898, 2017.

[73] Morad Aaboud et al. Search for top-squark pair production in final states with one lepton, jets, and missing transverse momentum using 36 fb$^{?1}$ of $\sqrt{s} = 13$ TeV pp collision data with the ATLAS detector. *JHEP*, 06:108, 2018.

[74] J. Alwall, R. Frederix, S. Frixione, V. Hirschi, F. Maltoni, O. Mattelaer, H. S. Shao, T. Stelzer, P. Torrielli, and M. Zaro. The automated computation of tree-level and next-to-leading order differential cross sections, and their matching to parton shower simulations. *JHEP*, 07:079, 2014.

[75] Torbjorn Sjostrand, Stephen Mrenna, and Peter Z. Skands. A Brief Introduction to PYTHIA 8.1. *Comput. Phys. Commun.*, 178:852–867, 2008.

[76] Georges Aad et al. Measurement of the Z/γ^* boson transverse momentum distribution in pp collisions at $\sqrt{s} = 7$ TeV with the ATLAS detector. *JHEP*, 09:145, 2014.

[77] Pythia tunes. `http://home.thep.lu.se/Pythia/pythia82html/Tunes.html`.

[78] ATLAS Collaboration, ATLAS Pythia 8 tunes to 7 TeV data, ATL-PHYS-PUB-2014-021, 2014. `https://cds.cern.ch/record/1966419`.

[79] Stefano Carrazza, Stefano Forte, and Juan Rojo. Parton Distributions and Event Generators. In *Proceedings, 43rd International Symposium on Multiparticle Dynamics (ISMD 13)*, pages 89–96, 2013.

[80] Andy Buckley, Jonathan Butterworth, Stefan Gieseke, David Grellscheid, Stefan Höche, Hendrik Hoeth, Frank Krauss, Leif Lönnblad, Emily Nurse, Peter Richardson, Steffen Schumann, Michael H. Seymour, Torbjörn Sjöstrand, Peter Skands, and Bryan Webber. General-purpose event generators for lhc physics. *Physics Reports*, 504(5):145 – 233, 2011.

[81] T. Gleisberg et al. Event generation with SHERPA 1.1. *JHEP*, 02:007, 2009.

[82] Simone Alioli, Paolo Nason, Carlo Oleari, and Emanuele Re. A general framework for implementing NLO calculations in shower Monte Carlo programs: the POWHEG BOX. *JHEP*, 06:043, 2010.

[83] Paolo Nason. A New method for combining NLO QCD with shower Monte Carlo algorithms. *JHEP*, 11:040, 2004.

[84] Stefano Frixione, Paolo Nason, and Carlo Oleari. Matching NLO QCD computations with Parton Shower simulations: the POWHEG method. *JHEP*, 11:070, 2007.

[85] Stefano Catani, Leandro Cieri, Giancarlo Ferrera, Daniel de Florian, and Massimiliano Grazzini. Vector boson production at hadron colliders: a fully exclusive QCD calculation at NNLO. *Phys. Rev. Lett.*, 103:082001, 2009.

[86] Hung-Liang Lai et al. New parton distributions for collider physics. *Phys. Rev.*, D 82:074024, 2010.

[87] Torbjorn Sjöstrand, Stephen Mrenna, and Peter Z. Skands. PYTHIA 6.4 Physics and Manual. *JHEP*, 0605:026, 2006.

[88] Michal Czakon, Paul Fiedler, and Alexander Mitov. Total Top-Quark Pair-Production Cross Section at Hadron Colliders Through $O(\alpha_S^4)$. *Phys. Rev. Lett.*, 110:252004, 2013.

[89] Michal Czakon and Alexander Mitov. NNLO corrections to top pair production at hadron colliders: the quark-gluon reaction. *JHEP*, 1301:080, 2013.

[90] Michal Czakon and Alexander Mitov. NNLO corrections to top-pair production at hadron colliders: the all-fermionic scattering channels. *JHEP*, 1212:054, 2012.

[91] Peter Bärnreuther, Michal Czakon, and Alexander Mitov. Percent Level Precision Physics at the Tevatron: First Genuine NNLO QCD Corrections to $q\bar{q} \to t\bar{t} + X$. *Phys. Rev. Lett.*, 109:132001, 2012.

[92] Matteo Cacciari, Michal Czakon, Michelangelo Mangano, Alexander Mitov, and Paolo Nason. Top-pair production at hadron colliders with next-to-next-to-leading logarithmic soft-gluon resummation. *Phys. Lett. B*, 710:612–622, 2012.

[93] Michal Czakon and Alexander Mitov. Top++: A Program for the Calculation of the Top-Pair Cross-Section at Hadron Colliders. *Comput.Phys.Commun.*, 185:2930, 2014.

[94] Peter Zeiler Skands. Tuning Monte Carlo Generators: The Perugia Tunes. *Phys.Rev.*, D82:074018, 2010.

[95] Nikolaos Kidonakis. Two-loop soft anomalous dimensions for single top quark associated production with a W- or H-. *Phys.Rev.*, D 82:054018, 2010.

[96] G. Corcella et al. HERWIG 6: An Event generator for hadron emission reactions with interfering gluons (including supersymmetric processes). *JHEP*, 01:010, 2001.

[97] LHC Higgs Cross Section Working Group. Handbook of LHC Higgs Cross Sections: 2. Differential Distributions. *CERN-2012-002*, CERN, Geneva, 2012.

[98] ATLAS Collaboration. The simulation principle and performance of the ATLAS fast calorimeter simulation FastCaloSim. 2010.

[99] Georges Aad et al. Muon reconstruction performance of the ATLAS detector in proton proton collision data at $\sqrt{s}$ =13 TeV. *Eur. Phys. J.*, C76(5):292, 2016.

[100] Electron efficiency measurements with the ATLAS detector using the 2015 LHC proton-proton collision data. Technical Report ATLAS-CONF-2016-024, CERN, Geneva, Jun 2016.

[101] Matteo Cacciari, Gavin P. Salam, and Gregory Soyez. The anti- k t jet clustering algorithm. *Journal of High Energy Physics*, 2008(04):063, 2008.

[102] Zachary Marshall. Simulation of Pile-up in the ATLAS Experiment. *J. Phys. Conf. Ser.*, 513:022024, 2014.

[103] Tagging and suppression of pileup jets with the ATLAS detector. Technical Report ATLAS-CONF-2014-018, CERN, Geneva, May 2014.

[104] Georges Aad et al. Jet energy measurement and its systematic uncertainty in proton-proton collisions at $\sqrt{s} = 7$ TeV with the ATLAS detector. *Eur. Phys. J.*, C75:17, 2015.

[105] Jet Calibration and Systematic Uncertainties for Jets Reconstructed in the ATLAS Detector at $\sqrt{s} = 13$ TeV. Technical Report ATL-PHYS-PUB-2015-015, CERN, Geneva, Jul 2015.

[106] Optimisation of the ATLAS b-tagging performance for the 2016 LHC Run. Technical Report ATL-PHYS-PUB-2016-012, CERN, Geneva, Jun 2016.

[107] Expected performance of missing transverse momentum reconstruction for the ATLAS detector at $\sqrt{s} = 13$ TeV. Technical Report ATL-PHYS-PUB-2015-023, CERN, Geneva, Jul 2015.

[108] C. G. Lester and D. J. Summers. Measuring masses of semiinvisibly decaying particles pair produced at hadron colliders. *Phys. Lett.*, B463:99–103, 1999.

[109] Alan Barr, Christopher Lester, and P. Stephens. m(T2): The Truth behind the glamour. *J. Phys.*, G29:2343–2363, 2003.

[110] Georges Aad et al. Measurement of the top quark-pair production cross section with ATLAS in pp collisions at $\sqrt{s} = 7$ TeV. *Eur. Phys. J.*, C71:1577, 2011.

[111] Georges Aad et al. Measurement of the top quark pair production cross section in pp collisions at $\sqrt{s} = 7$ TeV in dilepton final states with ATLAS. *Phys. Lett.*, B707:459–477, 2012.

[112] A L Read. Presentation of search results: the cl s technique. *Journal of Physics G: Nuclear and Particle Physics*, 28(10):2693, 2002.

[113] M. Baak, G. J. Besjes, D. Cote, A. Koutsman, J. Lorenz, and D. Short. HistFitter software framework for statistical data analysis. *Eur. Phys. J.*, C75:153, 2015.

[114] Simulation of top quark production for the ATLAS experiment at sqrt(s) = 13 TeV. Technical Report ATL-PHYS-PUB-2016-004, CERN, Geneva, Jan 2016.

[115] Martin Bauer, Ulrich Haisch, and Felix Kahlhoefer. Simplified dark matter models with two Higgs doublets: I. Pseudoscalar mediators. 2017.

[116] Morad Aaboud et al. Search for dark matter produced in association with bottom or top quarks in $\sqrt{s} = 13$ TeV pp collisions with the ATLAS detector. *Eur. Phys. J.*, C78(1):18, 2018.

[117] Morad Aaboud et al. Search for top squarks in final states with one isolated lepton, jets, and missing transverse momentum in $\sqrt{s} = 13$ TeV *pp* collisions with the ATLAS detector. *Phys. Rev.*, D94(5):052009, 2016.

[118] T. Zhao, Y. Chen, S. Han, and J. Hersch. A study of electron drift velocity in arco2 and arco2cf4 gas mixtures. *Nuclear Instruments and Methods in Physics Research Section A: Accelerators, Spectrometers, Detectors and Associated Equipment*, 340(3):485 – 490, 1994.

[119] Patrik Thuiner, Leszek Ropelewski, and Christina Streli. Ion space-charge effects in multi-GEM detectors: challenges and possible solutions for future applications, Nov 2016.

[120] John Sir Townsend. *The theory of ionization of gases by collision.* London Constable,.

[121] V Peskov and P Fonte. Research on discharges in micropattern and small gap gaseous detectors. Technical Report arXiv:0911.0463, Nov 2009.

[122] C. Adloff et al. Construction and test of a 1x1m^2 Micromegas chamber for sampling hadron calorimetry at future lepton colliders. *Nucl. Instrum. Meth.*, A729:90–101, 2013.

[123] F Thibaud et al. Performance of large pixelised micromegas detectors in the compass environment. *Journal of Instrumentation*, 9(02):C02005, 2014.

Acknowledgements

I am now arrived at the closing credits of my PhD. And it is time to thank all those without whom this experience would have never be possible.

First of all, for the third time, my deepest gratitude goes to Prof. Adele Rimoldi. Thanks for having supported me in every step of my carrier so far. We went quiet far since the first time we met.

More than a simple acknowledgement goes to the CERN Doctoral programme and to my CERN group;
I have grown up here, both as a person and as a researcher, and I will always be grateful.

Thanks to Christoph, for always supporting our activities and for your daily optimism and motivation. This has been really important for me.

Thanks to Paolo, I have always seen in you a friend, a mentor to learn from.

Thanks to Rania, because for more than 4 years we have been working together side to side, R&D first, PCB QAQC later.

Thanks to Andrea, for our conversations about physics and future.

Thanks to Jona, Joerg, Luigi, Givi, Dario, Stelian, Federico, Valentina, Roberto, Barbara and all the others having shared good and less good moments in these years in the lab. It has been a pleasure to work with you all.

A special thank goes to Giacomo, without whom half of this thesis would not be here. I will be always grateful.

To the ATLAS Pavia group, Gabriella, Andrea, and all the others for the support and the faith placed in me.

Thanks to Federico, Priscilla, Giulia, Francesca, Yoav and all the friends and colleagues I have worked with in our search for Dark Matter.

Thanks to Giada, Luca, Valerio because you have the passion that makes this job special.

Finally a big thank to my family, to Donatella and Pierluigi. In everything I do, there is always your imprint.

and to Sofia, because the end of the PhD is nothing but the beginning of a new, exciting, adventure together.